



UNIVERSITE D'AIX-MARSEILLE

THE UNIVERSITY OF THE ACADEMY OF SCIENCES OF MOLDOVA

ECOLE DOCTORALE DES SCIENCES CHIMIQUES

INSTITUT DES SCIENCES MOLECULAIRES DE MARSEILLE/ UMR 7313
THE INSTITUTE OF CHEMISTRY OF THE ACADEMY OF SCIENCES OF MOLDOVA

Thèse présentée pour obtenir le grade universitaire de Docteur

Discipline : Chimie

Spécialité : Chimie Bioinorganique

Olesea CUZAN

SYNTHESIS AND CHARACTERIZATION OF NEW TRANSITION METAL COMPLEXES FOR CATALYTIC OXIDATION AND ELECTROLYTIC PROTON REDUCTION

Soutenue le 25/11/2016 devant le jury :

Dr. Athanassios G. COUTSOLELOS

Dr. Silvia MELNIC

Dr. Marius REGLIER

Dr. Maylis ORIO

Dr. Dumitru SIRBU

Dr. Michel MAFFEI

Dr. Vasile LOZAN

Rapporteur

Rapporteur

Examineur

Examineur

Examineur

Directeur de thèse

Co-directeur de thèse

ACKNOWLEDGEMENTS

This thesis was initiated under a joint international supervision (cotutelle) between Aix-Marseille University and University of the Academy of Sciences of Moldova and it was realized in both BiosCiencs research team of the Institute of Molecular Sciences of Marseille (iSm2) and the Bioinorganic Chemistry laboratory of the Institute of Chemistry of the Academy of Sciences of Moldova (LCBA).

The undertaking and successful completion of this thesis has been a long journey and was possible due to the help, guidance and support of many great researchers and wonderful people. Each of them brought an important and appreciable contribution to the puzzle we were trying to solve during these years. I would like to thank every one of them.

First of all, I want to convey my gratitude towards my grandfather, who is no longer here with us, but whom we remember dearly. He is the one who taught me to understand and love chemistry.

I want to express my deepest appreciation to my advisor Professor Constantin TURTA for his mentoring, guidance, for introducing me to scientific research, for being a supportive mentor and always offering constructive advices. Thanks to him, I am able to call myself a scientist and I am honored to have been his PhD student. I would like to dedicate this thesis to his memory.

Special thanks are due to Dr. Marius REGLIER, for all his help, valuable input and for giving me the opportunity to do my PhD in Marseille. I will always keep in mind his kindness, dedication and eagerness to help.

I am very grateful to my supervisor, Professor Michel MAFFEI for his contribution to this research, and for introducing me to the field of phosphonates. His knowledge and support are very appreciated.

I would like to thank Dr. Silvia MELNIC (Institute of Chemistry, Moldova) and Dr. Athanasios COUTSOLELOS (University of Crete, Greece) for kindly accepting to be referees of my thesis. Also I would like to thank Dr. Dumitru SIRBU (Institute of Chemistry, Moldova) and Dr. Vasile LOZAN (Institute of Chemistry, Moldova) for kindly accepting to be members of the thesis jury.

This thesis would not have been possible to realize without the support that I received from Dr. Maylis ORIO who helped me with the DFT calculations, with good feedback and suggestions during the writing of this manuscript.

Also, I would like to thank Dr. Michel GIORGI and Dr. Sergiu SHOVA for their help with structure determination.

Next, I would like to acknowledge all members of BiosCiencs group and LCBA laboratory including Dr. Amelie KOCHER, Dr. Jalila SIMAAN, Dr. Bruno FAURE, Dr. Viviane ROBERT, Dr. Alda Lisa CONCIA for their support and contribution to the realization of this work, Dr. Tatiana STRAISTARI, Dr. Mihai IACOB, Viorina GORINCIOY, Irina VODA for their assistance and friendship during all these years. I would also like to mention Dr. Thierry TRON, Dr. Yasmina MEKMOUCHE, Dr. Olga IRANZO, Sandrine NICOLETTI, Dr. Renaud HARDRE, Dr. Mireille ATTOLINI, Yolande CHARMASSON, Dr. Marianthi KAFFENTZI, Camile MODOLO, Dr. Pierre ROUSSELOT-PAILLEY, Dr. Sybille TACHON, Dr. Emmanuelle OHEIX, Dr. Juan RICO-MOLINS, Eugenie FOURNIER, Alexandre HAUTTIER, Dr. Cristoph DECROS, Sidiky MENIL, Dr. Vadim DRUTA, Dr. Ana LAZARESCU and wish them the best in their future endeavors.

I greatly appreciate the support received through the collaborative work undertaken with the Molecular Photonics Laboratory of the Newcastle University, Professor Andrew C. BENNISTON and Dr. Elizabeth A. GIBSON.

The Doctoral Schools from Marseille and Chisinau, led by Pr. Thierry CONSTANTIEUX, Corinne ESQUIVA and Dr. Aculina ARICU are acknowledged for their support and assistance.

Campus France (EIFFEL-DOCTORAT 2015 / 840918H); the CNRS and the Academy of Sciences of Moldova (Bilateral agreement EDC25722 2013-2014/ 13.820.08.01/FrF) are acknowledged for financial support.

And finally, but most importantly, I am very grateful to my family for their unconditional love, encouragement and understanding. I have to say that working on this thesis has been a great experience and I am looking forward to everything the future brings!

Thank you! All of you!

DISSEMINATION AND PUBLICATION OF THE RESEARCH FINDINGS

The research results described in this thesis were presented in poster (four abstracts) and five oral sessions at national and international scientific conferences, symposia, summer schools: Symposium & Young-Researcher-Meeting: Current Challenges in Supramolecular Artificial Photosynthesis (09 – 13 March 2014, Jena, Germany); Summer School “Bioinspired Materials for Solar Energy Utilization” (07 – 18 July 2014, Heraklion, Greece); The International Conference of PhD students (10 March 2015, Chişinău, Moldova); XVIIIth International Conference "Physical Methods in Coordination and Supramolecular Chemistry", (07 – 09 October 2015, Chisinau, Moldova); Conference “Colloque Biomimétisme et chimie durable”, (10 November 2015, Paris, France); Conference „FrenchBic“, (06 – 09 March 2016, Murol, France); Conference „1ere journées AMU de l’Europe et de l’international“, (10 – 11 March 2016, Aix en Provence, France); Conference „6emes Rencontres Scientifiques des Doctorants en Chimie de Marseille“, (19 – 20 May, Marseille, France); The 8th International Conference “Materials Science and Condensed Matter Physics”, (12 – 16 September, Chisinau, Moldova).

Some aspects of the research process were disseminated at scientific TV show: “*Ştiinţă și inovare*”, TeleRadioMoldova, 28th December 2013 and 11th of January 2014.

This thesis is based on the following papers (one accepted article in journal with impact factor, one submitted article without co-authors in journal of B grade and one article in preparation):

1. Cuzan, O.; Kochem, A.; Simaan, J.A.; Bertaina, S.; Faure, B.; Robert, V.; Shova, S.; Giorgi, M.; Maffei, M.; Réglie, M.; Orio, M.; Oxidative DNA Cleavage Promoted by Phenoxy-Radical Copper(II) Complex. In: *Eur. J. Inorg. Chem.*, 2016. Accepted Manuscript, DOI:10.1002/ejic.201601001.
2. Cuzan, O.; Synthesis and Characterisation of a Novel Phosphonate Ligand and its Palladium(II) Coordination Compound. In: *Chemistry Journal of Moldova. General, Industrial and Ecological Chemistry*. Submitted Manuscript.
3. Cuzan, O.; Sirbu, D.; Kochem, A.; Orio, M.; Réglie, M.; Maffei, M.; Giorgi, M.; Shova, S.; Gibson, E.A.; Benniston, A.C.; Neutral Lipophilic Palladium(II) Complexes for Electrocatalytic Hydrogen Production. In: *Dalton Trans.* Manuscript in preparation.

TABLE OF CONTENTS

RESUME.....	8
SHORTCUTS.....	17
GENERAL INTRODUCTION	18
CHAPTER 1: Palladium complexes with benzotriazolyl phenolate ligands. ..	20
1.1. Introduction. Electrocatalytic hydrogen evolution.....	21
1.2. Ligands characterization.....	25
1.2.1. X-ray characterization.....	26
1.2.2. NMR characterisation.....	29
1.2.3. Cyclic voltammetry	31
1.2.4. UV-Visible absorption spectroscopy	32
1.3. Preparation of the Pd(II) coordination compounds.....	33
1.4. NMR characterisation	34
1.5. Structural characterization of the Pd(II) complexes	37
1.6. Cyclic voltammetry	42
1.7. UV-Visible absorption spectroscopy	44
1.8. Electrocatalysis	45
1.9. Calculation of number of electrons involved in the first reduction process	49
1.10. One-electron reduced species generation and characterization	50
1.11. Theoretical calculations	51
1.12. Gas analysis.....	53
1.13. Conclusions to Chapter 1	54
CHAPTER 2: Copper complexes with benzotriazolyl phenolate ligands.....	55
2.1. Introduction	56
2.2. Preparation of the Cu(II) coordination compounds	61

2.3. Structural characterisation of the Cu(II) complexes	62
2.4. IR study	69
2.5. UV-vis and EPR characterization of copper complexes.....	70
2.6. Electrochemical characterization	77
2.7. One-electron oxidized species generation and characterization	78
2.8. Veratryl alcohol oxidation	82
2.9. DNA cleavage	84
2.10. Conclusions to Chapter 2	90
CHAPTER 3: Palladium and copper phosphonates	91
3.1. Introduction	92
3.2. N-(methylene-2-pyridine)-N,N-bis(diethoxyphosphorylmethyl) amine (L ⁴).....	93
3.3. Palladium (II) complex	94
3.3.1. <i>Preparation of palladium(II) coordination compound</i>	94
3.3.2. <i>Structural characterization of palladium(II) coordination compound</i>	94
3.3.3. <i>NMR study of L⁴</i>	97
3.3.4. <i>UV-vis</i>	97
3.4. Copper (II) compound.....	98
3.4.1. <i>Preparation of copper(II) coordination compound</i>	98
3.4.2. <i>EPR characterization</i>	98
3.4.3. <i>Catalytic activity for the oxidation of p-nitrophenyl-β-D- glucopyranoside</i>	99
3.5. <i>N,N</i> bis(phosphonic acid methyl) 2-methylamino pyridine (L ⁶)	101
3.6. TiO ₂ nanoparticles and O ₂ consumption	102
3.7. Conclusions to Chapter 3	104
CHAPTER 4: EXPERIMENTAL SECTION	105
4.1. Physical methods of investigation	106
4.2. DFT calculations.....	107
4.3. Electrocatalysis cell and GC analysis.....	108

4.4. Oxydation experiments	108
4.5. DNA cleavage.....	109
4.6. Activity towards catalytic p-nitrophenyl- β -D-glucopyranoside oxidation	109
4.7. Synthetic procedures for compounds discussed in Chapters 1, 2 and 3.....	110
4.8. Conclusions to Chapter 4.....	123
GENERAL CONCLUSIONS	124
PERSPECTIVES.....	126
REFERENCES.....	127

RESUME

De nos jours, la capacité à synthétiser de nouveaux catalyseurs métalliques bioinspirés revêt une grande importance pour l'amélioration des conditions opératoires de nombreuses réactions chimiques et dans le but de développer une chimie respectueuse de notre environnement. En effet, on peut imaginer selon cette voie obtenir des catalyseurs susceptibles de réaliser des réactions classiques dans des conditions plus douces (donc plus économiques), mais aussi mettre en œuvre des réactions biomimétiques permettant d'accéder à de nouveaux procédés pour la production de sources d'énergie renouvelables, selon les principes de la chimie verte.

Les travaux présentés dans cette thèse se concentrent sur la conception de nouveaux complexes de métaux de transition (cuivre et palladium) basés sur deux classes différentes de ligands organiques: les benzotriazole-phénolates et les phosphonates. Les synthèses de ces composés ont été réalisées aussi bien par l'emploi de méthodes décrites dans la littérature que par la mise au point de protocoles originaux. La caractérisation des complexes obtenus ainsi que des ligands qui les constituent a été réalisée par différentes méthodes physico-chimiques (spectroscopie RMN, électrochimie, Résonance paramagnétique électronique (RPE), UV, Infra Rouge, cristallographie par diffraction des rayons X) et la chimie théorique.

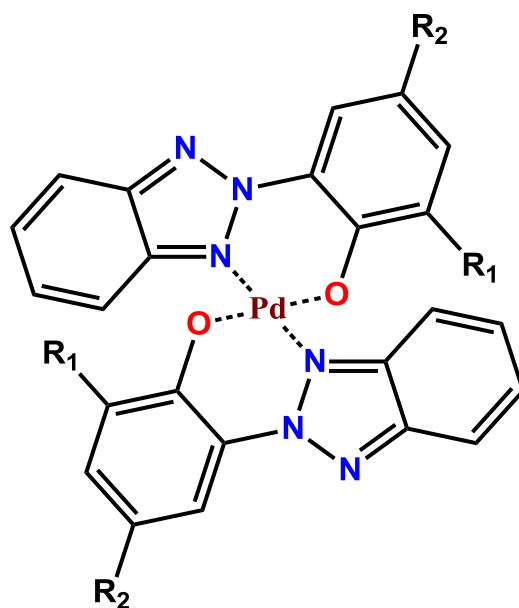
La génération et la caractérisation des différentes espèces réduites et oxydées nous ont aidés dans la détermination des mécanismes possible. Les composés obtenus ont été utilisés avec succès comme catalyseurs dans divers procédés tels que: la production d'hydrogène, l'oxydation d'alcool et le clivage d'ADN.

Ce thèse est constituée de quatre chapitres individuels au cours desquels les méthodes de synthèse et analyse des nouveaux composés de coordination avec des métaux de transition (palladium et cuivre) sont décrits.

Le premier chapitre présente la synthèse et la caractérisation de nouveaux complexes du palladium (II) en utilisant des ligands benzotriazole-phénolate. Les complexes de palladium figurent parmi les dérivés organométalliques les plus connus et les mieux décrits du fait de leur grande utilité dans les nombreuses réactions pallado-catalysées (couplages de Heck, Suzuki, Trost, réactions d'oxydation de Wacker, hydrogénation, électroréduction du CO₂).

En ce qui nous concerne, nous nous sommes tournés vers l'utilisation de ces nouveaux complexes en tant que catalyseurs pour la réduction électrocatalytique des protons, pour laquelle seulement quelques exemples ont été précédemment rapportés dans la littérature, et pour lesquels un seul décrit une expérience de détection d'hydrogène avec une valeur du turn over fréquence (TOF) de 2500 s⁻¹.

Nous avons réalisé la synthèse de composés de coordination originaux, dérivés du palladium (II) avec trois ligands différents, nommément le 2-(2H-benzotriazol-2-yl)-6-dodecyl-4-méthylphénol (**HL**¹), le 2-(2H-benzotriazol-2-yl)-4,6-di-tert-pentylphénol (**HL**²) et le 2-(2H-benzotriazol-2-yl)-4,6-bis(1-méthyl-1-phenylethyl)phénol (**HL**³).



$[\text{Pd}(\text{L}^1)_2]$: R_1 =dodecyl; R_2 =methyl

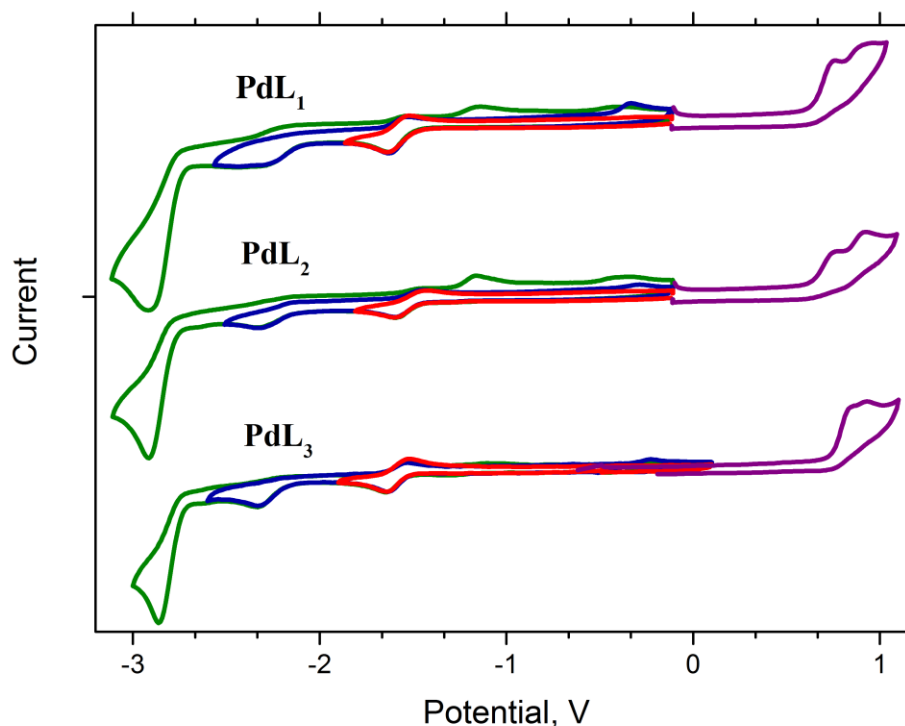
$[\text{Pd}(\text{L}^2)_2]$: $\text{R}_1=\text{R}_2$ =*tert*-pentyl

$[\text{Pd}(\text{L}^3)_2]$: $\text{R}_1=\text{R}_2$ =1-methyl-1-phenylethyl

$[\text{Pd}(\text{L}^2)_2]\text{H}_2\text{O}$: $\text{R}_1=\text{R}_2$ =*tert*-pentyl

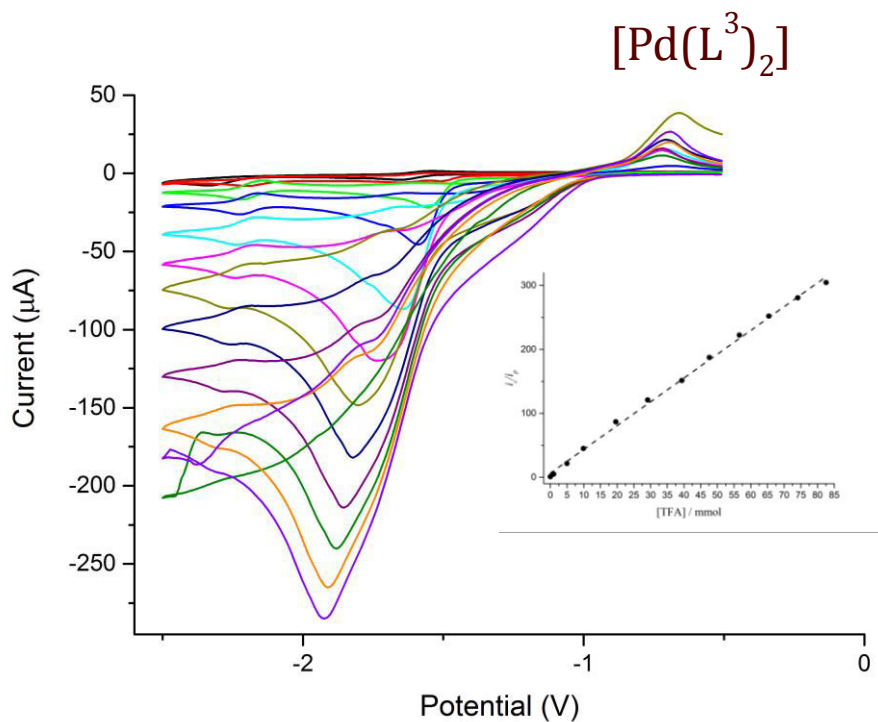
$[\text{Pd}(\text{L}^3)_2](\text{CH}_3)_2\text{CO}$: $\text{R}_1=\text{R}_2$ =1-methyl-1-phenylethyl

Ces complexes ont été isolés, purifiés et totalement caractérisés par différentes techniques (IR, analyse élémentaire, spectrométrie de masse, RMN, UV-vis et voltammétrie cyclique). Il apparaît ainsi que le palladium est lié à la fois aux deux atomes d'oxygène des fonctions phénol, et coordonné aux deux atomes d'azote des motifs triazole.



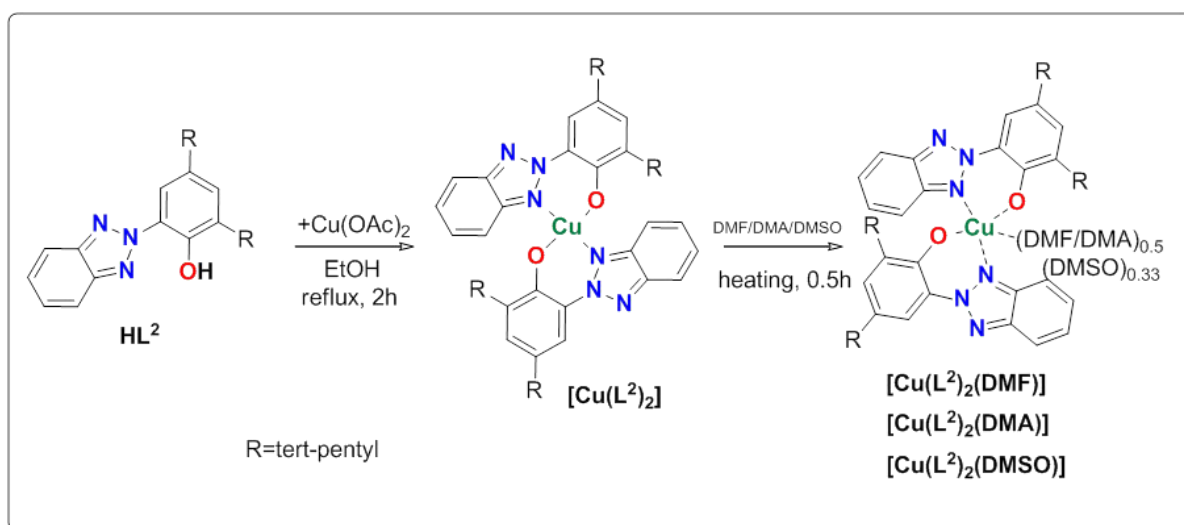
La caractérisation structurale par diffraction des rayons X a montré qu'ils cristallisent dans une structure monoclinique, les deux atomes d'oxygène étant en position *trans* par rapport au palladium (idem pour les atomes d'azote). La réduction électrocatalytique des protons a tout d'abord été observée au cours des expériences d'électrocatalyse en présence soit de l'acide trifluoroacétique (TFA) ou acétique, utilisés comme donneurs de protons sacrificiels, en solution dans le DMF avec le tétrabutyl hexafluorophosphate d'ammonium comme électrolyte.

Sur la base d'études électrocatalytiques, les valeurs des TOF ont été calculées pour les complexes de palladium (II) avec une valeur maximale de 18000 s^{-1} pour le complexe avec le troisième ligand.



La détection de l'hydrogène dégagé a été réalisée pour le complexe présentant la valeur TOF la plus haute, en utilisant l'analyse des gaz. La réaction est réalisée dans le DMF en présence de TFA à la concentration de 90 mM et par application d'un potentiel de -0,36 V vs. ENH ou -1.08 V vs. le couple redox Fc^+/Fc , l'électrode de travail étant constituée de diamant dopé au bore qui a conduit à la formation immédiate d'hydrogène moléculaire. Comme indiqué par l'analyse par chromatographie en phase gazeuse, la présence de catalyseur à hauteur de 1 mM a conduit à une augmentation du courant pour le même potentiel appliqué à une grandeur de trois ordres; avec une production immédiate et constante d'hydrogène. Près de sept turnovers ont été atteints au bout de cinq heures d'électrolyse et aucun signe de diminution de la production d'hydrogène n'a été observé à la fin de cette période. La surtension calculée pour le potentiel -1.08V a une valeur de 100 mV. Afin de faciliter la détermination du mécanisme, l'espèce monoréduite a été générée à la fois chimiquement et électrochimiquement, et caractérisée en utilisant des méthodes spectroscopiques UV-vis, EPR et les calculs théoriques. Sur la base de ces résultats, nous avons conclu que l'espèce responsable de la réduction électrocatalytique des protons est un intermédiaire monoréduit de palladium(I) et notre catalyseur peut donc être considéré comme le plus actif des complexes palladiés pour la production électrocatalytique de l'hydrogène.

La deuxième partie est consacrée aux complexes de cuivre (II) à base du ligand 2-(2H-benzotriazol-2-yl)-4,6-di-tert-pentylphenol (HL^2) et leur utilisation comme catalyseurs dans la réaction d'oxydation de l'alcool vératrylique et le clivage d'ADN. Ces travaux ont été inspirés par l'existence de nombreuses cupro-enzymes, employées par le monde vivant dans différents procédés catalytiques, et dont nous nous sommes inspirés pour imiter la nature. Ainsi, nous avons réalisé la synthèse de complexes du cuivre à partir des ligands benzotriazole employés à chapitre précédent, par réaction avec des sels de cuivre, soit au reflux du solvant (méthode 1), soit à température ambiante en présence de triéthylamine qui aide à la déprotonation du ligand.



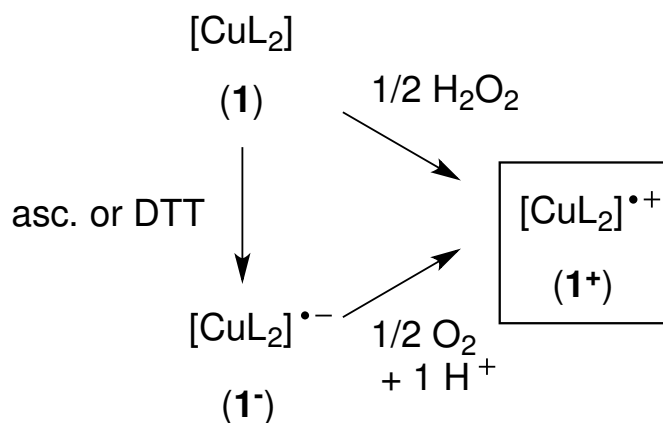
Les deux méthodes donnent des résultats comparables, et nous avons pu obtenir les complexes $[\text{Cu}(\text{L}^2)_2]$ avec de bons rendements. Selon le solvant utilisé, nous avons pu isoler les complexes $[\text{Cu}(\text{L}^2)_2(\text{DMF})]$, $[\text{Cu}(\text{L}^2)_2(\text{DMA})]$, ou encore $[\text{Cu}(\text{L}^2)_2(\text{DMSO})]$ pour lesquels une molécule de solvant est incluse dans la maille cristalline. La composition chimique a été confirmée par diffraction des rayons X, mis à part $[\text{Cu}(\text{L}^2)_2(\text{DMSO})]$ pour lequel la qualité des cristaux n'a pas permis une analyse satisfaisante. Les structures existent selon deux états de coordination différents : tétra-coordonné avec une coordination tétraédrique déformée, où le métal est coordonné à deux molécules de ligand aux atomes d'oxygène et d'azote, ou penta-coordonnée dans laquelle la position apicale est occupée par l'atome d'oxygène du solvant de coordination.

Afin d'avoir une idée précise des espèces oxydées mises en jeu dans les réactions d'oxydation catalysées par ces complexes, les intermédiaires monooxydés ont été générés par une réaction d'oxydation chimique avec 1 équivalent d'oxydant NOSbF_6 ; celui-ci a été isolé et complètement caractérisé par des méthodes spectroscopiques (EPR et UV-VIS) et des calculs

théoriques qui confirment la formation du complexe de cuivre (II) avec un ligand radical organique dans une configuration ferromagnétique.

L'activité catalytique de type galactose-oxydase de ces complexes a été évaluée par le biais de réactions d'oxydation de l'alcool veratrylique. L'aldéhyde vératrylique est produit en présence de peroxyde d'hydrogène avec une valeur TON de 5 moles de produit par mole de catalyseur calculé pour un temps de réaction de 30 minutes dans une solution de DMF à température ambiante. La quantité d'aldéhyde obtenu a été déterminée par spectrophotométrie à 310 nm en utilisant la technique de chromatographie liquide à haute performance.

Des complexes de cuivre (II) sont aussi connus pour provoquer la coupure de l'ADN de manière efficace, et ce dans des conditions classiques d'oxydation. Ceci nous a amenés à tester l'activité de nos complexes pour cette réaction. L'activité de nucléase du complexe de cuivre (II) a été étudiée sur l'ADN surenroulé pUC19 à une température de 37 ° C avec différents agents oxydant ou reducteur tels que le peroxyde d'hydrogène, l'ascorbate ou le dithiothréitol DTT (100 µM). Le complexe à base de cuivre présente une réactivité significative de clivage d'ADN dans la plage de concentration de 100 à 500 µM. La quantité d'ADN clivé (NC) augmente en fonction de la concentration du complexe, comme l'atteste la transformation progressive du plasmide superenroulé (SC) en la forme circulaire entaillé (NC), puis en la forme linéaire (L). Par incubation de l'ADN dans des conditions anaérobies avec le complexe de cuivre seul (500 µM), moins de 20% de la forme NC a été observée, tandis que dans des conditions oxydatives (H₂O₂ ou O₂ et ascorbate / DTT) avec la même concentration du complexe, une conversions totale (100%) en NC et formes L sont observées. Ces résultats confirment que le clivage de l'ADN se produit par un processus d'oxydation plutôt qu'un processus hydrolytique.

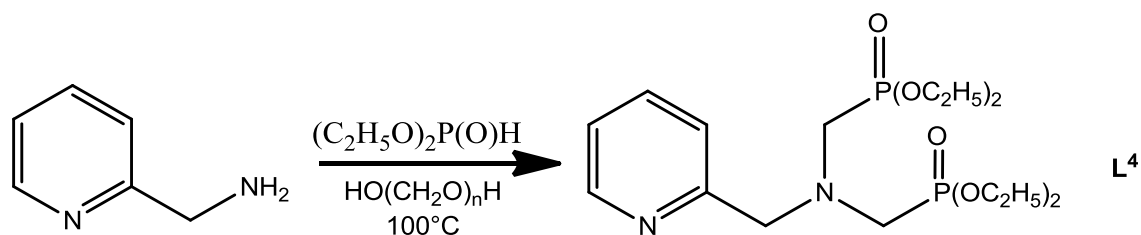


RESUME

Ces résultats très significatifs suggèrent que nos complexes sont capables de désorganiser l'ADN d'une cellule, et par conséquent, de provoquer sa destruction. Ce phénomène est à la base de l'activité de nombreux agents cytotoxiques, dont certains peuvent être utilisés comme agents anti-cancéreux.

Le troisième chapitre aborde la synthèse de nouveaux ligands organiques de type aminobisphosphonates contenant le motif pyridine. L'un des intérêts de ces composés est qu'ils présentent habituellement une solubilité importante dans l'eau, et l'on peut donc s'attendre à pouvoir solubiliser aisément les complexes correspondants dans les milieux aqueux, par opposition aux complexes étudiés dans les chapitres précédents. Ceci laisse donc présager l'utilisation de ces complexes métal bisphosphonates en tant que catalyseurs pour diverses réactions réalisées dans l'eau.

Un nouveau ligand bisphosphonate a été obtenu grâce à une double réaction de Kabachnik-Fields dans un très bon rendement.



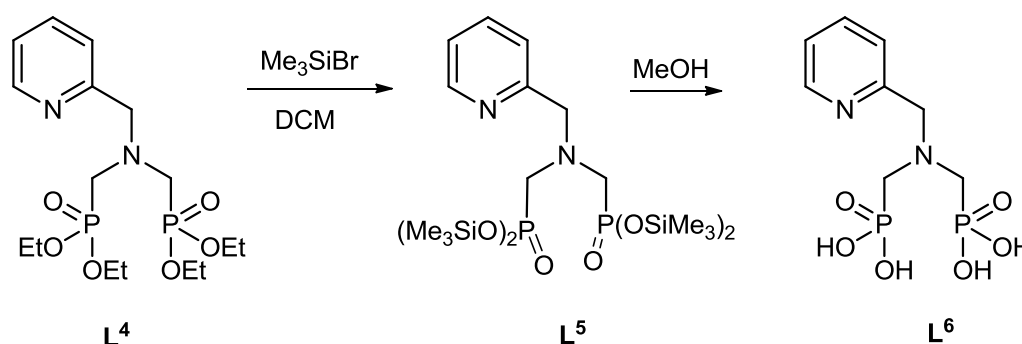
Il a ensuite conduit au complexe du palladium (II) correspondant selon un mode opératoire mis au point durant ce travail. La caractérisation de ce complexe a été effectuée selon les techniques spectroscopiques habituelles, qui mettent en évidence la stœchiométrie de deux molécules de ligand pour un atome de palladium. L'analyse par diffraction des rayons X montre que le palladium adopte une structure plan carrée, en étant coordonné uniquement aux atomes d'azote des deux cycles pyridine. Il n'y a aucune interaction entre le palladium et les groupements phosphonate.

En ce qui concerne le cuivre, un complexe Cu (II) dérivé de ce ligand a pu être isolé, mais n'a pas donné lieu à la formation de cristaux. Sa stœchiométrie entre le métal et le ligand est de 1 pour 1. Son analyse par RPE montre la coordination de l'atome de cuivre aux deux atomes de d'azote du motif aminopyridine.

Nous avons ensuite montré que ce complexe de cuivre est capable de catalyser la réaction d'oxydation du *p*-nitrophényl-β-D-glucopyranoside, utilisée comme réaction modèle. Ainsi,

en présence de peroxyde d'hydrogène, l'oxydation a rapidement lieu, la réaction étant suivie par la mesure spectrophotochimique de l'apparition du *p*-nitrophénol à 400 nm.

L'autre intérêt d'employer un ligand construit sur un motif phosphoré est de pouvoir préparer l'acide phosphonique correspondant susceptible d'être greffé sur un support métallique tel que l'oxyde de titane. Pour cela, l'acide amino bisphosphonique correspondant au ligand a été préparé selon un mode opératoire décrit dans la littérature. Toutefois, cette procédure, bien que simple dans sa réalisation, n'a pas donné les résultats indiqués. Afin de contourner cette difficulté, nous avons mis au point la synthèse de cet acide amino bisphosphonique par hydrolyse de l'acido bisphosphonate, selon une méthode décrite en employant le bromotriméthylsilane.



Dans ce cas, l'acide a été obtenu avec un bon rendement, et une pureté très satisfaisante.

Le greffage de cet acide sur de l'oxyde de titane a été réalisé, suivi de la complexation avec un sel de cuivre. L'analyse par RPE du composé résultant a montré que la coordination du métal sur le ligand greffé a lieu quasi instantanément.

Des expériences de production/consommation d'oxygène ont été réalisées en utilisant ce complexe en solution aqueuse, en présence persulfate de potassium et de ruthénium tris-bipyridine en tant que photosensibilisateur. Ces expériences préliminaires montrent que la consommation d'oxygène a lieu, mais il reste à déterminer le devenir de cet élément et quelle est la réaction mise en jeu.

Il résulte de ceci que l'utilité d'un tel catalyseur reste à évaluer sur plusieurs réactions modèles. Ce dernier chapitre constitue donc un préliminaire à une étude plus poussée, et a le mérite de montrer la faisabilité du concept envisagé initialement.

Enfin, le quatrième chapitre regroupe la partie expérimentale avec les protocoles expérimentaux employés pour les synthèses des nouveaux complexes ainsi que les résultats des analyses spectroscopiques concernant la caractérisation des composé obtenus.

SHORTCUTS

Cp – Cyclopentadienide rings	Fc – Ferrocene
CV – Cyclic Voltammetry	GC – Gas Chromatography
DCM – DiChloroMethane	HOMO – Highest Occupied Molecular Orbital
DFT – Density Functional Theory	i_c – current response of the catalytic wave
DMA – Dimethylacetamide	i_p – current response of the sample in the absence of acid
DMF – Dimethylformamide	IR – Infra Red
DMSO – Dimethyl Sulfoxide	LUMO – Lowest Unoccupied Molecular Orbital
DNA – DeoxyRibonucleic Acid	MeOH - Methanol
DSSC – Dye-Sensitized Solar Cell	MS – Mass Spectroscopy
EPR – Electron Paramagnetic Resonance	NHE – Normal Hydrogen Electrode
ESI – ElectroSpray Ionisation	NMR – Nuclear Magnetic Resonance
EtOH - Ethanol	RT – Room Temperature
	SCE – Saturated Calomel Electrode
	TBABF ₄ – Tetrabutylammonium Tetrafluoroborate
	TFA – Trifluoroacetic Acid
	THF – Tetrahydrofuran
	TOF – Turnover Frequency
	TON – Turn Over Number
	UV-Vis – Ultraviolet Visible
	η – Energy Conversion Efficiency

GENERAL INTRODUCTION

Green chemistry, or also called sustainable chemistry, represents a large area of chemistry which emerged from a variety of existing ideas about three decades ago. The main goal of green chemistry is the safe design of molecules, materials, products, and processes.

An important area of green chemistry is catalysis, since catalysts can help to develop new reactions, reduce the costs and significantly lower the amount of used chemicals.

In this context we decided to develop new transitional metal based catalysts and to use them in various clean chemical reactions such as electrocatalytic proton reduction, aerobic veratryl alcohol oxidation and DNA cleavage.

The objective of this thesis is the synthesis of new coordination compounds of palladium and copper with benzotriazolyl phenolate ligands as well as phosphonate ligands and their use as catalysts in different catalytic processes.

This thesis is comprised of four chapters and describes the synthesis and characterization of new coordination compounds as well as their use in various catalytic processes.

The first chapter is dedicated to the synthesis and characterization of new palladium based benzotriazolyl phenolates and their use as catalysts in hydrogen evolution processes. The electrochemical investigations proved the electrocatalytic generation of a gas, the nature of which was confirmed to be hydrogen by using the gas analysis.

The second chapter describes the synthesis and study of new copper benzotriazolyl phenolates as catalysts in veratryl alcohol oxidation reaction and biological active agents in DNA cleavage. The oxidation reaction as well as the DNA cleavage occurs through the formation of a one electron oxidized copper(II) active species with an organic ligand radical situated on the phenolic bond.

The third chapter comprises an ongoing investigation based on palladium and copper coordination compounds with phosphonate moieties based ligands. The phosphonate containing compounds have a good solubility in both organic and aqueous solutions which could escalate the catalytic behavior in different processes. The catalytic activity of a new copper(II) phosphonate complex was studied in the cleavage reaction of 4-Nitrophenyl β -D-glucopyranoside. In order to enhance the catalytic activity of phosphonate complexes they should be grafted of different surfaces like metal oxides or proteins.

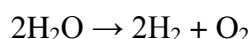
The fourth chapter describes the experimental methods used within this thesis and contains a table with structures of all fourteen new coordination compounds synthesized within this work.

CHAPTER 1

Palladium complexes with benzotriazolyl phenolate ligands.

1.1. Introduction. Electrocatalytic hydrogen evolution

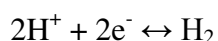
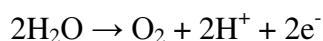
Nowadays, a special role in the use of renewable energy is assigned to the solar energy. After demonstrating the possibility of using solar energy to dissociate water molecules into hydrogen and oxygen,¹ chemists, together with researchers in physics, biology and engineering, have conducted multidisciplinary study to put into operation an effective technology for obtaining hydrogen - eco-friendly fuel with high specific energy capacity, produced through water splitting.²



Moreover, molecular catalysis of H₂ production from the electrochemical reduction of water (protons) by transition-metal complexes is one of the most convenient ways of a durable storage of renewably energies, provided that electrical energy is initially obtained from renewably resources.³

By having water as its combustion product, hydrogen is a perfect energy carrier. The development of an energy-efficient, cost-effective and ecologically-clean process for H₂ production is one of the greatest challenges to successfully shift from a fossil fuel-based economy to a hydrogen economy.

Till now have been investigated a large number of catalysts for small molecule activation in either homogeneous or heterogeneous phase. Most frequently, researchers focus their interest on individual catalysts for each of the two parallel half-reactions. As an example could serve the prototypical clean photochemical or electrochemical cell in which the water is split into molecular hydrogen and oxygen, one catalyst efficiently oxidizes water into molecular oxygen, protons and electrons, and another catalyst reduces the protons with the formation of molecular hydrogen.⁴



While electrocatalysis, is a mature and robust technology, the most promising devices, based on proton exchange membranes, rely on the use of platinum as an electrocatalyst to accelerate both hydrogen evolution and water oxidation reactions. Taking into consideration the fact that platinum is a rare, expensive metal and its resource is not itself renewable, the hydrogen

production process depends on the design of new efficient and robust electrocatalytic materials based on Earth-abundant elements.

By considering Nature's solutions to catalytic hydrogen production and oxidation, a good alternative to platinum for the oxidation of H_2 ,⁵ could be found in some living microorganisms which metabolize hydrogen using some enzymes called hydrogenases.^{6,7} These enzymes contain some metal-based centers constituted by iron and nickel atoms and in dependence of the nature of the active sites there are known three big classes of hydrogenases.

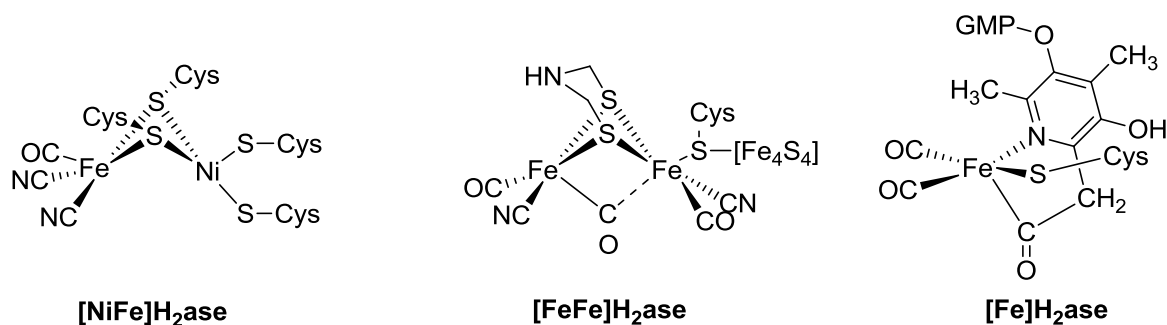


Figure 1. Structure of active sites of a) [Ni-Fe], b) [Fe-Fe], c) [Fe] – hydrogenase enzymes.

The electrocatalytic mechanism of hydrogen production catalyzed by enzymes has been extensively investigated⁸ and the structure of active sites of all three hydrogenases has been determined. (Figure 1) The active site of these enzymes has played the role of a blueprint for the development of series of new biomimetic⁹ and bioinspired¹⁰ molecular hydrogen evolving catalysts. The main approach of the researchers is not to directly incorporate hydrogenases into biotechnological devices but rather to use them as an inspiration for designing efficient noble metal-free inorganic complexes with catalytic activities for proton reduction and/or hydrogen activation.¹¹

It should be mentioned that bioinspired catalysts developed by D. L. DuBois show combined features of both [NiFe]- and [FeFe]-hydrogenases. By borrowing the Ni atom from [NiFe]-hydrogenases and the pendant proximal base and an amine group from [FeFe]-hydrogenases they elaborated a series of complexes with different external ligand substituents and confirmed that the presence of phosphonate moiety enhances the performance of the catalyst in aqueous mixtures by several times¹² up to a TOF of 1850 s^{-1} which is a good result. Also these catalysts are reported to be the only class of molecular catalysts able to electrocatalyze H_2 oxidation with very low overvoltages in the range of 0.1 – 0.2 V.^{13,14}

Nowadays are known a high number of bioinspired coordination compounds of various transitional metals which are successfully involved in the process of electrochemical proton reduction.

Due to their catalytic efficiency and rich redox chemistry in recent years, cobalt complexes were employed as catalysts for electro- and photochemical H₂ generation. Wang and collaborators¹⁵ classify cobalt H₂ evolving electrocatalysts in dependence of the nature of the ligand into eight classes: N₄-macrocyclic complexes,^{16,17} hexaamino complexes,¹⁸ porphyrin complexes,^{19,20} phthalocyanine complexes,²¹ cyclopentadienyl complexes,^{22,23} cobalt glyoxime complexes,^{24,25} polypyridine complexes²⁶ and cobalt complexes with one or two base-containing diphosphines.²⁷

Nevertheless in contrast to the multitude of systems under investigation, very little is known about the mechanisms of action of these catalysts at the molecular level. The design of molecular catalysts for hydrogen production by a heterolytic bond formation pathway and the understanding of the mechanism of action are crucial for future applications were these catalysts will be attached to an electrode. The heterolytic reaction ($H^+ + H^- \rightarrow H_2$) has obvious advantages over the homolytic reaction ($2H^\bullet \rightarrow H_2$) due to the fact that the latter pathway presumably requires two metal centers that will be difficult to bring together when immobilized on the electrode surface.⁴

At this point should be mentioned that a tool to enhance the activity of the catalyst is its deposition on monolayered carbon nanotubes which could be easily realized due to the $\pi - \pi$ stacking interactions.

Recently it was reported for the first time the use of a palladium complex as electrocatalyst in hydrogen evolution.²⁸ The dinuclear palladium(I)1,3-bis[(2-chloro)benzene]triazenide complex (Figure 2) has shown electrocatalytic properties for the production of hydrogen from acetic acid in DCM based on cyclic voltammetry experiment but no detection of the electrolysis products was performed.

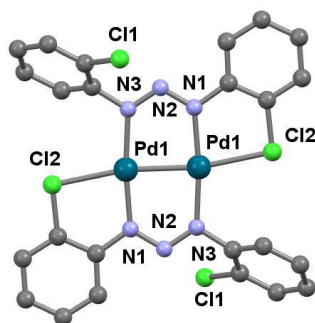


Figure 2. Molecular structure of palladium(I)1,3-bis[(2-chloro)benzene]triazenide complex.

The cyclic voltammogram was measured at a glassy carbon electrode in the presence of [*n*-Bu₄N][ClO₄] as supporting electrolyte. To determine possible electrocatalytic activity, cyclic voltammograms of the complex were recorded in the presence of acetic acid at different concentrations from 0.87 to 5.22 mM. The hydrogen evolution was observed near -0.95 V with catalytic onset shift to more positive potentials in the presence of increasing acid concentrations.

There are not many known Pd based catalysts for proton reduction, but a recently reported palladium(II) meso-tetraferrocenylporphyrine²⁹ (Figure 3) which shows some promising results for the development of new palladium containing molecular catalysts for H₂ production should be mentioned. This is the only reported detection of the electrolysis products performed in presence of a palladium(II) electrocatalyst. The reported Faradaic efficiency of 70% was obtained by the use of the Pd(II) catalyst during electrocatalytic proton reduction in DMF in the presence of TFA or TEAHCl at a glassy carbon working electrode by applying a potential of -1.5 V vs. saturated calomel electrode (SCE).

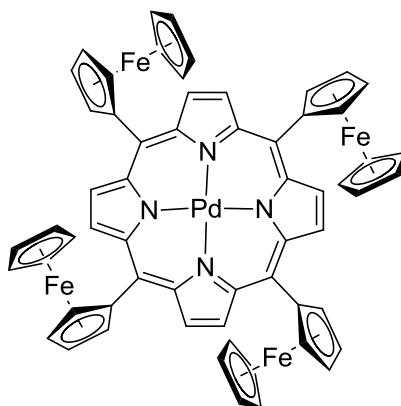


Figure 3. Illustration of the palladium(II) meso-tetraferrocenylporphyrine²⁹.

Development of molecular electrocatalysts for H₂ production is an interesting research field that has received considerable attention over the last few decades.³⁰ This work reflects the synthesis and crystal structure of three new Pd(II) complexes incorporating N,O-bidentate benzotriazol-phenolate ligands as potential catalysts for H₂ production with a TOF value of 2500 s⁻¹.

1.2. Ligands characterization

Benzotriazolyl phenols are widely known as a class of ultraviolet absorbers widely used in industry as protection of commercially important plastics and synthetic fibers against light.³¹

At the same time benzotriazole derivatives have an important role as precursors in the formation of heterocyclic ring systems³² and also present significant biological activity.³³

The synthesis of benzotriazolyl phenols (Figure 4) occurs usually in two steps: formation of *o*-nitrophenylazo compounds followed by their reductive cyclisation. The *o*-nitrophenylazo compounds are prepared via the coupling reaction between *o*-nitrobenzenediazonium chloride and the appropriated phenol derivative.³¹ The reduction of *o*-nitrophenylazo compounds was widely studied and several reducing agents such as thiourea dioxide³⁴, hydrobromic acid in acetic acid³¹, zinc/ethanolic sodium alkaly³¹, benzyl alcohol/basic conditions³⁵, samarium diiodide³⁶ were successfully employed.

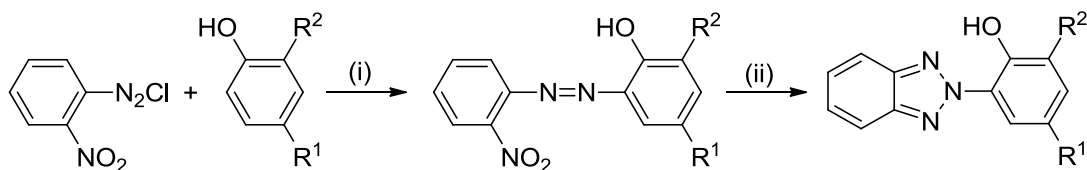


Figure 4. (i) Acidic or alkaline coupling; (ii) Zn/NaOH/EtOH.³¹

The benzotriazolyl phenols usually exist in two tautomeric forms (Figure 5).³⁷

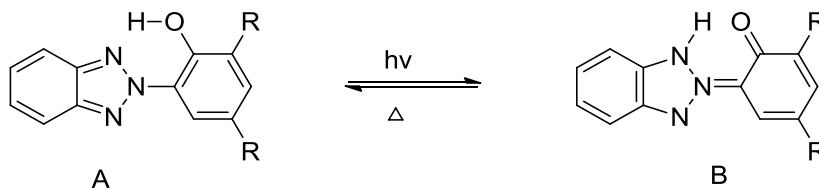
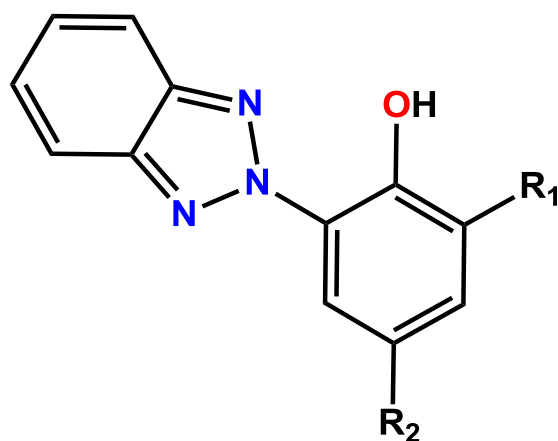


Figure 5. Enol-keto tautomeric forms of benzotriazolyl compounds A and B respectively.

In our work, we decided to use benzotriazolyl phenols as ligands (Figure 6) for copper and palladium coordination compounds.

The commercially available compounds 2-(2H-benzotriazol-2-yl)-4,6-di-*tert*-pentylphenol (**HL**²) and 2-(2H-benzotriazol-2-yl)-4,6-bis(1-methyl-1-phenylethyl)phenol (**HL**³) were used as received, while 2-(2H-benzotriazol-2-yl)-6-dodecyl-4-methylphenol (**HL**¹) was purified by column chromatography before use due to impure character of the ligand (for NMR characterization see subchapter 1.2.2).



HL¹: R₁=dodecyl; R₂=methyl

HL²: R₁=R₂=*tert*-pentyl

HL³: R₁=R₂=1-methyl-1-phenylethyl

Figure 6. Illustration of the ligands discussed in the text.

1.2.1. X-ray characterization

By using careful crystallization methods, the **HL**³ ligand was isolated as colorless needle like single crystals suitable for single crystal X-ray diffraction analysis. The collected relevant data for the ligand structure **HL**³ is presented in Table 1.

The ligand **HL**³ crystallized in the monoclinic centrosymmetric space group P2/c with two independent molecules in the asymmetric unit, one of them showing some disorder at one phenyl site (two positions). The molecular structure of one molecule of **HL**³ is shown in Figure 7. The hydroxyl group is intra-molecular hydrogen bonded to one of the nitrogen atoms within the triazole unit to generate a six membered ring. The phenyl groups are

positioned in an anti-arrangement with respect to each other, although this is undoubtedly not the lowest energy arrangement; a basic MM⁺ molecular mechanics calculation identified several conformations which were close in energy. The structure of **HL**³ also reveals the presence of inter-molecular interactions within the crystal as at least four relevant π -stacking and five CH/ π interactions can be reported (Table 2).

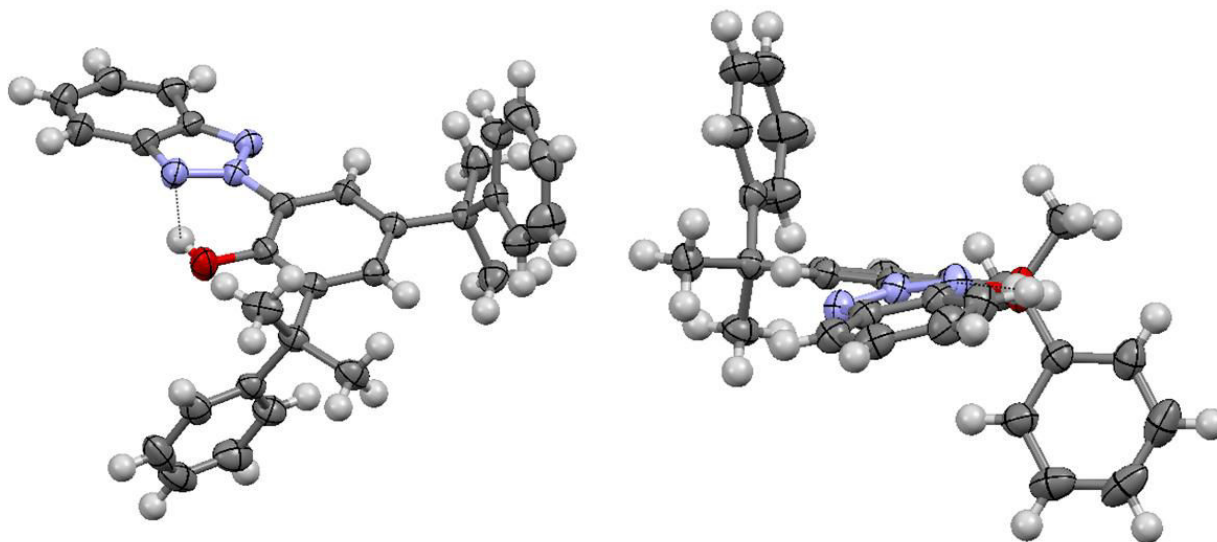


Figure 7. View of the molecular structure for **HL**³ showing the intramolecular hydrogen bond (left) and a side-on view showing the anti-arrangement of the phenyl groups ellipsoids (right).

The structural parameters of **HL**³ are in agreement with the bonding sequence shown for tautomer A in Figure 5.

Table 1. Crystallographic data, details of data collection and structure refinement parameters for **HL**³.

Compound	HL ³
Empirical formula	C ₆₀ H ₅₈ N ₆ O ₂
Formula weight (g/mol)	895.12
Crystal system	monoclinic
Space group	P2/c
<i>Unit cell dimensions</i>	
a (Å)	30.4748(5)
b (Å)	8.49767(11)
c (Å)	19.3531(3)
α (°)	90
β (°)	105.8243(16)
γ (°)	90
Volume (Å ³)	4821.82(13)

Z	4
λ (Å)	1.54184
$\rho_{\text{calc.}}$ (g/cm ³)	1.233
Crystal size (mm ³)	0.22 × 0.12 × 0.03
Temperature (K)	293
μ (mm ⁻¹)	0.587
Unique data, parameters, restraints	9221, 654, 12
R_1 ^(a)	0.0430
wR_2 ^(b)	0.1348
GOF ^(c)	1.132
Data collection method	SuperNova, Dual, Cu at zero, AtlasS2

^a $R_1 = \sum \|F_o\| - \|F_c\| / \sum \|F_o\|$;

^b $wR_2 = \{\sum [w(F_o^2 - F_c^2)^2] / \sum [w(F_o^2)^2]\}^{1/2}$;

^c GOF = $\{\sum [w(F_o^2 - F_c^2)^2] / (n - p)\}^{1/2}$, where n is the number of reflections and p the total number of parameters refined.

Table 2. Relevant short inter-molecular interactions for **HL**³.

<u>π-stacking</u>	<u>CH/π interactions</u>
Rings labels	Rings labels
Distance between rings centroids[Å] / dihedral angle between rings[°]	Ring label/H--ring distance[Å] /C-H--ring centroid angle[°]
R1 = N4/N3/N6/C31/C36	R5 = C14/C15/C16/C17/C18/C19
R2 = C31/C32/C33/C34/C35/C36	R6 = C7/C8/C9/C10/C11/C12
R3 = N1/N2/N3/C6/C1	R7 = C55/C56/C57/C58/C59/C60
R4 = C1/C2/C3/C4/C5/C6	R8 = C61/C62/C63/C64/C65/C66
	R9 = C37/C38/C39/C40/C41/C42
R1 – R1 _{<i>i</i>} : 4.5213(10) / 0.02(10)	R5 _{<i>iv</i>} /2.66/146.
R1 – R2 _{<i>ii</i>} : 4.1543(12) / 2.11(10)	R6 _{<i>v</i>} /2.97/139.
R2 – R2 _{<i>ii</i>} : 3.9803(13) / 0.02(11)	R7 _{<i>vi</i>} /2.76/154.
R3 – R4 _{<i>iii</i>} : 4.0695 (10) / 2.85(9)	R8 _{<i>vi</i>} /2.63/164.
	R9 _{<i>vii</i>} /2.99/143.
Symmetry codes: <i>i</i> = 1-x, 2-y, -z; <i>ii</i> = 1-x, 3-y, -z; <i>iii</i> = 2-x, -1-y, 1-z	Symmetry codes: <i>iv</i> = x, -y, 1/2+z; <i>v</i> = x, 1+y, z; <i>vi</i> = 1-x, 1+y, 1/2-z; <i>vii</i> = x, -1+y, z

1.2.2. NMR characterisation

The ^1H -NMR spectra of the free ligands are shown in Figures 8 – 10.

The initial spectrum of **HL**¹ shows the presence of six different signals in the region of spectrum 11.76 – 11.07 ppm with the relative areas (0.05, 0.45, 1.0, 0.49, 0.14, 0.08) attributed to the OH proton. This shows that the ligand contains impurities. The signal at 11.42 ppm has the biggest area, in proportion of 45 % (calc. from the ratio of OH signals). In the region 8.25 – 7.08 ppm can be seen signals attributed to aromatic protons with the relative area of 14.01. In the aliphatic region (<3.5 ppm) the total proton area is 75.88. This way from the spectrum we have the ratio of OH : AromaticH : AliphaticH of 1 : 6.3 : 34.3, while from the structure it is 1 : 6 : 28. Therefore, we detect the presence six OH containing compounds in the analyzed mixture and alkyls homologues and isomerism could be one explanation.

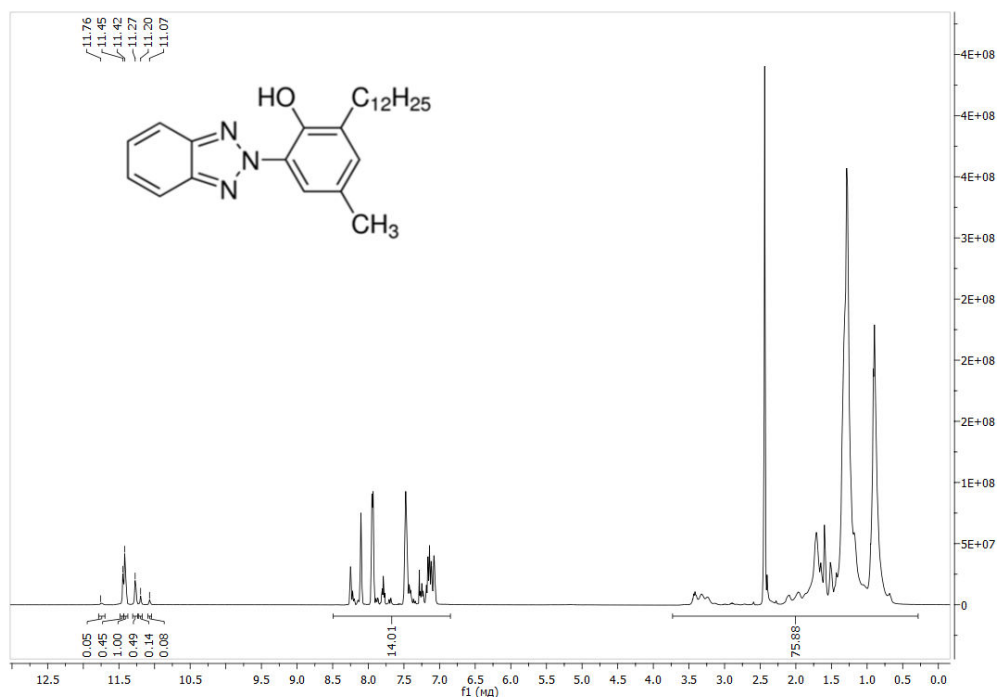


Figure 8. 400 MHz ^1H -NMR spectrum for initial **HL**¹.

The ^1H -NMR spectrum for **HL**² shows the presence of ten signals: one signal at 11.78 ppm attributed to one OH proton; four signals in the range 8.28 – 7.33 ppm attributed to six CH (aromatic) protons and five signals in the range 2.08 – 0.72 ppm attributed to twenty two aliphatic protons CH_2 (four) and CH_3 (eighteen).

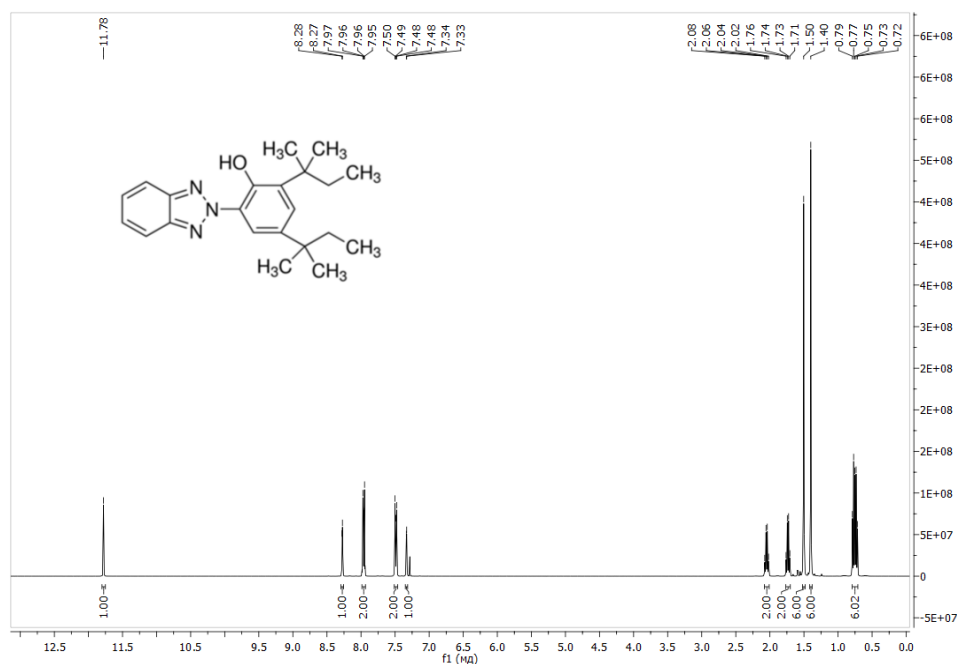


Figure 9. 400 MHz ¹H-NMR spectrum for **HL²**.

The ¹H-NMR spectrum for **HL³** shows the presence of six signals: one signal at 11.57 ppm attributed to one OH proton; three signals in the range 8.48 – 7.28 ppm attributed to sixteen CH (aromatic) protons and two singlets at 1.96 and 1.85 ppm attributed to twelve CH₃ (aliphatic) protons.

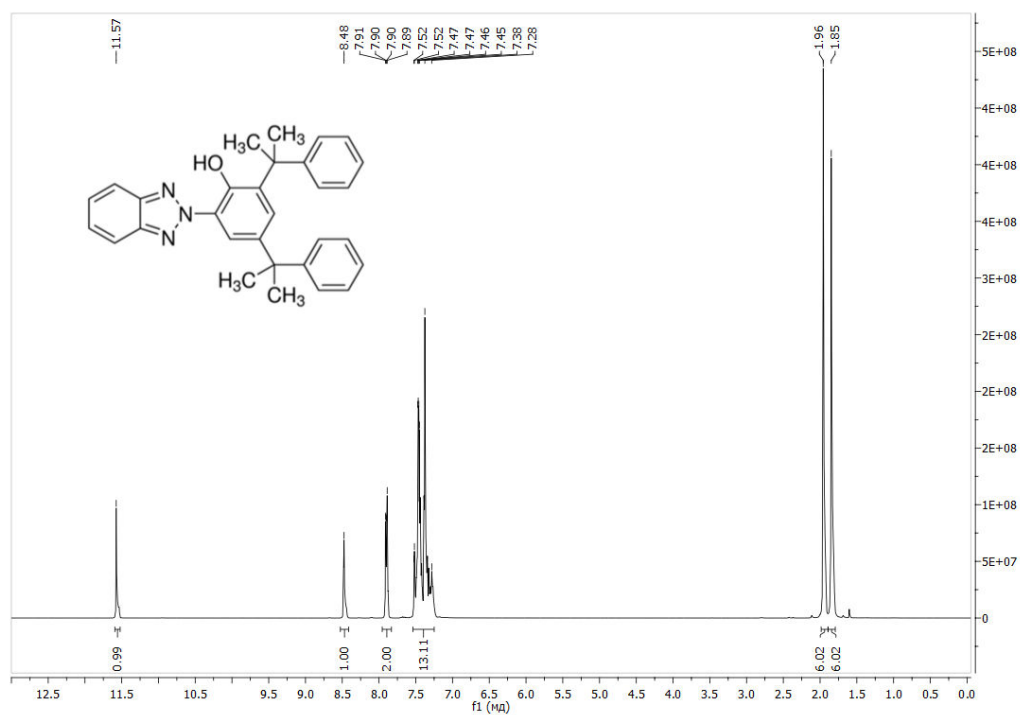


Figure 10. 400 MHz ¹H-NMR spectrum for **HL³**.

1.2.3. Cyclic voltammetry

The redox behavior of the ligands **HL**¹, **HL**² and **HL**³ (Figure 11, Table 3) were studied by cyclic voltammetry in dry DMF at a glassy-carbon electrode using 0.1 M tetrabutylammonium hexafluorophosphate (TBAPF₆, [Bu₄N][PF₆]) as the supporting electrolyte. All potentials are referred to Fe(Cp)₂⁺/Fc(Cp)₂ redox couple.

For all studied ligands (Figure 11) we can see a similar character: in the cathodic part of the spectrum can be observed a quasi-reversible redox signals with $E_{1/2}^0 = -2.20$ V, -2.22 V, -2.15 V for **HL**¹, **HL**² and **HL**³ respectively while in the anodic region appears an irreversible signal at $E_p^{a,1} = 0.80$ V, 0.90 V, 0.95 V for **HL**¹, **HL**² and **HL**³ respectively.

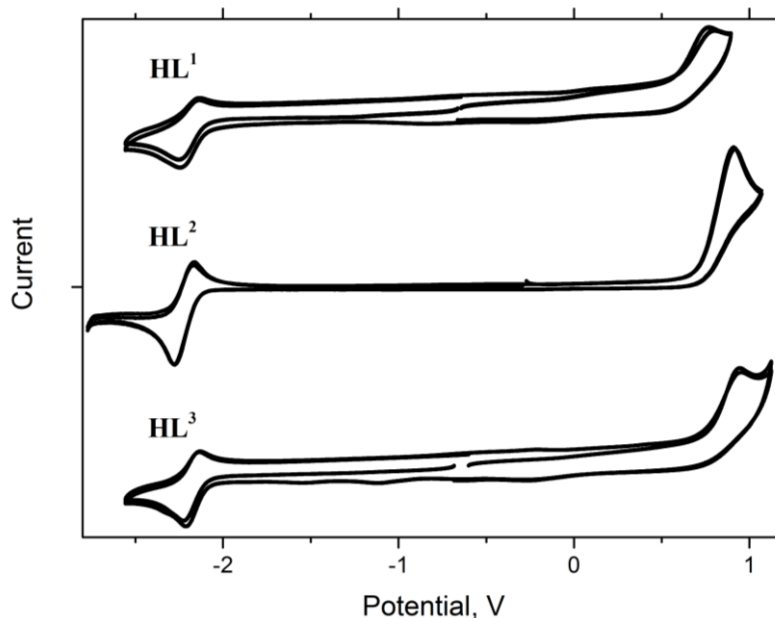


Figure 11. Cyclic voltammograms recorded for **HL**¹, **HL**² and **HL**³ in DMF containing 0.1M TBAPF₆ vs Fc⁺/Fc at a glassy carbon working electrode.

Table 3. Cyclic voltammograms data for **HL**¹, **HL**² and **HL**³ ligands.

Ligand	$E_p^{c,0}$	$E_p^{a,0}$	$E_{1/2}^0$	$E_p^{a,1}$
HL ¹	-2.25	-2.15	-2.20	0.80
HL ²	-2.27	-2.17	-2.22	0.90
HL ³	-2.20	-2.10	-2.15	0.95

1.2.4. UV-Visible absorption spectroscopy

The room temperature electronic absorption spectra recorded for **HL**¹, **HL**² and **HL**³ in DMF show two broad bands with absorption maxima λ_{\max} at 305 and 340 nm for **HL**¹ and **HL**² and with λ_{\max} at 305 and 345 nm for **HL**³ (Figure 12) and the relevant parameters are summarized in Table 4.

According to theoretical calculations this transition is characteristic to electronic charge transfer to the hydroxyl group (1st peak) and from the hydroxyl group (2nd peak).

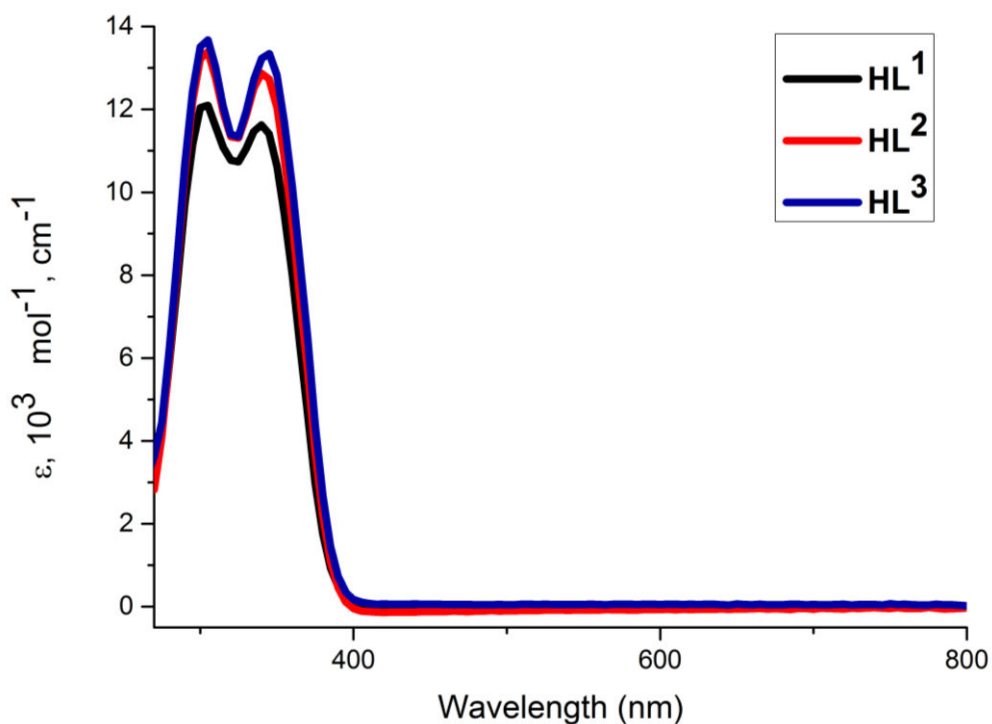


Figure 12. Electronic absorption spectra recorded in DMF for **HL**¹, **HL**² and **HL**³ ligands.

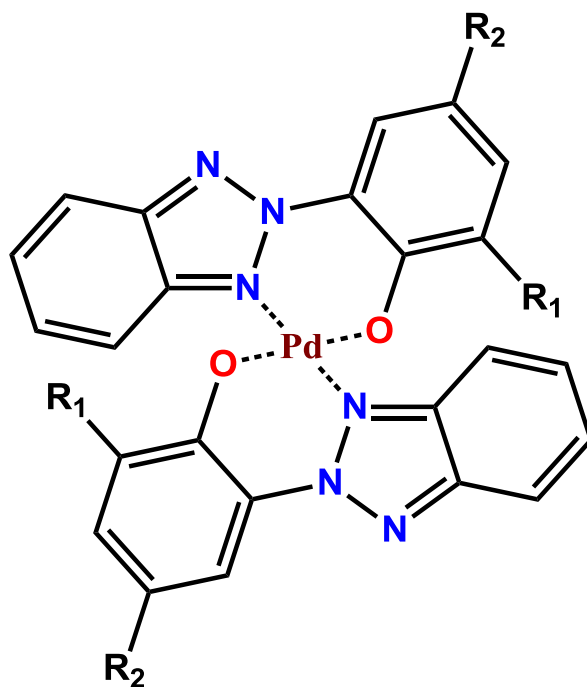
Table 4. Absorption maxima λ_{\max} and molar extinction coefficients ϵ of the UV-visible absorption of **HL**¹, **HL**² and **HL**³ in DMF.

Ligand	λ , nm (ϵ , $10^3 \text{ L mol}^{-1} \text{ cm}^{-1}$)	λ , nm (ϵ , $10^3 \text{ L mol}^{-1} \text{ cm}^{-1}$)
HL ¹	305 (11.4)	340 (11.0)
HL ²	305 (13.2)	340 (12.8)
HL ³	305 (13.7)	345 (13.4)

1.3. Preparation of the Pd(II) coordination compounds

The synthesis of palladium(II) coordination complexes with benzotriazolyl phenol ligands is a field under investigation. Nowadays there are known only a few palladium incorporated coordination compounds with benzotriazolyl phenol moiety containing ligands where the ligand coordinates to the ligand through $\widehat{\text{N}}\widehat{\text{O}}$ sites. The first time a palladium(II) benzotriazolyl phenol complex was reported several years ago.³⁸

The palladium(II) complexes $[\text{Pd}(\text{L}^1)_2]$, $[\text{Pd}(\text{L}^2)_2]$ and $[\text{Pd}(\text{L}^3)_2]$ were obtained by mixing 2 equivalents of appropriate **HL** ligand with 1 equivalent of palladium (II) acetate in THF under ambient conditions in very good yields (>80%). The requirement of chromatographic purification of the complexes involves non-quantitative yields. Complex $[\text{Pd}(\text{L}^3)_2](\text{CH}_3)_2\text{CO}$ was obtained upon recrystallization from acetone solution while complex $[\text{Pd}(\text{L}^2)_2]\text{H}_2\text{O}$ from chloroform solution. The chemical composition of the complexes $[\text{Pd}(\text{L}^1)_2]$, $[\text{Pd}(\text{L}^2)_2]$ and $[\text{Pd}(\text{L}^3)_2]$ was confirmed by $^1\text{H-NMR}$, ESI-MS and elemental analysis. By using careful crystallization techniques was possible to collect crystals suitable for single crystal X-ray diffraction analysis for complexes $[\text{Pd}(\text{L}^2)_2]\text{H}_2\text{O}$, $[\text{Pd}(\text{L}^3)_2]$ and $[\text{Pd}(\text{L}^3)_2](\text{CH}_3)_2\text{CO}$.



- $[\text{Pd}(\text{L}^1)_2]$: R_1 =dodecyl; R_2 =methyl
 $[\text{Pd}(\text{L}^2)_2]$: $\text{R}_1=\text{R}_2$ =*tert*-pentyl
 $[\text{Pd}(\text{L}^3)_2]$: $\text{R}_1=\text{R}_2$ =1-methyl-1-phenylethyl
 $[\text{Pd}(\text{L}^2)_2]\text{H}_2\text{O}$: $\text{R}_1=\text{R}_2$ =*tert*-pentyl
 $[\text{Pd}(\text{L}^3)_2](\text{CH}_3)_2\text{CO}$: $\text{R}_1=\text{R}_2$ =1-methyl-1-phenylethyl

Figure 13. Illustration of the palladium(II) complexes discussed in the text.

1.4. NMR characterisation

All the complexes are diamagnetic as shown by NMR studies. A representative ^1H NMR spectrum for $[\text{Pd}(\text{L}^3)_2]$ is shown in Figure 16, highlighting the four signals for the nonequivalent methyl groups.

It is interesting to note that the ^1H NMR spectrum for HL_3 displays a doubled signal for the methyl groups. In the aromatic region between 6 and 8 ppm there are present eleven signals attributed to sixteen protons while in the aliphatic region 1 – 3 ppm could be observed five signals: four signals attributed to twelve proton from methyl groups and one signal for the protons from the solvent.

The ^1H -NMR spectra of the palladium(II) coordination compounds $[\text{Pd}(\text{L}^1)_2]$, $[\text{Pd}(\text{L}^2)_2]$ and $[\text{Pd}(\text{L}^3)_2]$ are shown in Figures 14 – 16.

It should be mentioned here that the signals at 11.5 – 11.8 ppm characteristic for the hydrogen from OH group present in all three ligands are not present in the spectra for the complexes, which is due to deprotonation upon the formation of Pd–O bond.

The $^1\text{H-NMR}$ spectrum for $[\text{Pd}(\text{L}^1)_2]$ shows the presence of eight signals: four signals in the range 8.00 – 6.81 ppm attributed to six CH (aromatic) protons and four signals in the range 3.50 – 0.60 ppm attributed to twenty eight: CH_2 -22 and CH_3 -6 (aliphatic) protons.

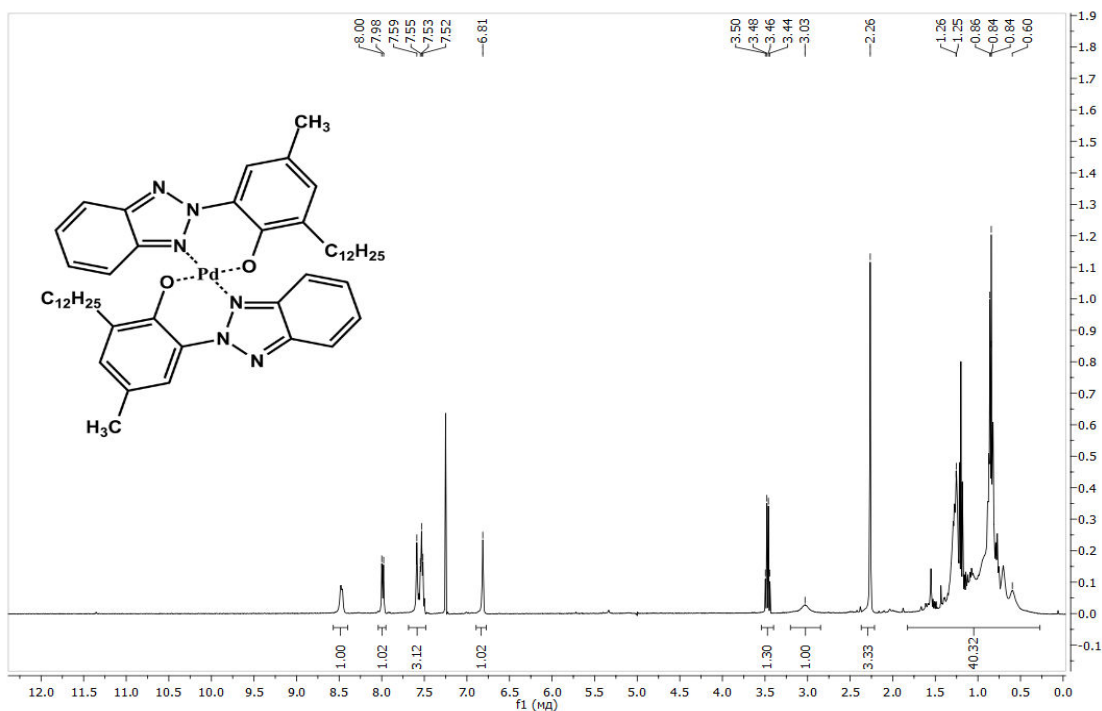


Figure 14. 400 MHz $^1\text{H-NMR}$ spectrum for $[\text{Pd}(\text{L}^1)_2]$.

The $^1\text{H-NMR}$ spectrum for $[\text{Pd}(\text{L}^2)_2]$ shows the presence of eleven signals: five signals in the range 8.34 – 7.19 ppm attributed to six CH (aromatic) protons and six signals in the range 1.75 – 0.45 ppm attributed to twenty two CH_2 -4 and CH_3 -18 (aliphatic) protons.

1.5. Structural characterization of the Pd(II) complexes

By using careful crystallization methods a number of products afforded single crystals suitable for X-ray diffraction analysis (SCXDR). Collected in Table 5 are the relevant data for the structures $[\text{Pd}(\text{L}^2)_2]\text{H}_2\text{O}$, $[\text{Pd}(\text{L}^3)_2]$ and $[\text{Pd}(\text{L}^3)_2](\text{CH}_3)_2\text{CO}$.

Table 5. Crystallographic data, details of data collection and structure refinement parameters for $[\text{Pd}(\text{L}^2)_2]\text{H}_2\text{O}$, $[\text{Pd}(\text{L}^3)_2]$ and $[\text{Pd}(\text{L}^3)_2](\text{CH}_3)_2\text{CO}$.

Compound	$[\text{Pd}(\text{L}^2)_2]\text{H}_2\text{O}$	$[\text{Pd}(\text{L}^3)_2]$	$[\text{Pd}(\text{L}^3)_2](\text{CH}_3)_2\text{CO}$
Empirical formula	$\text{C}_{88}\text{H}_{115.5}\text{N}_{12}\text{O}_{5.75}\text{Pd}_2$	$\text{C}_{60}\text{H}_{56}\text{N}_6\text{O}_2\text{Pd}$	$\text{C}_{61.5}\text{H}_{56}\text{N}_6\text{O}_{2.5}\text{Pd}$
Formula weight (g/mol)	1646.22	999.50	1025.52
Crystal system	monoclinic	monoclinic	monoclinic
Space group	$\text{P}2_1/\text{n}$	$\text{P}2_1/\text{c}$	$\text{C}2/\text{c}$
<i>Unit cell dimensions</i>			
a (Å)	15.7047(8)	12.9408(5)	30.8711(11)
b (Å)	29.5155(19)	31.9535(13)	14.0518(4)
c (Å)	20.0274(11)	12.7254(6)	26.4580(9)
α (°)	90	90	90.0
β (°)	102.241(6)	106.426(5)	114.879(4)
γ (°)	90	90	90.0
Volume (Å ³)	9072.3(9)	5047.2(4)	10412.2(6)
Z	4	4	8
λ (Å)	0.71073	0.71073	0.71073
$\rho_{\text{calc.}}$ (g/cm ³)	1.205	1.315	1.308
Crystal size (mm ³)	$0.2 \times 0.15 \times 0.15$	$0.24 \times 0.16 \times 0.03$	$0.28 \times 0.18 \times 0.14$
Temperature (K)	297.3(3)	293	293(2)
μ (mm ⁻¹)	0.451	0.417	0.407
Unique data, parameters, restraints	12936, 959, 101	11915, 630, 0	13190, 658, 39
R_1 ^(a)	0.0709	0.0510	0.0509
wR_2 ^(b)	0.1914	0.0987	0.1192
GOF ^(c)	1.032	1.080	1.047
Data collection method	Xcalibur, Eos	SuperNova, Dual, Cu at zero, AtlasS2	SuperNova, Dual, Cu at zero, AtlasS2

^a $R_1 = \Sigma||F_o| - |F_c||/\Sigma|F_o|$;

^b $wR_2 = \{\Sigma[w(F_o^2 - F_c^2)^2]/\Sigma[w(F_o^2)^2]\}^{1/2}$;

^c $\text{GOF} = \{\Sigma[w(F_o^2 - F_c^2)^2]/(n - p)\}^{1/2}$, where n is the number of reflections and p the total number of parameters refined.

Complex $[\text{Pd}(\text{L}^2)_2]\text{H}_2\text{O}$ crystallized in the $P2_1/n$ monoclinic centrosymmetric space group. The asymmetric unit cell of metal complex $[\text{Pd}(\text{L}^2)_2]\text{H}_2\text{O}$ consists of two crystallographically independent units (Figure 17) and 0.875 molecules of co-crystallised H_2O solvent. The crystallographic data containing bond length values and angle information are presented in Table 6.

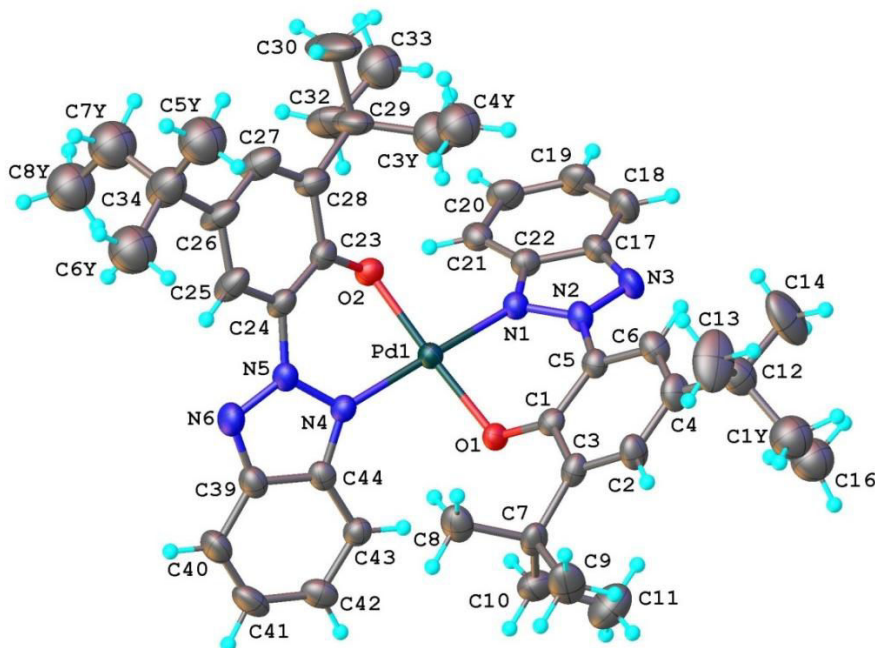


Figure 17. X-ray molecular structure of $[\text{Pd}(\text{L}^2)_2]\cdot 0.875\text{H}_2\text{O}$ with atom labeling representation and thermal ellipsoids at 30% probability level. Only one site of disordered fragments is shown.

Table 6. Selected bond lengths [\AA] and angles [$^\circ$] for $[\text{Pd}(\text{L}^2)_2]\text{H}_2\text{O}$.

$[\text{Pd}(\text{L}^2)_2]\text{H}_2\text{O}$		$[\text{Pd}(\text{L}^2)_2]\text{H}_2\text{O}$	
Pd1A–O1A	1.992(5)	Pd1B–O1B	2.001(5)
Pd1A–O2A	1.999(4)	Pd1B–O2B	1.984(5)
Pd1A–N1A	2.004(5)	Pd1B–N1B	2.003(5)
Pd1A–N4A	1.994(5)	Pd1B–N4B	2.001(5)
O1A–C1A	1.339(8)	O1B–C1B	1.326(8)
O2A–C23A	1.343(7)	O2B–C23B	1.337(8)
N1A–N2A	1.360(8)	N1B–N2B	1.333(7)
N2A–N3A	1.325(7)	N2B–N3B	1.321(7)
N4A–N5A	1.349(7)	N4B–N5B	1.354(7)
N5A–N6A	1.332(7)	N5B–N6B	1.317(8)
O1A–Pd1A–O2A	177.27(17)	O1B–Pd1B–O2B	176.22(19)

The N4-Pd1-N1 and O1-Pd1-O2 bond angles are 170.91(9) and 176.14(8), respectively. The Pd1-N1 and Pd1-N4 bond lengths are 2.001(2) Å and 2.013(2) Å. The Pd1-O1 and Pd1-O2 bond lengths of 1.995(2) Å and 1.999(2) Å are not within the standard deviation error different from the Pd-N bond lengths. The orientation of the two ligands within the complex is such that a single aryl ring of the 1-methyl-1-phenylethyl subunit appears to stack with benzotriazole unit of the opposite ligand. The shortest centroid-to-centroid distance is 3.56 Å as illustrated in Figure 19. The crystallographic data containing bond length values and angle information are presented in Table 7.

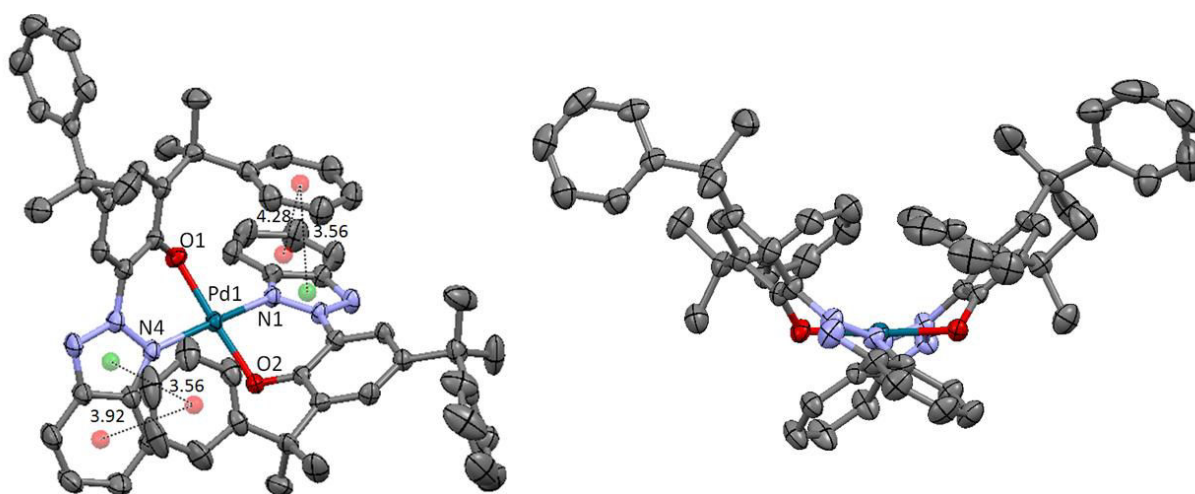


Figure 19. View of the molecular structure for $[\text{Pd}(\text{L}^3)_2]$ as 50% ellipsoids showing selected labelling of atoms and distances in Å (left) and a view down the N4-Pd1-N1 axis (right).

Table 7. Selected bond lengths [Å] and angles [°] for $[\text{Pd}(\text{L}^3)_2]$.

	$[\text{Pd}(\text{L}^3)_2]$
Pd1–O1	1.9953(17)
Pd1–O2	1.9990(17)
Pd1–N1	2.001(2)
Pd1–N4	2.013(2)
O1–C4	1.334(3)
O2–C31	1.335(3)
N1–N2	1.343(3)
N2–N3	1.323(3)
N4–N5	1.344(3)
N5–N6	1.326(3)

O1–Pd1–O2	176.14(8)
O1–Pd1–N1	92.47(8)
O1–Pd1–N4	87.52(8)
O2–Pd1–N1	87.00(8)
O2–Pd1–N4	93.61(8)
N1–Pd1–N4	170.91(9)

Compound $[\text{Pd}(\text{L}^3)_2](\text{CH}_3)_2\text{CO}$ crystallized in the $C2/c$ space group with 2 independent molecules in the asymmetric unit (Figure 20). The Pd atoms are lying on the 2-fold axis and their coordination sphere is identical to that of complex $[\text{Pd}(\text{L}^3)_2]$. Indeed the geometrical features observed in $[\text{Pd}(\text{L}^3)_2](\text{CH}_3)_2\text{CO}$ are comparable to those observed in $[\text{Pd}(\text{L}^3)_2]$, with 2 pairs of intra-molecular π -stacking interactions between the benzotriazoles and two phenyl groups, but the accessible sides of the Pd planes are now facing each other thus forming a pseudo dimer with the Pd1-Pd2 distance close to 4.2 Å. The crystallographic data containing bond length values and angle information are presented in Table 8.

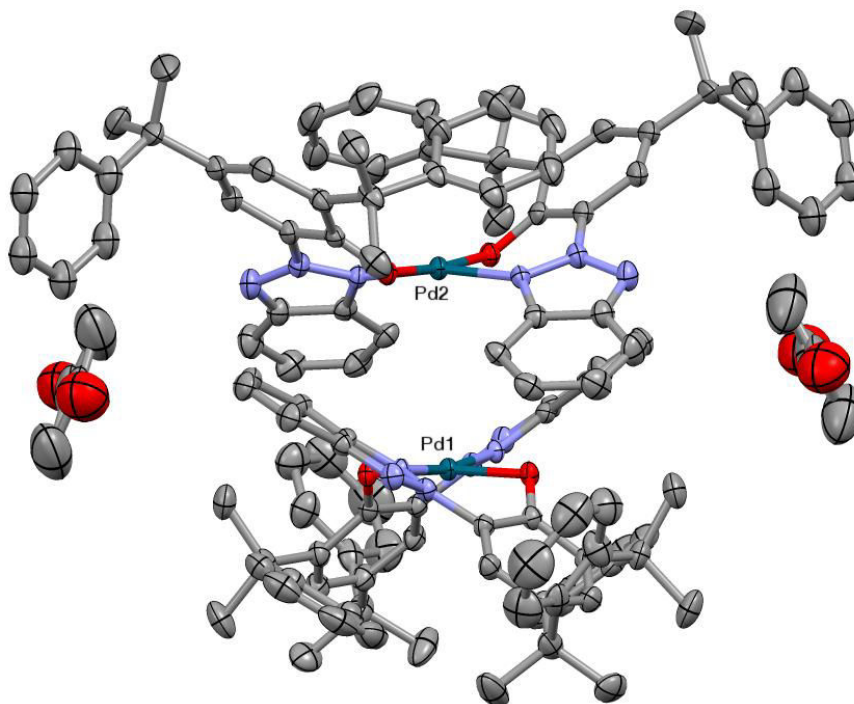


Figure 20. View of the molecular structure for $[\text{Pd}(\text{L}^3)_2]\cdot 0.5(\text{CH}_3)_2\text{CO}$ with the two disordered half acetone molecules. The ellipsoids are represented at the 30% probability level and the H-atoms are omitted for clarity.

Table 8. Selected bond lengths [Å] and angles [°] for $[\text{Pd}(\text{L}^3)_2](\text{CH}_3)_2\text{CO}$.

$[\text{Pd}(\text{L}^3)_2](\text{CH}_3)_2\text{CO}$	
Pd1–O1	1.9895(18)
Pd2–O2	1.9907(19)
Pd1–N3	1.999(2)
Pd2–N6	2.003(2)
O1–C12	1.325(3)
O2–C42	1.334(3)
N1–N2	1.322(3)
N1–N3	1.341(3)
N4–N5	1.321(4)
N4–N6	1.344(3)
O1 ¹ –Pd1–O1	174.34(11)
O1–Pd1–N3 ¹	91.90(8)
O1–Pd1–N3	88.60(8)
O1 ¹ –Pd1–N3 ¹	88.61(8)
O1 ¹ –Pd1–N3	91.90(8)
N3 ¹ –Pd1–N3	169.72(13)
O2 ¹ –Pd2–O2	174.38(11)
O2 ¹ –Pd2–N6 ¹	88.37(9)
O2–Pd2–N6	88.37(9)
O2–Pd2–N6	92.15(9)
O2 ¹ –Pd2–N6	92.15(9)
N6 ¹ –Pd2–N6	169.48(13)

¹-X,+Y,3/2-Z;

1.6. Cyclic voltammetry

The redox behavior of the complexes $[\text{Pd}(\text{L}^1)_2]$, $[\text{Pd}(\text{L}^2)_2]$ and $[\text{Pd}(\text{L}^3)_2]$ (Figure 21 – 23, Table 9) was studied by cyclic voltammetry in dry DMF at a glassy-carbon electrode using 0.1 M tetrabutyl-ammonium hexafluorophosphate (TBAPF₆, [Bu₄N][PF₆]) as the supporting electrolyte. All potentials are referred to Fe(Cp)₂⁺/Fc(Cp)₂ redox couple. The cyclic voltammogram in DMF is similar for all three complexes and also the redox behavior for all

three complexes is rather the same. Upon scanning to positive potentials two irreversible waves are observed at around $E_p^{a,3} = +0.74 - +0.83$ V and $E_p^{a,4} = +0.91 - +0.94$ V and are interpreted as ligand-based oxidation processes. The reduction side of the voltammogram shows one quasi-reversible wave at $E_{1/2}^2 = -1.51 - -1.59$ V (vs. $\text{Fc}(\text{Cp})_2^+/\text{Fc}(\text{Cp})_2$) and is associated with redox processes at the metal site and two irreversible redox signals at $E_p^{c,1} = -2.33 - -2.35$ V and at $E_p^{c,0} = -2.87$ V $- -2.92$ V which are associated with redox responses at $E_p^{a,1} = -0.23$ V $- -0.36$ V and $E_p^{a,0} = -1.09$ V $- -1.14$ V respectively.

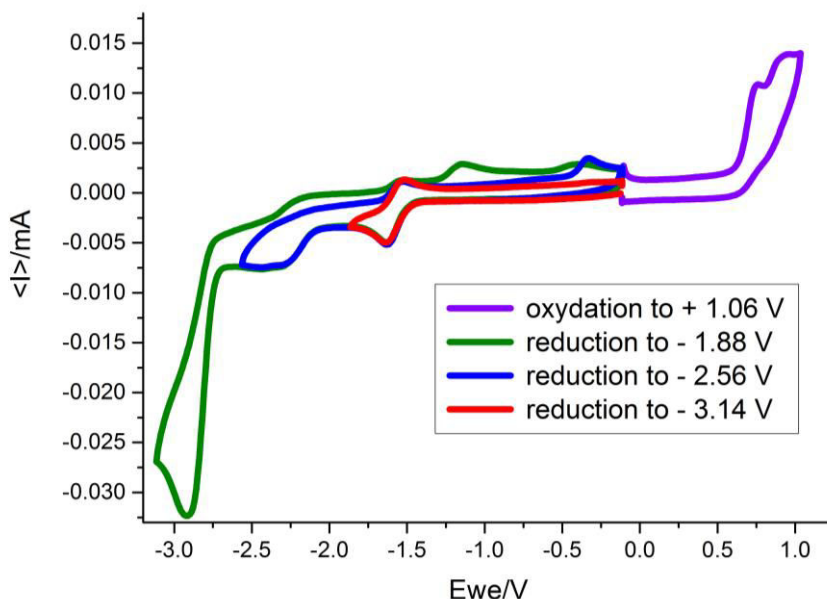


Figure 21. Cyclic voltammogram recorded for $[\text{Pd}(\text{L}^1)_2]$ in DMF containing 0.1M TBAPF_6 vs. Fc^+/Fc at a glassy carbon working electrode at different scan rates.

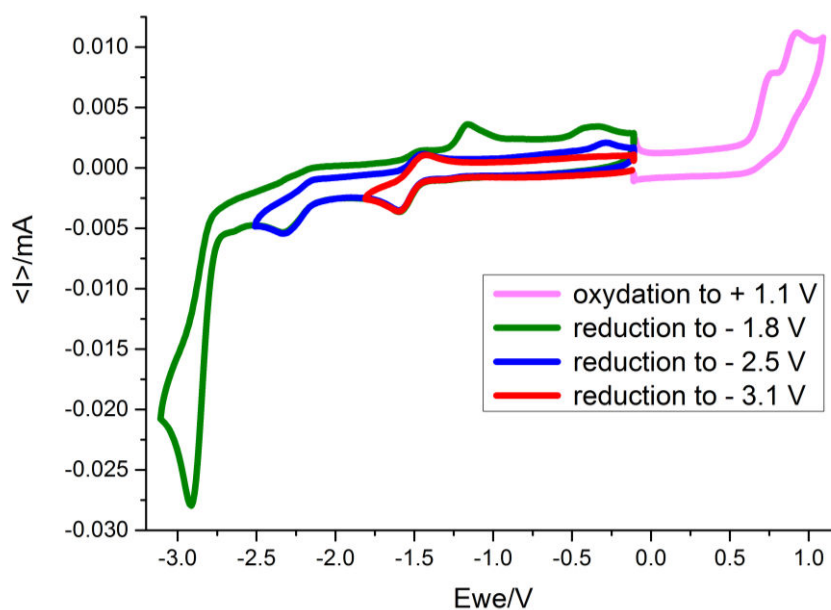


Figure 22. Cyclic voltammogram recorded for $[\text{Pd}(\text{L}^2)_2]$ in DMF containing 0.1M TBAPF_6 vs. Fc^+/Fc at a glassy carbon working electrode at different scan rates.

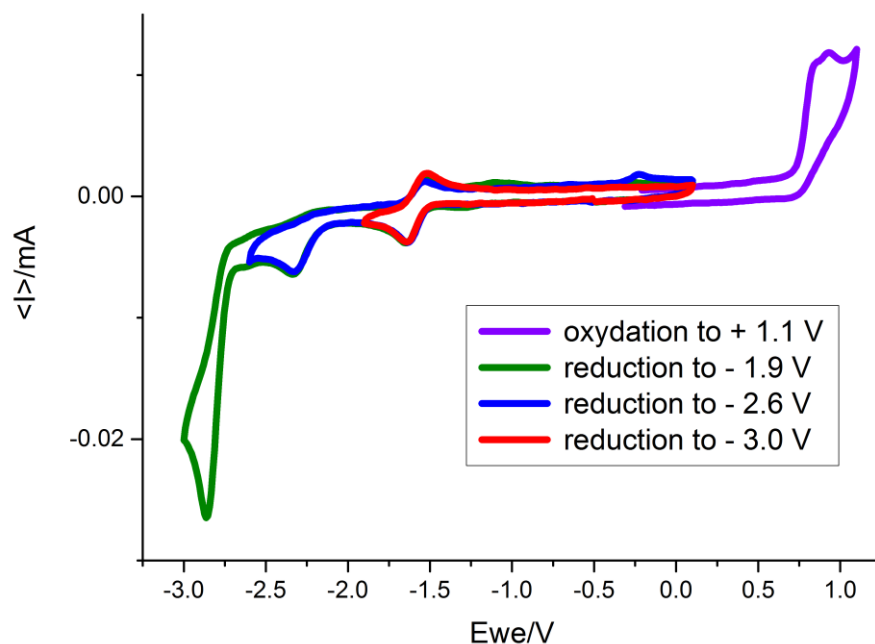


Figure 23. Cyclic voltamogram recorded for $[\text{Pd}(\text{L}^3)_2]$ in DMF containing 0.1M TBAPF₆ vs. Fc⁺/Fc at a glassy carbon working electrode at different scan rates.

Table 9. CV data for complexes.

	$E_p^{c,2}$	$E_p^{a,2}$	$E_{1/2}^2$	$E_p^{c,1}$	$E_p^{a,1}$	$E_p^{c,0}$	$E_p^{a,0}$	$E_p^{a,3}$	$E_p^{a,4}$
$[\text{Pd}(\text{L}^1)_2]$	-1.63	-1.52	-1.57	-2.35	-0.36	-2.92	-1.14	0.74	0.91
$[\text{Pd}(\text{L}^2)_2]$	-1.60	-1.42	-1.51	-2.33	-0.29	-2.92	-1.12	0.75	0.91
$[\text{Pd}(\text{L}^3)_2]$	-1,64	-1,54	-1.59	-2,34	-0,23	-2,87	-1,09	0,83	0,94

1.7. UV-Visible absorption spectroscopy

The room temperature electronic absorption spectra recorded for $[\text{Pd}(\text{L}^1)_2]$, $[\text{Pd}(\text{L}^2)_2]$ and $[\text{Pd}(\text{L}^3)_2]$ in DMF show two broad bands with absorption maxima λ_{max} at 310 and 390 nm for $[\text{Pd}(\text{L}^1)_2]$ and $[\text{Pd}(\text{L}^2)_2]$ and with λ_{max} at 305 and 395 nm for $[\text{Pd}(\text{L}^3)_2]$ (Figure 24). The relevant parameters are summarized in Table 10.

For complexes we can observe a minor shift for the first transition from 305 to 310 nm. The second transition present for ligands at 340-345 nm is absent in the case of palladium complexes. A new band at 390 nm appears and this is related to the coordination of the ligand to the metal.

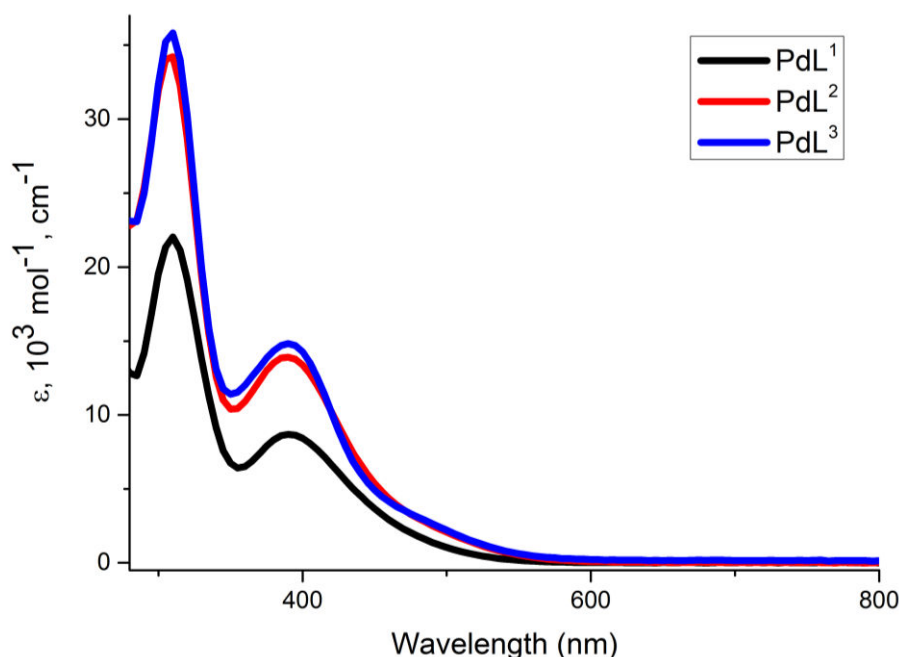


Figure 24. Electronic absorption spectra for complexes $[\text{Pd}(\text{L}^1)_2]$, $[\text{Pd}(\text{L}^2)_2]$ and $[\text{Pd}(\text{L}^3)_2]$.

Table 10. Absorption maxima λ_{max} and molar extinction coefficients ϵ of the UV-visible absorption of $[\text{Pd}(\text{L}^1)_2]$, $[\text{Pd}(\text{L}^2)_2]$ and $[\text{Pd}(\text{L}^3)_2]$ in DMF.

Complex	λ , nm (ϵ , $10^3 \text{ L mol}^{-1} \text{ cm}^{-1}$)	λ , nm (ϵ , $10^3 \text{ L mol}^{-1} \text{ cm}^{-1}$)
$[\text{Pd}(\text{L}^1)_2]$	310 (22.0)	390 (8.6)
$[\text{Pd}(\text{L}^2)_2]$	310 (34.2)	390 (13.9)
$[\text{Pd}(\text{L}^3)_2]$	305 (35.8)	395 (14.8)

1.8. Electrocatalysis

Since the redox behavior as well as the electronic absorption of all three complexes is rather the same, we have decided to study the electrocatalytic activity of our complexes in similar conditions. The addition of both trifluoroacetic acid and acetic acid as a proton source to complexes $[\text{Pd}(\text{L}^1)_2]$, $[\text{Pd}(\text{L}^2)_2]$ and $[\text{Pd}(\text{L}^3)_2]$ resulted in the formation of new catalytic waves in the cathodic region of the cyclic voltammograms (Figures 25 – 29). By using the “first derivative technique” was estimated the number and the potential of the formed waves. For complex PdL_3 (Figure S12) three waves can be observed within the potential range -1.1 V, -1.6 V and -1.8 V respectively. The current response increased with the addition of acid

and the maximum of the peak for complex **PdL₃** shifted from -1.5 V to -1.9 V vs. Fe(Cp)₂⁺/Fe(Cp)₂. The existence of 3 catalytic waves suggests competing parallel processes.

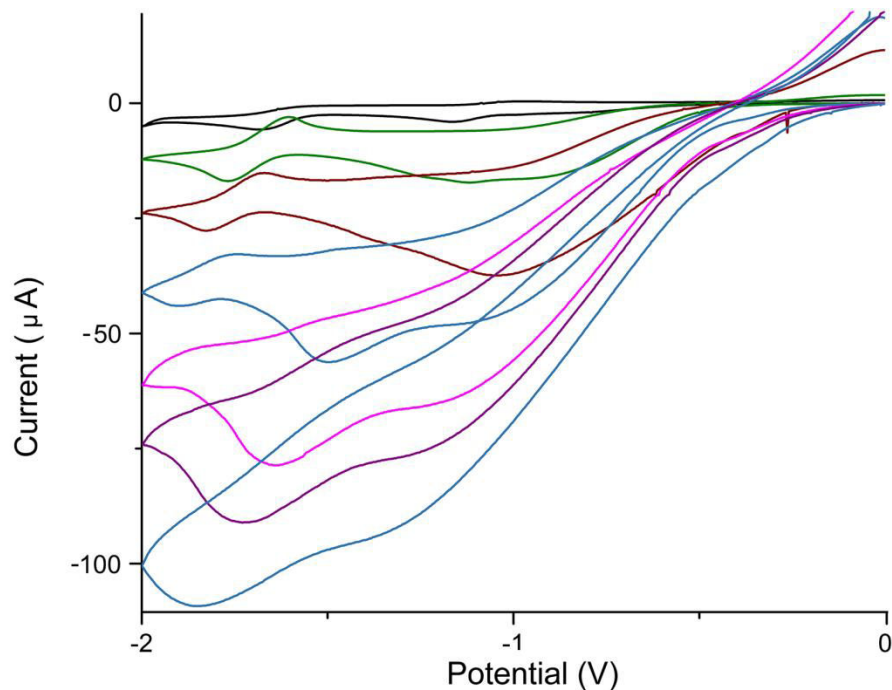


Figure 25. Selected cyclic voltammograms for **[Pd(L¹)₂]** (1 mM) at a glassy carbon electrode in dry DMF in the presence of increasing quantities of TFA. Voltammograms show that the addition of acid (0 – 20 eq) leads to the appearance of an irreversible wave of increasing amplitude corresponding to the reduction of protons catalyzed by the complex. Conditions: T = 298 K, scan rate 100 mV/s. Supporting electrolyte: 0.1M TBA.PF₆.

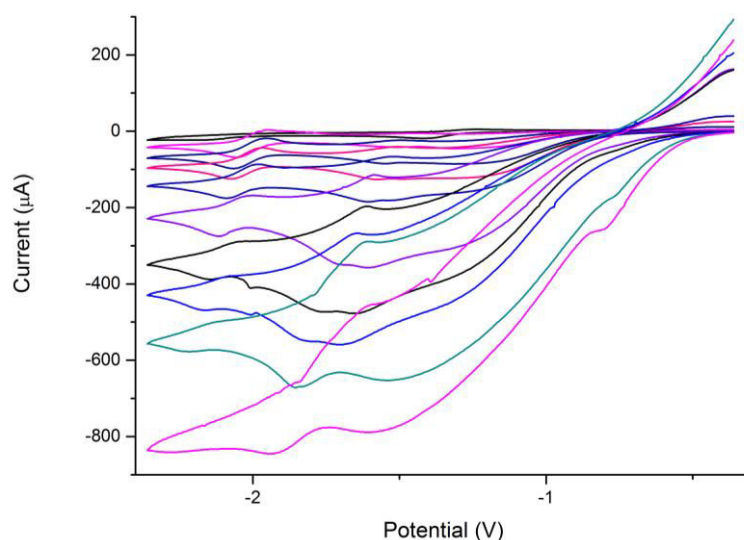


Figure 26. Selected cyclic voltammograms for $[\text{Pd}(\text{L}^2)_2]$ (1 mM) at a glassy carbon electrode in dry DMF in the presence of increasing quantities of TFA. Voltammograms show that the addition of acid (0 – 52 eq) leads to the appearance of an irreversible wave of increasing amplitude corresponding to the reduction of protons catalyzed by the complex. Conditions: $T = 298 \text{ K}$, scan rate 100 mV/s . Supporting electrolyte: 0.1M TBA.PF_6 .

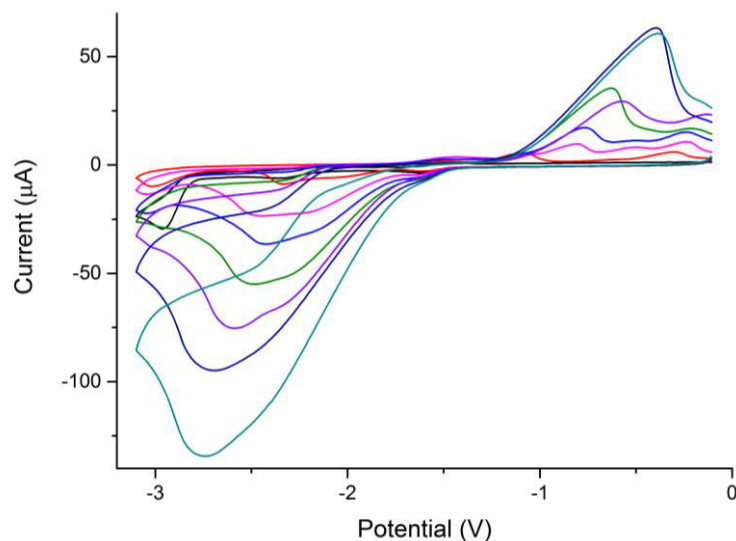


Figure 27. Selected cyclic voltammograms for $[\text{Pd}(\text{L}^2)_2]$ (1 mM) at a glassy carbon electrode in dry DMF in the presence of increasing quantities of Acetic Acid. Voltammograms show that the addition of acid (0 – 90 eq) leads to the appearance of an irreversible wave of increasing amplitude corresponding to the reduction of protons catalyzed by the complex. Conditions: $T = 298 \text{ K}$, scan rate 100 mV/s . Supporting electrolyte: 0.1M TBA.PF_6 .

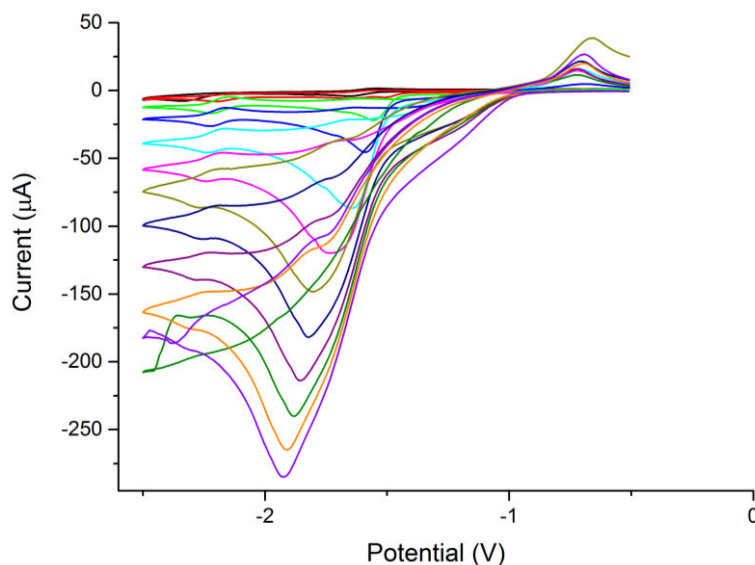


Figure 28. Selected cyclic voltammograms for $[\text{Pd}(\text{L}^3)_2]$ (1 mM) at a glassy carbon electrode in dry DMF in the presence of increasing quantities of TFA. Voltammograms show that the addition of acid (0 – 90 eq) leads to the appearance of an irreversible wave of increasing amplitude corresponding to the reduction of protons catalyzed by the complex. Conditions: T = 298 K, scan rate 100 mV/s. Supporting electrolyte: 0.1M TBA.PF₆.

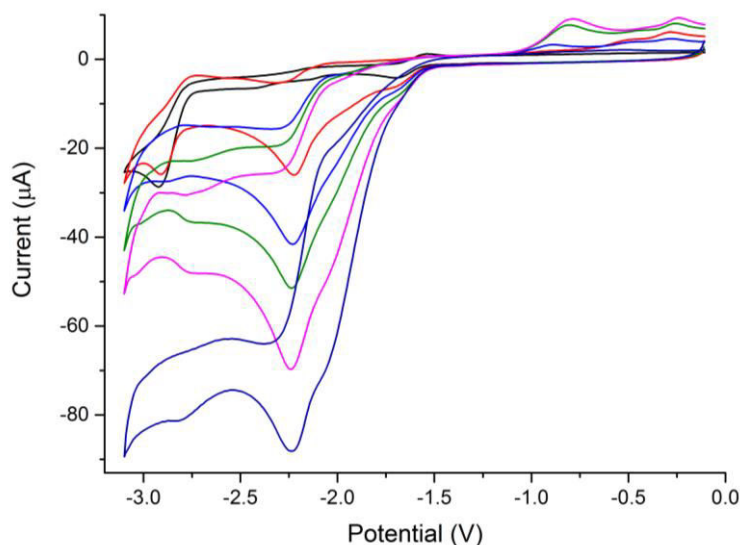


Figure 29. Selected cyclic voltammograms for $[\text{Pd}(\text{L}^3)_2]$ (1 mM) at a glassy carbon electrode in dry DMF in the presence of increasing quantities of Acetic Acid. Voltammograms show that the addition of acid (0 – 25 eq) leads to the appearance of an irreversible wave of increasing amplitude corresponding to the reduction of protons catalyzed by the complex. Conditions: T = 298 K, scan rate 100 mV/s. Supporting electrolyte: 0.1M TBA.PF₆.

1.9. Calculation of number of electrons involved in the first reduction process

From Randles-Sevcik equation (https://en.wikipedia.org/wiki/Randles-Sevcik_equation) was calculated the number of electrons involved in the red-ox process for complex $[\text{Pd}(\text{L}^3)_2]$.

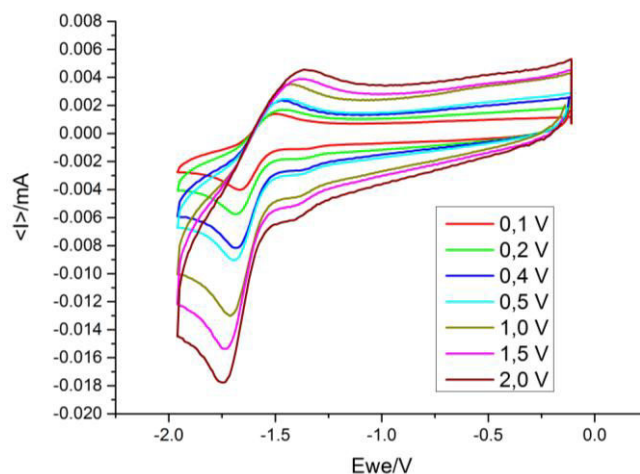


Figure 30. Cyclic voltammogram of 1 mM $[\text{PdL}_3]$ solution at different scan rates.

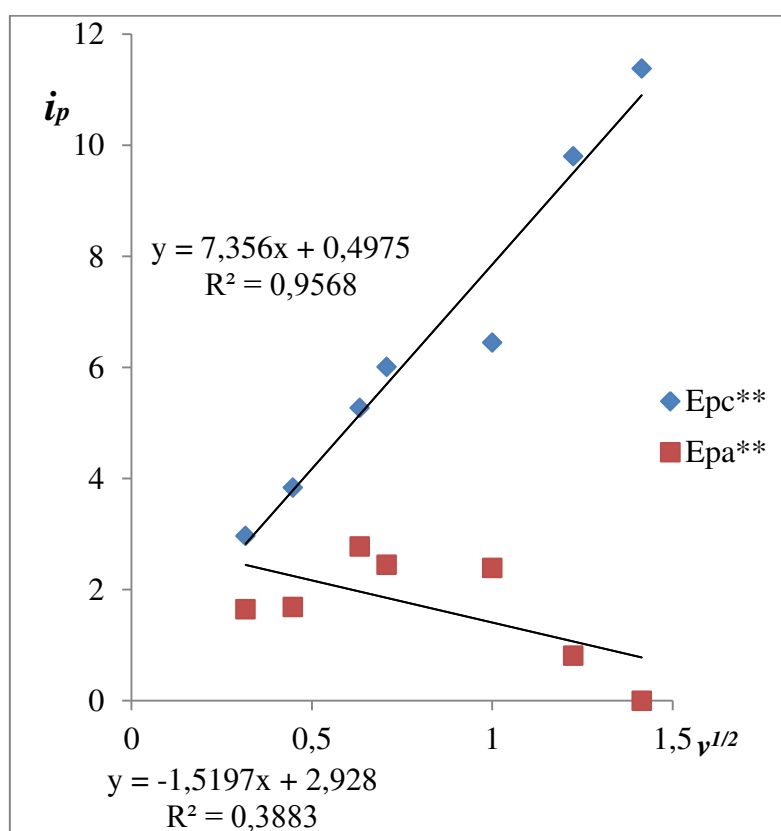


Figure 31. Linear plots of current maximum values in dependence of square root of scan rates.

As we can see from Figure 30, for the cathodic process the dependence is linear but it is not for anodic. This tells us that we can calculate the number of electrons involved only for cathodic process, by using the value of the slope (7.356) as $i_p/v^{1/2}$ in the *Randles-Sevick equation*.

In this way we obtained the value for the number of transferred electrons $n = 1,000591818$ so the reduction of the complex is a one electron process.

1.10. One-electron reduced species generation and characterization

Chemical reduction of $[\text{Pd}(\text{L}^3)_2]$ complex in DMF and THF at RT was realized by adding 1 equiv. NaHg (10%) as one-electron reductant with the reduction potential of -2.07 V (in THF). The EPR samples were collected, frozen in liquid nitrogen and measured at 120 K.

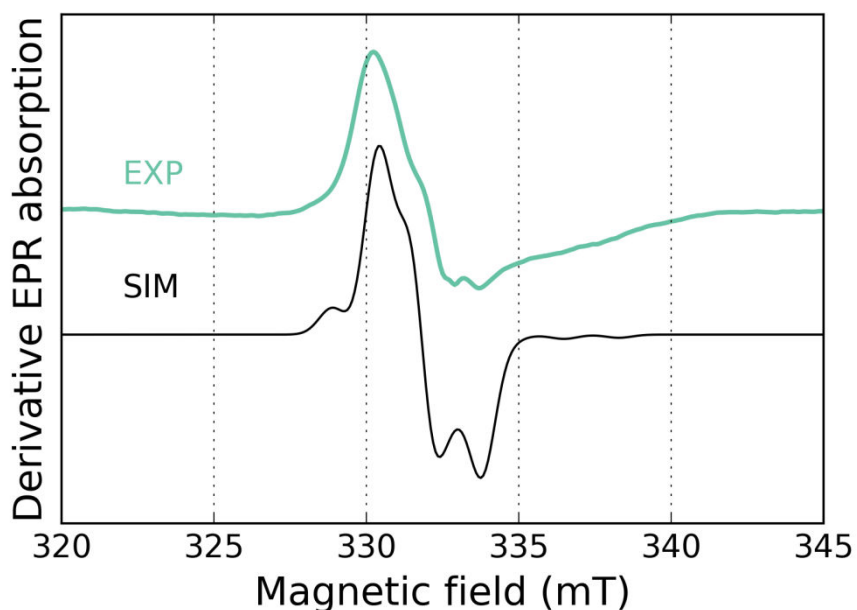


Figure 32. EPR spectra of the neutral $[\text{Pd}(\text{L}^3)_2]$ complex and chemically reduced species with 1 equiv. NaHg (10%) in THF at RT.

The $[\text{Pd}(\text{L}^3)_2]$ complex is EPR silent. As can be seen in Figure 32, the EPR active species is the reduced one which was generated from THF solution.

By generating the one-electron reduced species we have two possibilities:

1. The reduction could be metal-centered with the formation of Pd(I)-L complex or
2. The reduction could be ligand-based with the formation of Pd(II)-L^{•-} radical

To determine which is the case, we performed theoretical calculations which suggested that the first reduction is on the metal, with the formation of a Pd(I) complex.

1.11. Theoretical calculations

The structure of the neutral, monoreduced and monoxydized were first subjected to geometry optimization (Figure 33). Comparison of the DFT-optimized structure of [PdL₃] with the X-ray data showed a pretty good agreement between the two sets of data which confirmed that [PdL₃] can be best described as a diamagnetic square planar Pd(II) complex ([PdL₃], S = 0). The reduced [PdL₃] complex was described as a Pd(I) paramagnetic species, S = ½. The elongation of Pd-N and Pd-O bond lengths suggests that the reduction occurs on the metal. In the case of the oxidized [PdL₃] complex we observed the presence of paramagnetic Pd(II)-ligand radical species S = ½. The oxidation occurs on the ligand since O-C and C-C bond lengths of the phenolate groups are affected.

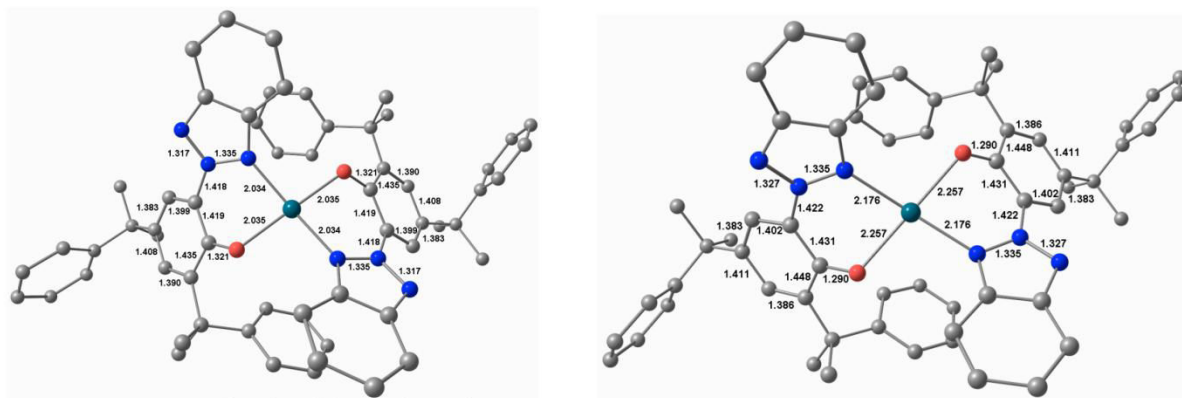


Figure 33. DFT-optimized structure of neutral PdL₃ complex (left) and mono reduced PdL₃ complex (right) (hydrogen atoms were omitted for clarity).

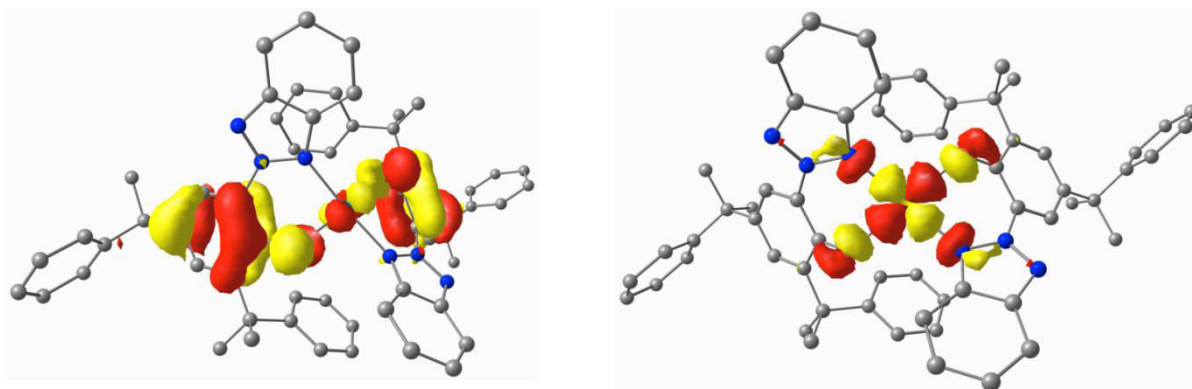


Figure 34. HOMO (left) and LUMO (right) for neutral $[\text{PdL}_3]$ complex.

The performed DFT calculations show that in the base HOMO state, electronic density is centered on the phenolate groups of the ligand. In the LUMO excited state, the electron density is centered on the metal and its coordination sphere (Figure 34).

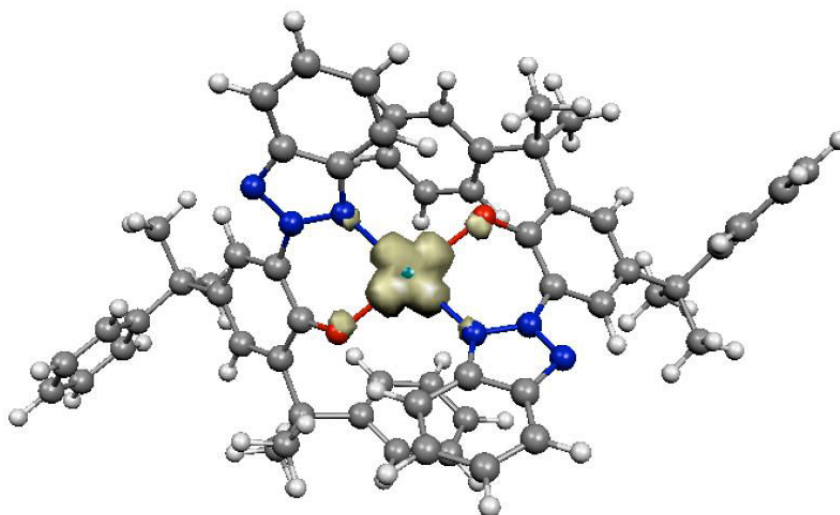


Figure 35. Spin density plot of the reduced $[\text{PdL}_3]$ complex.

The spin density plot of the reduced $[\text{PdL}_3]$ complex (Figure 35) shows that positive spin populations are found both at the Pd center and its coordinating O- and N-atoms which is a proof of a metal centered process for the reduction

1.12. Gas analysis

A continuous flow-rig with in-line GC analysis was used to detect the molecular hydrogen produced during electrocatalytic proton reduction in DMF in the presence of TFA.³⁹ Applying a potential of -0.36 V vs. NHE to the boron doped diamond working electrode resulted in immediate formation of molecular hydrogen (Figure 36). The rate of H_2 produced was determined by calibration with a known flow rate of a H_2/Ar mixture by checking the proportionality between the peak area and the volume of injected hydrogen per minute. When no catalyst was employed no hydrogen was detected during five hours of electrolysis. The presence of 1 mM of the catalyst resulted in three orders of magnitude increase of current at the same applied potential and immediate constant production of hydrogen as indicated by the GC analysis. Almost seven turnovers were reached after five hours of electrolysis and no sign of hydrogen production decrease was observed at the end of this time. At the same time a quite low constant Faradaic yield of about 50% was obtained. As the amount of hydrogen evolved per minute did not change significantly during electrolysis the decomposition of catalyst could not be the major factor contributing to the low Faradaic yield. The UV-Vis spectrum and the cyclic voltammogram of the electrolysis solution did not change significantly during electrolysis. This would suggest that the low Faradaic yield of the detected hydrogen is more likely to be a result of substrate reduction. Palladium complexes are well known catalysts for chemical and electrochemical hydrogenation of organic compounds¹⁵. As the produced hydrogen cannot be removed immediately from the solution hydrogenation of the electrolysis mixture components is quite likely. Another explanation is the direct reduction of the substrate by the Pd catalyst. When acetic acid was used as the proton source no hydrogen evolution was observed at -0.36 V vs. NHE . Small amount of hydrogen was detected only after application of -0.7 V vs. NHE .

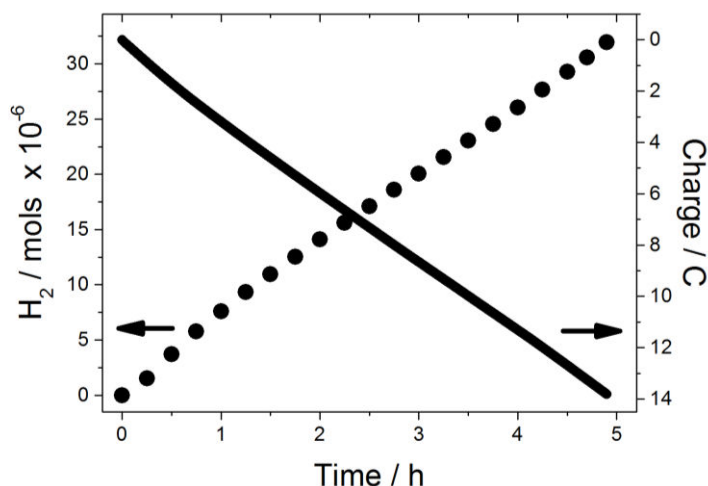


Figure 36. Electrocatalytic hydrogen production vs. time and charge vs. time by applying -0.36 V vs. NHE to a glassy carbon electrode in 0.1 M TBAPF₆ solution of DMF containing 90 mM TFA and 1 mM [Pd(L³)₂] complex.

Based on the obtained data, the calculated overpotential is 100 mV. This shows us that [Pd(L³)₂] complex is the best known palladium based catalyst in hydrogen evolution reactions.

1.13. Conclusions to Chapter 1

Three new Pd(II) complexes with benzotriazol-phenolic ligands were synthesized and characterized by physico-chemical methods such as: X-ray, NMR, elemental analysis, mass spectrometry, UV-visible spectroscopy, theoretical calculations and electrochemistry. The one electron reduced species were isolated and characterized by UV-visible spectroscopy, EPR and DFT calculations.

In the presence of acid used as source of protons appears an irreversible signal in the reduction area. The intensity of the signal is proportional to the concentration of added acid. In the case of trifluoroacetic acid the signal appears at the potential of the first redox process which suggests a mechanism involving the formation of a metal based reduced active species while in the case of a weaker acetic acid the signal appears at the potential characteristic to the second red-ox process which indicates that the mechanism implies the formation of a ligand based reduced active species. In the case of TFA, the protonation occurs at the monoreduced complex but in the case of acetic acid, requires a double reduction. Molecular modelling is needed to prove the nature of the redox process.

CHAPTER 2

Copper complexes with benzotriazolyl phenolate ligands.

2.1. Introduction

Copper is an important metal in the nature. There are known many types of copper metalloenzymes as shown in Figure 37.

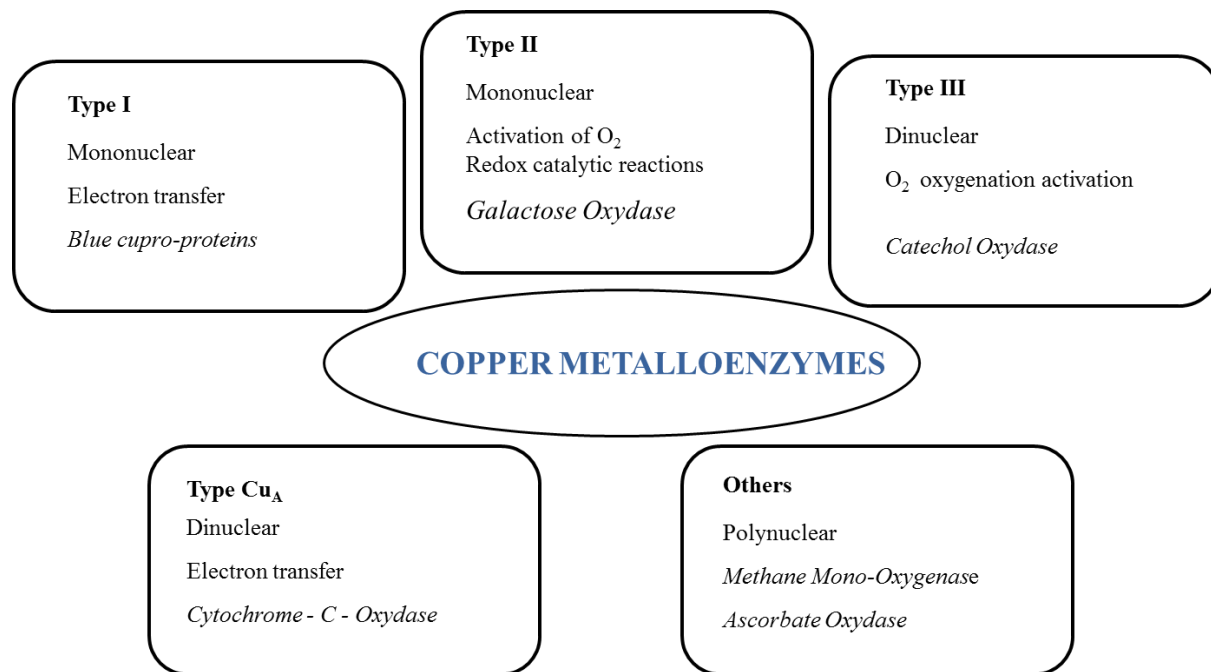


Figure 37. Classification of copper metalloenzymes.

Mononuclear metalloenzymes of type I and type II are involved in electron transfer processes and catalytic or redox active processes respectively. As shown in Table 11, the mononuclear copper metalloenzymes have different coordinating atoms in the inner coordination sphere and also have some specific spectroscopic properties (EPR, UV-vis).

Table 11. Characteristics of mononuclear copper metallo enzymes.

	Type I	Type II
State	Mononuclear	Mononuclear
Biological Function	Electron Transfer	Catalysis, redox activity
Examples of enzymes	Plastocyanine, azurine	Galactose oxydase, superoxyde dismutase

Coordinating atoms	S ⁻ (Cys), 2 N (His), S (Met)	In general 3 N (His) + 1 vacant site
EPR	Weak hyperfine coupling	In general classic for a Cu(II) system
UV-Vis	LMCT Cys ⁻ → Cu(II)	Without an intense LMCT

Due to their important biological relevance, metal-associated phenoxyl radicals have received much attention from chemists over a period of several decades.^{40,41} Among the metalloenzymes where tyrosine residues play a redox non-innocent role, the copper-radical oxidases (CROs) family are prominent.⁴² In the CROs family, glyoxal oxidase (GlyOX),^{43,44} galactose oxidase (GalOX)^{45,46} and alcohol oxidases (AlcOX)⁴⁷ are of much interest since these enzymes catalyze oxidations of aldehydes (GlyOX) or alcohols (GalOX and AlcOX)^{46,48} which are chemical transformations at the basis of several biotechnological applications.⁴⁹

The active site of the CROs is composed of a copper center coordinated by five ligands in a square pyramidal geometry: Tyr₂₇₂, His₄₉₆, His₅₈₁ and a water molecule form the square plane. At a longer distance, Tyr₄₉₅ is the fifth axial ligand (Figure 38A). The active species is the copper(II)-tyrosyl radical (Figure 38B) that is responsible for the oxidation of the substrate by H-atom transfer to the tyrosyl radical and electron transfer to the copper center leading to copper(I)-tyrosine species. The regeneration of the copper(II)-tyrosyl radical occurs by reaction of the copper center with dioxygen leading to the formation of hydrogen peroxide. The CROs family has inspired many chemists who reproduced their coordination sphere including a phenoxy-radical copper moieties,⁵⁰⁻⁵⁵ but also their reactivity in aerobic oxidation of various substrates such as alcohol, amines or phenolic compounds.⁵⁶ Paradoxically, the reactivity of these model complexes has rarely been exploited in the oxidative DNA cleavage. The development of artificial metallonucleases able to cleave DNA by an oxidative process is of high interest due to their potential applications in biology and medicine.⁵⁷ Recently, Klein *et al.* have reported a new copper(II) complex based on a triazole-phenolate type ligand which produces a quite stable phenoxyl-radical bound to copper(II).⁵⁸ In the perspective of the development of phenoxyl-radical copper(II) complexes that mediate oxidative DNA cleavage, we report on the synthesis and the characterization of a copper(II) complex based on a triazole-phenolate type ligand. The chemical generation of its phenoxy-radical copper species and its evaluation as alcohol oxidant or nuclease are also described.

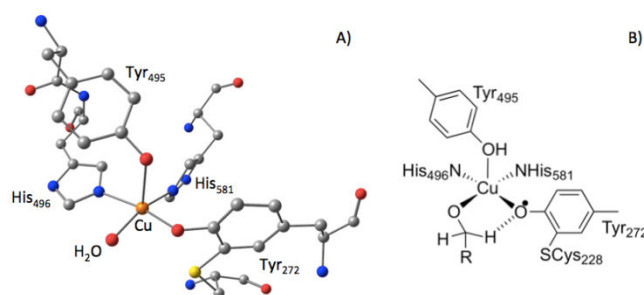


Figure 38. A) Active site of GalOX (PDB: 1GOG) with water molecule as fifth ligand (H atoms removed for clarity). B) Cu-tyrosyl radical intermediate involved in alcohol oxidation.

From the point of view of coordination chemistry, benzotriazolyl phenols could be interpreted as a class of lipophilic proligands containing the π -delocalized bidentate N^-O monoanionic moiety.

The coordination of this class of ligands occurs through the deprotonated N^-O site.

Benzotriazolyl phenols began to be employed as proligands recently, a copper coordination compound with benzotriazolyl phenol ligand (Figure 39) was reported for the first time almost two decades ago.³⁷ It was a copper(I) dinuclear complex which was designed as photosensitizer to assist the norbornadiene (NBD) \rightarrow quadricyclene (Q) isomerization with the purpose of carrying out the reaction using visible light and achieving high NBD/photocatalyst turnover.

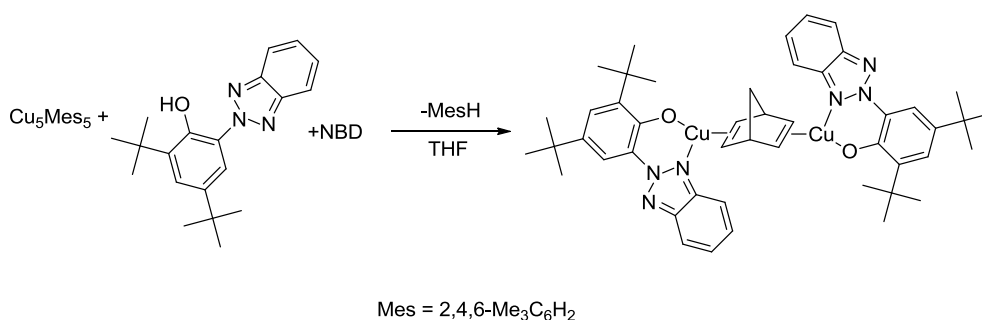


Figure 39. Synthetic route for the copper(I) benzotriazolyl phenol complex reported by Franceschi et al.³⁷

A copper(II) coordination compound with benzotriazolyl phenol ligand (Figure 40) was reported for the first time 15 years later by Butsch et al.⁵⁸

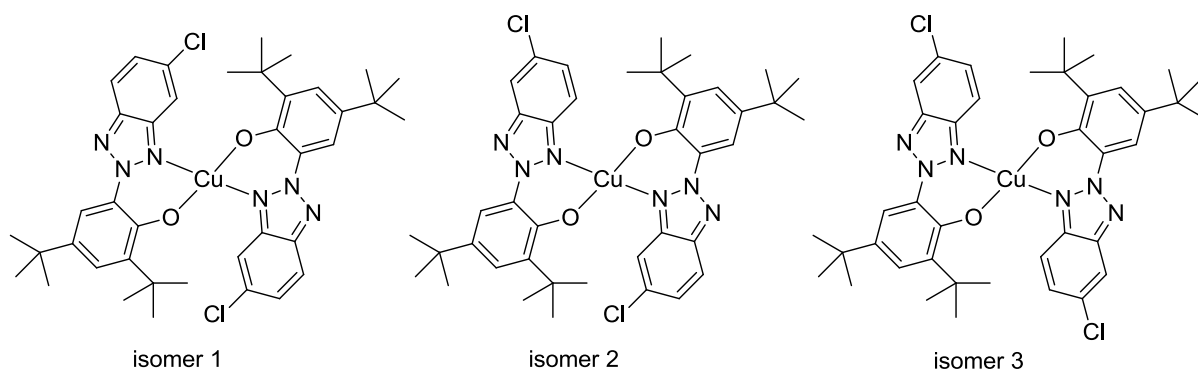


Figure 40. Structural representation for the three isomers of the copper(II) benzotriazolyl phenol complex reported by Butsch *et al.*⁵⁸

As can be seen from Figure 40, in the mononuclear copper(II) complex, the central metal site coordinates to two molecules of the 2,4-di(*t*Bu)-6-(5-chloro-2*H*-benzo-*[d]*[1,2,3]triazol-2-yl)phenol ligand through N⁻O deprotonated site forming a square planar complex which crystallises as a mixture of 3 possible isomers.

The catalytic tests in benzyl alcohol oxidation by Butsch complex were undertaken for the active species $[\text{Cu}(\text{triaz})_2]^+$ generated by the disproportionation reaction performed in MeCN/toluene mixture in the presence of base.

Other copper(II) complexes with benzotriazolyl phenol ligands were reported by Li *et al.*⁵⁹

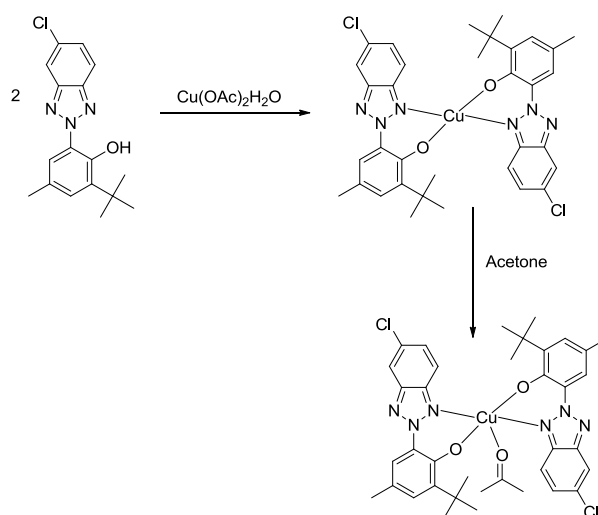


Figure 41. Synthetic route for the copper(II) benzotriazolyl phenol complexes reported by Li *et al.*⁵⁹

In the case of Li's complexes (Figure 41) the coordination occurs in a similar way as for Butsch complex (Figure 40), namely the monomeric homoleptic complex with a four-coordinated copper center incorporated by two *N,O*-bidentate ligands, forming two six-

membered chelating rings in a twisted conformation, is displaced in a distorted square planar geometry. It should be mentioned that a copper complex (Figure 41) as an acetone adduct, is reported for the first time, as well as the formation of a pentacoordinated copper(II) benzotriazolyl phenol complex.⁵⁹

Li's complexes were employed as catalysts for lactide polymerization in the presence of various alcohol initiators.

It is interesting to notice the fact that benzotriazolyl phenol ligand were also employed as building blocks for the preparation of some bulkily decorated phthalocyanines (Figure 42).⁶⁰

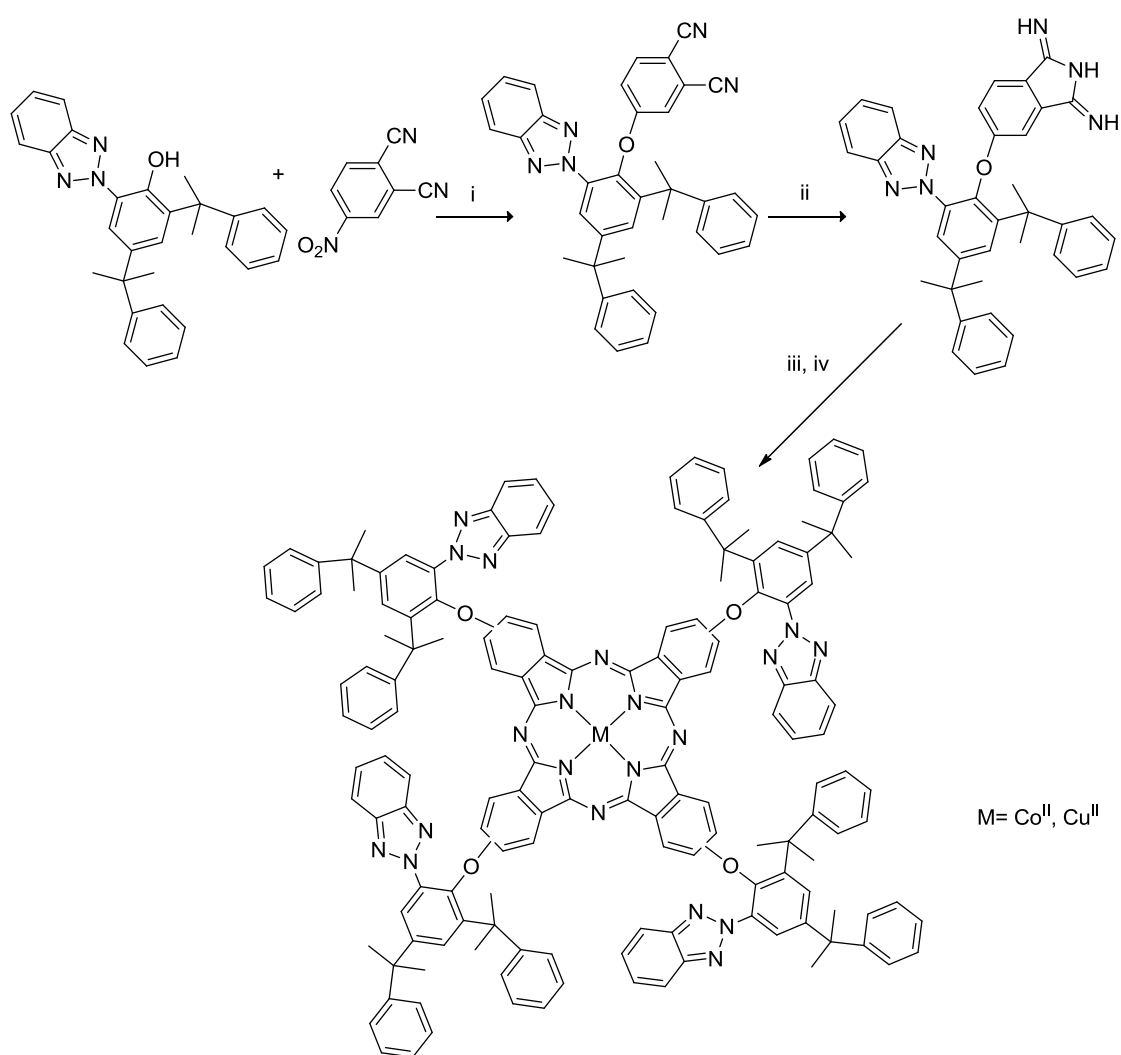


Figure 42. Copper(II) phthalocyanine⁶⁰

Copper(II) phthalocyanine coordination compound turned out to exhibit good optical limiting performances which can be attributed to the effectiveness of peripheral side groups as a result of the improved electron mobility.

2.2. Preparation of the Cu(II) coordination compounds

The synthesis of copper(II) coordination compounds with benzotriazolyl phenol ligands is known to be an easy procedure with high resulting yields. This could be realized *via* two methods. Method 1 consists in the direct reaction between the copper salts with the ligand at high temperature, usually at reflux during 24 hours⁵⁹. Method 2 is the interaction of copper(II) salt with the previously deprotonated ligand by using triethylamine as a base at room temperature.⁵⁸

The copper(II) complex $[\text{Cu}(\text{L}^2)_2]$ (Figure 43) was obtained by mixing 2 equivalent of HL^2 either with one equivalent of copper(II) acetate in ethanol under reflux (method 1) or with one equivalent of copper(II) triflate in a 5:3 acetonitrile:toluene mixture at r.t in the presence of 2 equivalent of base (method 2). As base were used triethylamine, sodium hydride or sodium hydroxide, in all these cases we isolated complex $[\text{Cu}(\text{L}^2)_2]$ in good yield. The complexes $[\text{Cu}(\text{L}^2)_2\text{DMF}]$, $[\text{Cu}(\text{L}^2)_2\text{DMA}]$ and $[\text{Cu}(\text{L}^2)_2\text{DMSO}]$ were prepared by mixing 2 equivalents of HL^2 with 1 equivalent of copper(II) acetate in *N,N*-dimethylformamide, *N,N*-dimethylacetamide or dimethyl sulfoxide upon heating. The recrystallization of $[\text{Cu}(\text{L}^2)_2]$ in *N,N*-dimethylformamide, *N,N*-dimethylacetamide or dimethyl sulfoxide also affords $[\text{Cu}(\text{L}^2)_2\text{DMF}]$, $[\text{Cu}(\text{L}^2)_2\text{DMA}]$ and $[\text{Cu}(\text{L}^2)_2\text{DMSO}]$ respectively as crystalline compounds. The chemical composition of $[\text{Cu}(\text{L}^2)_2]$, $[\text{Cu}(\text{L}^2)_2\text{DMF}]$ and $[\text{Cu}(\text{L}^2)_2\text{DMA}]$ were confirmed by single crystal X-ray diffraction (Figures 44 – 46), ESI-MS, and CHN analysis. The single crystals of $[\text{Cu}(\text{L}^2)_2\text{DMSO}]$ were too small to be suitable for X-ray diffraction analysis and the chemical composition was confirmed by CHN analysis.

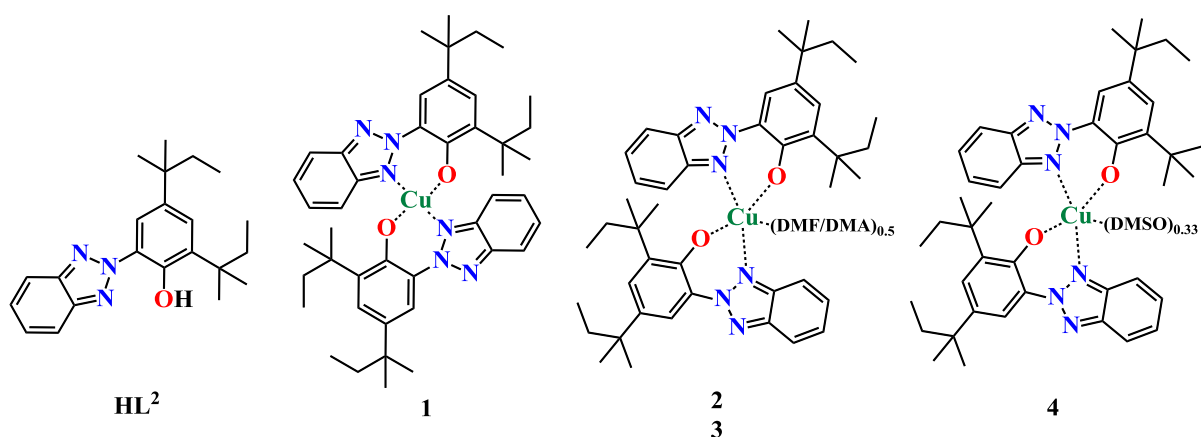


Figure 43. Formula of the ligand (HL^2) and complexes $[\text{Cu}(\text{L}^2)_2]$, $[\text{Cu}(\text{L}^2)_2\text{DMF}]$, $[\text{Cu}(\text{L}^2)_2\text{DMA}]$ and $[\text{Cu}(\text{L}^2)_2\text{DMSO}]$.

2.3. Structural characterisation of the Cu(II) complexes

Suitable crystals for single crystal X-ray diffraction study of complexes $[\text{Cu}(\text{L}^2)_2]$, $[\text{Cu}(\text{L}^2)_2\text{DMF}]$ and $[\text{Cu}(\text{L}^2)_2\text{DMA}]$ were grown by slow evaporation of the $\text{CH}_3\text{CN}/\text{toluene}$ (5:3) solution for $[\text{Cu}(\text{L}^2)_2]$, DMF for $[\text{Cu}(\text{L}^2)_2\text{DMF}]$ and DMA for $[\text{Cu}(\text{L}^2)_2\text{DMA}]$. All the experimental details of the structure determinations are given in Table 12 and the distances and angles of the coordination sphere of the copper center are reported in Table 12 as well. Complexes $[\text{Cu}(\text{L}^2)_2]$, $[\text{Cu}(\text{L}^2)_2\text{DMF}]$ and $[\text{Cu}(\text{L}^2)_2\text{DMA}]$ have a molecular structure in the crystal consisting of neutral molecules. Complex $[\text{Cu}(\text{L}^2)_2]$ crystallizes in the triclinic centrosymmetric space group P-1, while complexes $[\text{Cu}(\text{L}^2)_2\text{DMF}]$ and $[\text{Cu}(\text{L}^2)_2\text{DMA}]$ crystallize in the monoclinic space group $\text{P}2_1/c$. Crystals of complex $[\text{Cu}(\text{L}^2)_2]$ appeared to be twinned but the two domains could be integrated separately and used in the refinement process with calculated respective contributions equal to 0.7 and 0.3 for the major and minor domains respectively. Copper-atom in complex $[\text{Cu}(\text{L}^2)_2]$ has a distorted square planar geometry provided by two N-atoms and two O-atoms from two ligand molecules (Figure 45). For complexes $[\text{Cu}(\text{L}^2)_2\text{DMF}]$ and $[\text{Cu}(\text{L}^2)_2\text{DMA}]$, a solvent molecule of DMF or DMA, respectively, is coordinated to the copper center. DMF(DMA) was found to lie on a center of inversion and its occupancy factor was fixed to 0.5. In the crystal, two molecules of complex associate together through hydrophobic interactions between the four *t*-pentyl substituents forming thus a cage that encapsulate a DMF(DMA) molecule (Figure 43). Some terminal moieties for $[\text{Cu}(\text{L}^2)_2\text{DMF}]$ and $[\text{Cu}(\text{L}^2)_2\text{DMA}]$ were found to be disordered and refined on two sites of occupancies equal to 0.65 and 0.35 for $[\text{Cu}(\text{L}^2)_2\text{DMF}]$ and 0.8 and 0.2 for

[Cu(L²)₂DMA]. Compounds **[Cu(L²)₂DMF]** and **[Cu(L²)₂DMA]** are isostructural and consist of one [CuL₂(DMF)_{0.5}] or [CuL₂(DMA)_{0.5}] unit with a penta-coordinated geometry provided by two nitrogen atoms and two O-atoms of the two ligand molecules and an O-atom from dimethylformamide / dimethylacetamide solvent (Figure 46). The Addison parameter calculations reveal that these coppers are in a distorted geometry between square planar and trigonal bipyramid: $\tau = 0.48$ and 0.5 for **[Cu(L²)₂DMF]** and **[Cu(L²)₂DMA]**, respectively.⁶¹

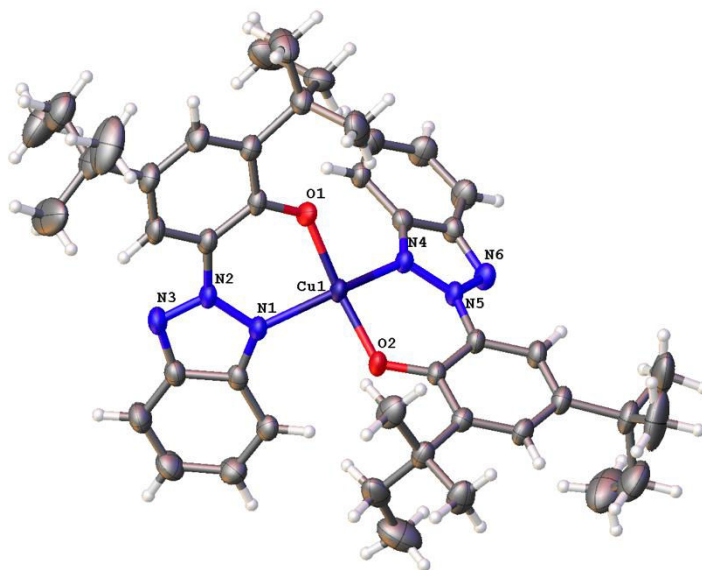


Figure 44. View of the molecule of **[Cu(L²)₂]** with some atom labeling and ADP's at 50% probability level.

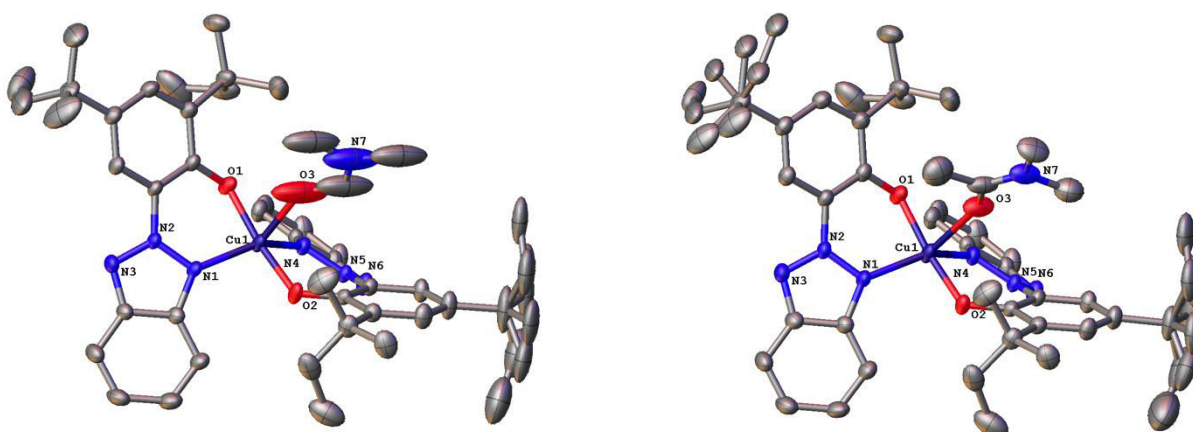


Figure 45. View of the molecule **[CuL₂(DMF)_{0.5}]** **[Cu(L²)₂DMF]**, left, and **[CuL₂(DMA)_{0.5}]** **[Cu(L²)₂DMA]**, right, with some atom labeling and ADP's at 50% probability level. Hydrogen atoms were omitted for clarity.

Table 12. Crystallographic data for copper compounds $[\text{Cu}(\text{L}^2)_2]$, $[\text{Cu}(\text{L}^2)_2\text{DMF}]$ and $[\text{Cu}(\text{L}^2)_2\text{DMA}]$.

Compound	$[\text{Cu}(\text{L}^2)_2]$	$[\text{Cu}(\text{L}^2)_2\text{DMF}]$	$[\text{Cu}(\text{L}^2)_2\text{DMA}]$
Empirical formula	$\text{C}_{44}\text{H}_{56}\text{CuN}_6\text{O}_2$	$\text{C}_{45.5}\text{H}_{59.5}\text{CuN}_{6.5}\text{O}_{2.5}$	$\text{C}_{46}\text{H}_{60.5}\text{CuN}_{6.5}\text{O}_{2.5}$
Formula weight (g/mol)	764.48	801.03	808.05
Crystal system	triclinic	monoclinic	monoclinic
Space group	P-1	$\text{P2}_1/\text{c}$	$\text{P2}_1/\text{c}$
<i>Unit cell dimensions</i>			
a (Å)	11.0580(3)	10.90460(12)	10.9103(2)
b (Å)	13.7352(5)	29.8272(3)	30.0207(7)
c (Å)	14.1678(5)	13.24480(15)	13.2449(3)
α (°)	92.680(3)		
β (°)	102.350(3)	95.6462(10)	95.9118(18)
γ (°)	98.873(3)		
Volume (Å ³)	2069.83(12)	4287.02(8)	4315.11(15)
Z	2	4	4
λ (Å)	1.54184	1.54184	1.54184
$\rho_{\text{calc.}}$ (g/cm ³)	1.227	1.241	1.244
Crystal size (mm ³),	$0.38 \times 0.05 \times 0.02$	$0.28 \times 0.18 \times 0.04$	$0.3 \times 0.04 \times 0.02$
colour	green	brown	brown
Temperature (K)	223.00(10)	223.00(10)	223.00(10)
μ (mm ⁻¹)	1.073	1.072	1.069
Unique data, parameters,	14317, 491,	7777, 527,	7300, 562,
restraints	0	105	18
R_1 ^(a)	0.0500	0.0669	0.0489
wR_2 ^(b)	0.1253	0.1738	0.1404

GOF ^(c)	0.905	1.103	1.036
Residual Fourier (e. Å ⁻³)	-0.352; 0.775	-0.855; +0.807	-0.864; +0.478

$$^a R_1 = \Sigma ||F_o| - |F_c|| / \Sigma |F_o|;$$

$$^b wR_2 = \{ \Sigma [w(F_o^2 - F_c^2)^2] / \Sigma [w(F_o^2)^2] \}^{1/2};$$

$$^c \text{GOF} = \{ \Sigma [w(F_o^2 - F_c^2)^2] / (n - p) \}^{1/2}, \text{ where } n \text{ is the number of reflections and } p \text{ the total number of parameters refined.}$$

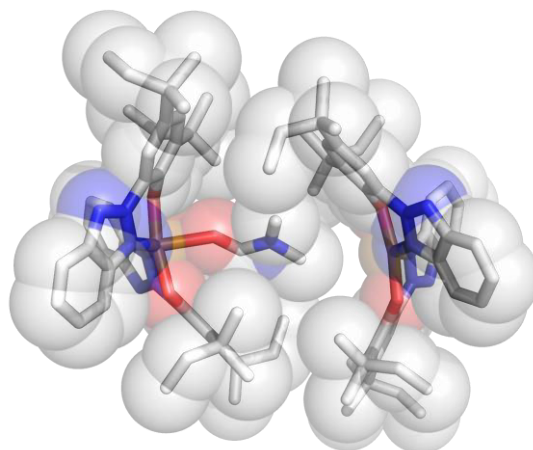


Figure 46. Space-filling structure of the complex $[\text{CuL}_2(\text{DMF})_{0.5}] [\text{Cu}(\text{L}^2)_2\text{DMF}]$ showing the interaction of two $[\text{Cu}(\text{L}^2)_2]$ moieties that exhibit a cavity where DMF binds.

Table 13. Selected bond lengths [Å] and angles [°] for $[\text{Cu}(\text{L}^2)_2]$, $[\text{Cu}(\text{L}^2)_2\text{DMF}]$ and $[\text{Cu}(\text{L}^2)_2\text{DMA}]$.

	$[\text{CuL}_2]$	$[\text{CuL}_2(\text{DMF})_{0.5}]$	$[\text{CuL}_2(\text{DMA})_{0.5}]$
Cu1–O1	1.873(2)	1.885(2)	1.8906(18)
Cu1–O2	1.8694(19)	1.892(2)	1.8904(18)
Cu1–O3		2.245(9)	2.255(4)
Cu1–N1	1.989(2)	2.009(2)	2.013(2)
Cu1–N4	1.985(2)	2.027(2)	2.024(2)
O1–Cu1–O2	161.24(10)	169.54(11)	169.85(9)
O1–Cu1–O3		84.7(2)	87.07(13)
O1–Cu1–N1	92.21(9)	90.55(9)	90.39(8)
O1–Cu1–N4	94.78(9)	92.89(9)	92.94(8)
O2–Cu1–O3		84.9(2)	83.19(13)
O2–Cu1–N1	92.99(9)	92.76(9)	92.90(8)
O2–Cu1–N4	91.49(9)	90.82(9)	90.70(8)
N1–Cu1–O3		116.3(4)	125.20(16)

N1–Cu1–N4	144.22(10)	140.76(10)	139.98(9)
N4–Cu1–O3		102.9(4)	94.80(16)
Σ_{Cu}^a	371.50(9)	367.05(9)	366.96(5)
Benzotriazole1– benzotriazole2	98.16	102.44	102.74

$$^a \Sigma_{\text{Cu}} = (\text{O1–Cu1–N1}) + (\text{N1–Cu1–O2}) + (\text{O2–Cu1–N4}) + (\text{N4–Cu1–O1}).$$

From molecular structures of the compound $[\text{Cu}(\text{L}^2)_2]$ could be seen the $\pi - \pi$ stacking intramolecular interaction due to the parallel displacement of the benzotriazolyl moieties of the ligand. In the case of $[\text{Cu}(\text{L}^2)_2\text{DMF}]$ and $[\text{Cu}(\text{L}^2)_2\text{DMA}]$ the benzotriazolyl moieties are not in a parallel displacement and the angle of them is 4.15° and 5.25° respectively.

To get insight into the geometric and electronic features of $[\text{Cu}(\text{L}^2)_2]$ theoretical calculations based on Density Functional Theory (DFT) were undertaken.

Table 14. Selected bond lengths [\AA] and angles [$^\circ$] for experimental and theoretical data obtained for $[\text{Cu}(\text{L}^2)_2]$.

Complex	$[\text{Cu}(\text{L}^2)_2]$	
	X-ray	DFT
Cu1–O1	1.873(2)	1.900
Cu1–O2	1.8694(19)	1.903
Cu1–N1	1.989(2)	1.995
Cu1–N4	1.985(2)	1.998
O1–Cu1–O2	161.24(10)	160.32
O1–Cu1–N1	92.21(9)	90.05
O1–Cu1–N4	94.78(9)	95.08
O2–Cu1–N1	92.99(9)	95.91
O2–Cu1–N4	91.49(9)	89.68
N1–Cu1–N4	144.22(10)	148.25

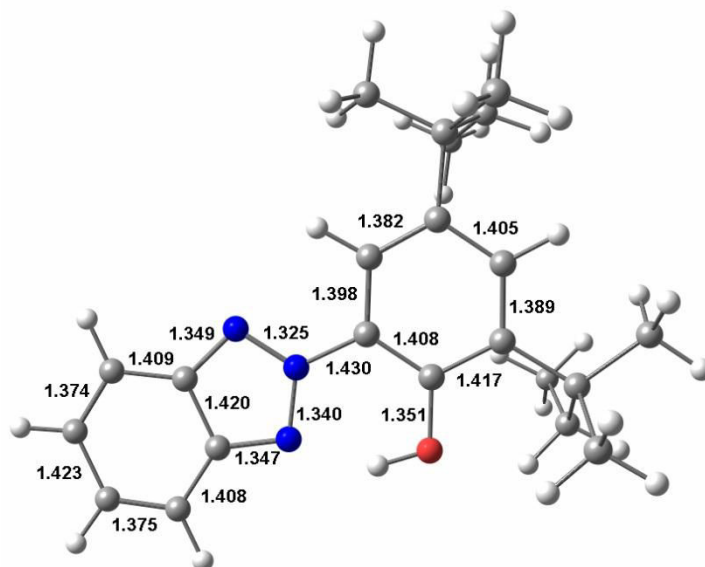


Figure 47. DFT-optimized structure of HL^2 and selected metrical parameters.

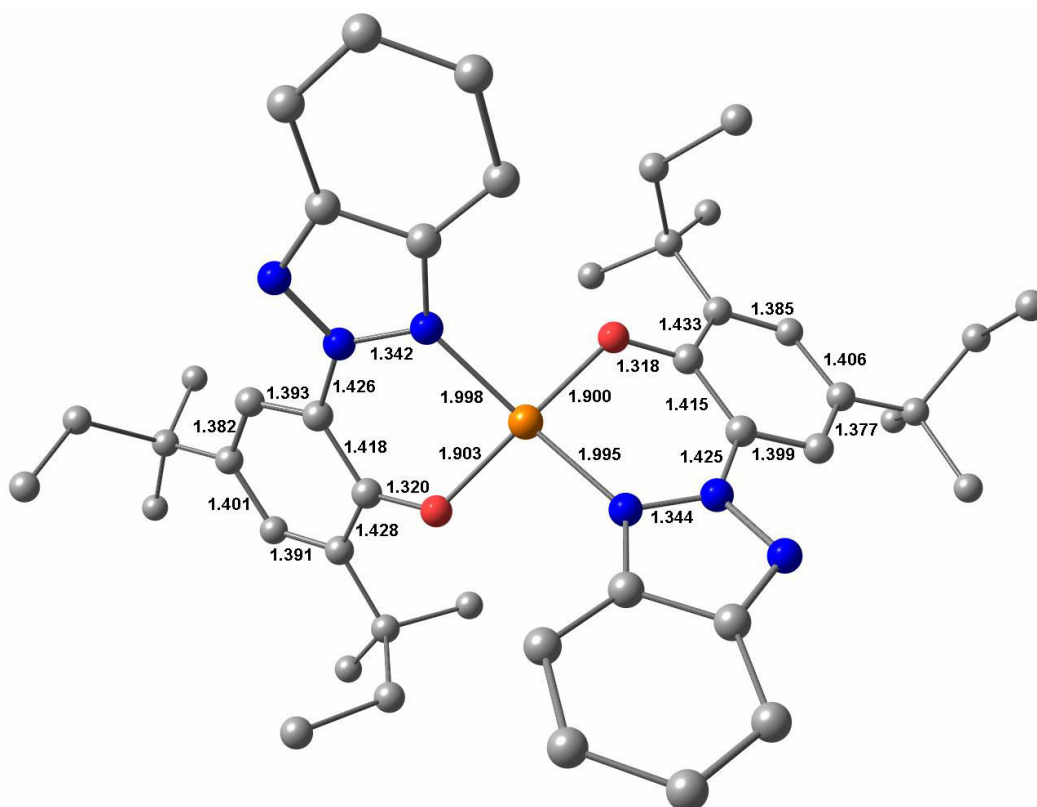


Figure 48. DFT-optimized structure of $[\text{Cu}(\text{L}^2)_2]$ (hydrogen atoms were omitted for clarity).

The structure of the ligand (HL^2) and the complex $[\text{Cu}(\text{L}^2)_2]$ were first subjected to geometry optimization (Table 14 and Figures 47 and 48). Comparison of the DFT-optimized structure of $[\text{Cu}(\text{L}^2)_2]$ with the X-ray data showed a good agreement between the two sets

of data which confirmed that $[\text{Cu}(\text{L}^2)_2]$ can be best described as a pseudo-square planar Cu(II) complex ($[\text{CuL}_2]^0$, $S = \frac{1}{2}$). Electronic structure calculations further support this assignment as the spin density plot of $[\text{Cu}(\text{L}^2)_2]$ shows that positive spin populations are found both at the Cu center (56%) and at its coordinating O- and N-atoms (32%, Figure 49).

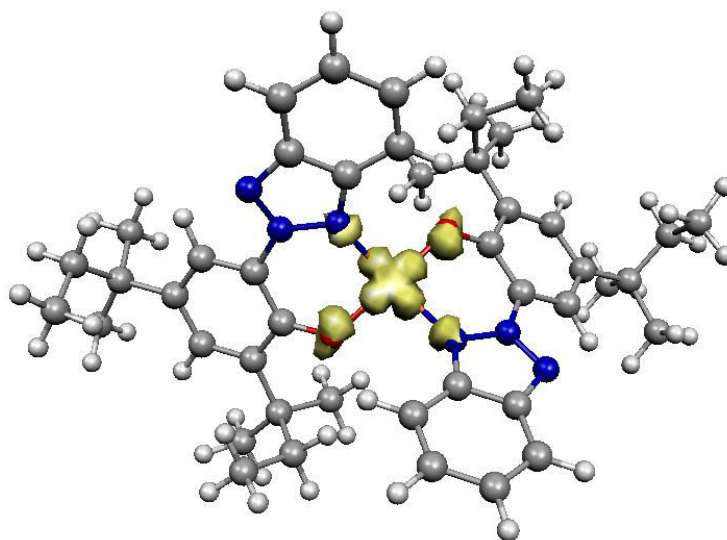


Figure 49. Spin density plot of $[\text{Cu}(\text{L}^2)_2]$.

Consistently the singly occupied molecular orbital (SOMO) of $[\text{Cu}(\text{L}^2)_2]$ presents a dominant Cu $3d_{x^2-y^2}$ character and is mainly distributed over the metal and its first coordination sphere (Figure 50) which shows us a metal-based character and a covalency of the metal-ligand bonds.

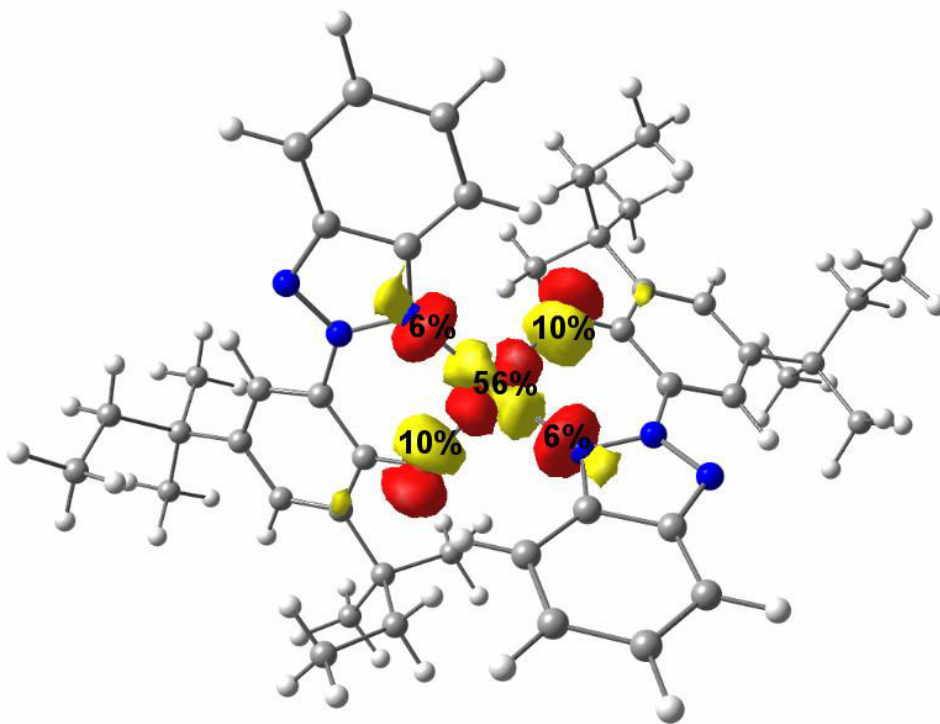


Figure 50. DFT-calculated redox active orbital for complex $[\text{Cu}(\text{L}^2)_2]$.

2.4. IR study

The IR study for obtained copper benzotriazolphenolate coordination compounds ($[\text{Cu}(\text{L}^2)_2]$, $[\text{Cu}(\text{L}^2)_2\text{DMF}]$, $[\text{Cu}(\text{L}^2)_2\text{DMA}]$ and $[\text{Cu}(\text{L}^2)_2\text{DMSO}]$) consist of numerous absorption bands. The presence of *N,N*-dimethylformamide in compound $[\text{Cu}(\text{L}^2)_2\text{DMF}]$ and *N,N*-dimethylacetamide in compound $[\text{Cu}(\text{L}^2)_2\text{DMA}]$ is proved by the bands at 1665.0 cm^{-1} for $[\text{Cu}(\text{L}^2)_2\text{DMF}]$ and at 1634.6 cm^{-1} for $[\text{Cu}(\text{L}^2)_2\text{DMA}]$, assigned to the carbonyl group coordinated to the metal. The carbonyl group in noncoordinated *N,N*-dimethylformamide and *N,N*-dimethylacetamide is positioned at 1687 cm^{-1} and 1662 cm^{-1} respectively. These bands are shifted to the lower values by $22, 28\text{ cm}^{-1}$ respectively which suggests the coordination of the solvent molecule to the metal through the carbonyl group.

The most part of the bands in the region $650 - 4000\text{ cm}^{-1}$ of the IR spectra of coordination compounds $[\text{Cu}(\text{L}^2)_2]$, $[\text{Cu}(\text{L}^2)_2\text{DMF}]$, $[\text{Cu}(\text{L}^2)_2\text{DMA}]$ and $[\text{Cu}(\text{L}^2)_2\text{DMSO}]$ are characteristic to the vibrations of the HL^2 ligand bonds. The majority of them are listed in the table presented below.

Table 15. IR data of the complexes $[\text{Cu}(\text{L}^2)_2]$, $[\text{Cu}(\text{L}^2)_2\text{DMF}]$, $[\text{Cu}(\text{L}^2)_2\text{DMA}]$ and $[\text{Cu}(\text{L}^2)_2\text{DMSO}]$ (cm^{-1}) and their assignment

	$[\text{Cu}(\text{L}^2)_2]$	$[\text{Cu}(\text{L}^2)_2\text{DMF}]$	$[\text{Cu}(\text{L}^2)_2\text{DMA}]$	$[\text{Cu}(\text{L}^2)_2\text{DMSO}]$
(CH) stretch	2955,8	2960,6	2960,1	2960,1
$\nu_{\text{as}}(\text{CH}_3)$	2910,2	2902,2	2911,1	2910,7
$\nu_{\text{s}}(\text{CH}_3)$	2872		2874,6	2873
$\nu(\text{C}=\text{C})$	1606,3; 1576,7; 1556	1605,9; 1571,5; 1556	1571,0; 1555,8	1603,7; 1574,7; 1553,9
(CH) bend	1466,9	1466,9	1467,8	1470,4
$\nu(\text{C}=\text{N})$	1404,8	1404,3	1403,4	1403,9
$\nu(\text{C}-\text{C})$	1310,6	1305,7	1305,7	1309,4
$\nu_{\text{as}}(\text{Ph}-\text{O})$	1254,1	1255	1254,6	1256,5
$\nu_{\text{s}}(\text{Ph}-\text{O})$	1223,2	1224,1	1223,6	1223,4
$\beta(\text{C}-\text{H})$	1115	1113,9	1114,1	1113,6
δ	988,1; 830,9	982	981,5; 828,8	989,1; 829,7
$\gamma(\text{C}-\text{H})$	766,9; 742,9	768,8; 744,9	768,8; 745,1	767,8; 750,8

The remaining bands in the limits $1400\text{-}650\text{ cm}^{-1}$ may be assigned to fingerprint region of these complexes. The bands characteristic to the metal – ligand bond usually could be observed in the range above 650 cm^{-1} .

2.5. UV-vis and EPR characterization of copper complexes

The room temperature electronic absorption spectrum of the ligand HL^2 and the complex $[\text{Cu}(\text{L}^2)_2]$ in DMF are shown in Figure 51. The spectrum for HL^2 reveals the presence of two bands at 305 nm ($\epsilon = 26 \times 10^3\text{ L mol}^{-1}\text{ cm}^{-1}$) and 340 nm ($\epsilon = 25 \times 10^3\text{ L mol}^{-1}\text{ cm}^{-1}$).

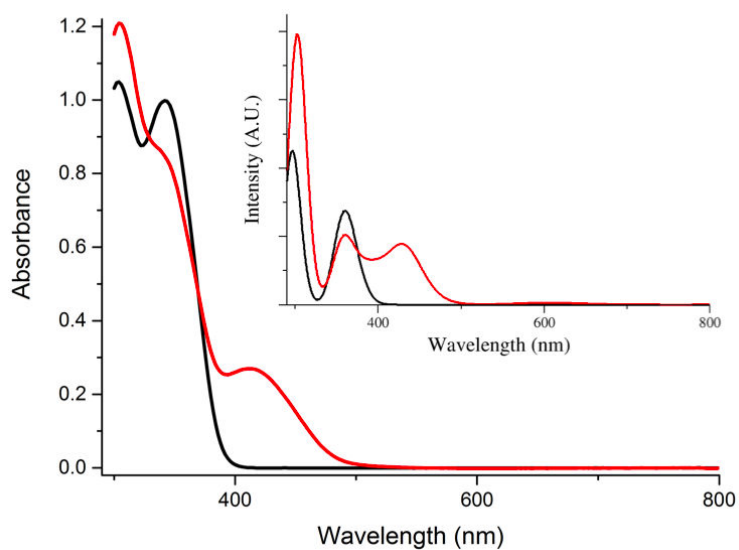


Figure 51. Electronic absorption spectra of 3.98×10^{-5} M solution of ligand (HL^2) (black line) and of 3.32×10^{-5} M solution of complex $[\text{Cu}(\text{L}^2)_2]$ (red line) in DMF. Inset: TDDFT-predicted UV-vis spectra of (HL^2) (black line), and $[\text{Cu}(\text{L}^2)_2]$ (red line).

The electronic spectrum of $[\text{Cu}(\text{L}^2)_2]$ in DMF exhibits two main absorption bands at 305 nm ($\epsilon=35 \times 10^3 \text{ L mol}^{-1} \text{ cm}^{-1}$) and 410 nm ($\epsilon=13 \times 10^3 \text{ L mol}^{-1} \text{ cm}^{-1}$), and a shoulder at 340 nm. The UV-Vis spectra of complexes $[\text{Cu}(\text{L}^2)_2]$, $[\text{Cu}(\text{L}^2)_2\text{DMF}]$, $[\text{Cu}(\text{L}^2)_2\text{DMA}]$ and $[\text{Cu}(\text{L}^2)_2\text{DMSO}]$ in DMF being pretty similar (Figure 52 and Table 16), and the results obtained on complex $[\text{Cu}(\text{L}^2)_2]$ will be discussed in details.

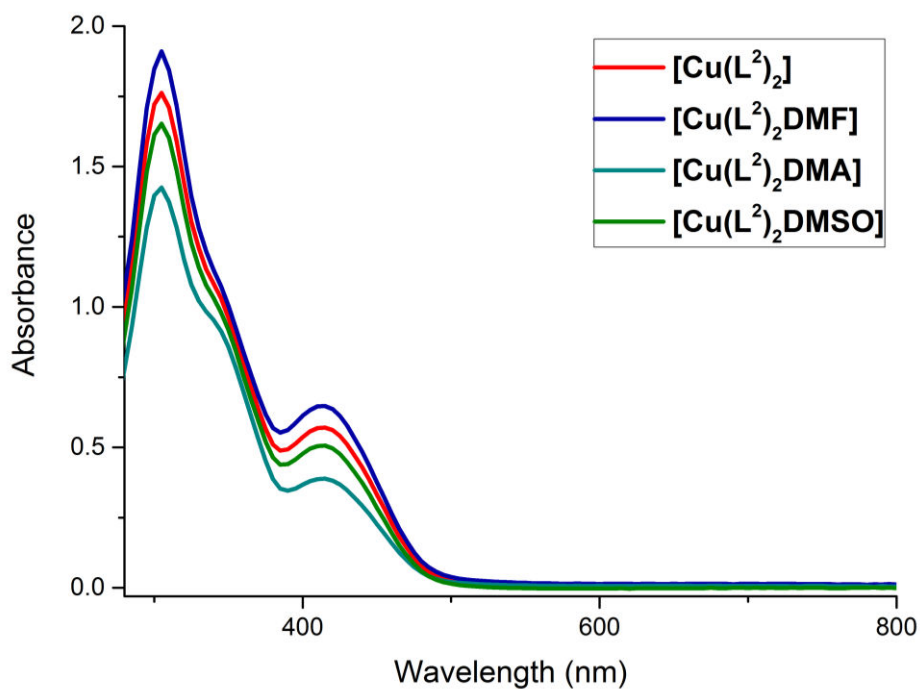


Figure 52. Electronic absorption spectra of 4.98×10^{-5} M solutions of complexes $[\text{Cu}(\text{L}^2)_2]$, $[\text{Cu}(\text{L}^2)_2\text{DMF}]$, $[\text{Cu}(\text{L}^2)_2\text{DMA}]$ and $[\text{Cu}(\text{L}^2)_2\text{DMSO}]$ in DMF.

Table 16. UV-Visible absorption parameters for HL^2 and complexes $[\text{Cu}(\text{L}^2)_2]$, $[\text{Cu}(\text{L}^2)_2\text{DMF}]$, $[\text{Cu}(\text{L}^2)_2\text{DMA}]$ and $[\text{Cu}(\text{L}^2)_2\text{DMSO}]$ in DMF.

Compound	Band, nm	Band, nm	Band, nm
	(ϵ , $10^3 \text{ M}^{-1} \text{ cm}^{-1}$)	(ϵ , $10^3 \text{ M}^{-1} \text{ cm}^{-1}$)	(ϵ , $10^3 \text{ M}^{-1} \text{ cm}^{-1}$)
HL	305 (26)	340 (25)	
1	305 (35)	340 (sh)	410 (13)
2	305 (37)	340 (sh)	410 (13)
3	305 (29)	340 (sh)	410 (12)
4	305 (32)	340 (sh)	410 (13)

From Figure 53 can be observed that the nature of the solvent does not influence the electronic spectra of the complex $[\text{Cu}(\text{L}^2)_2]$.

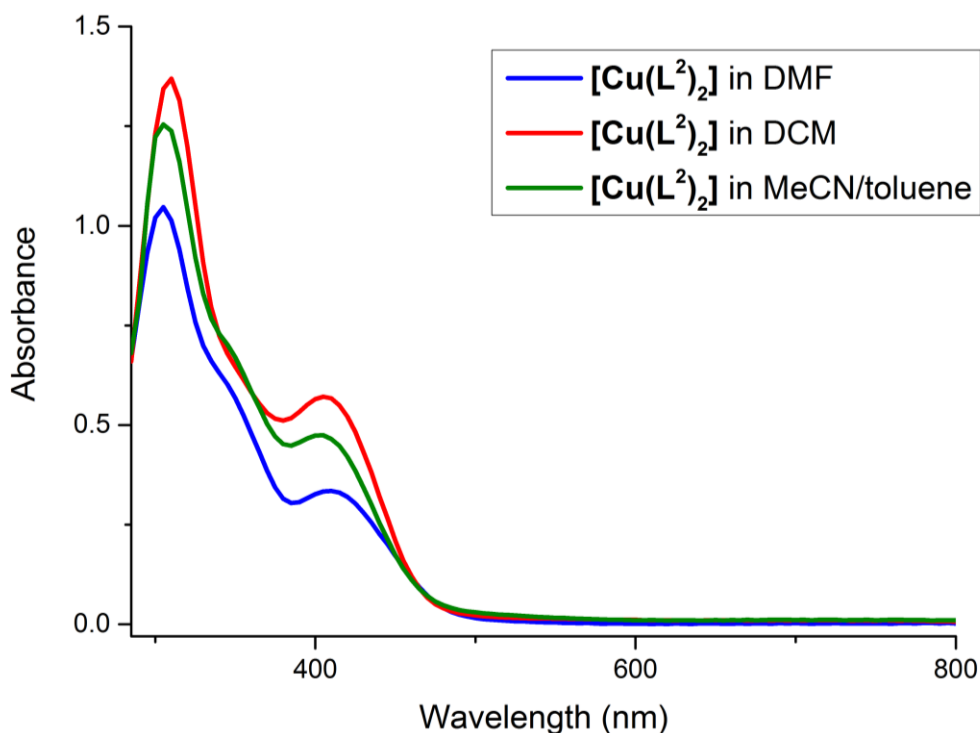
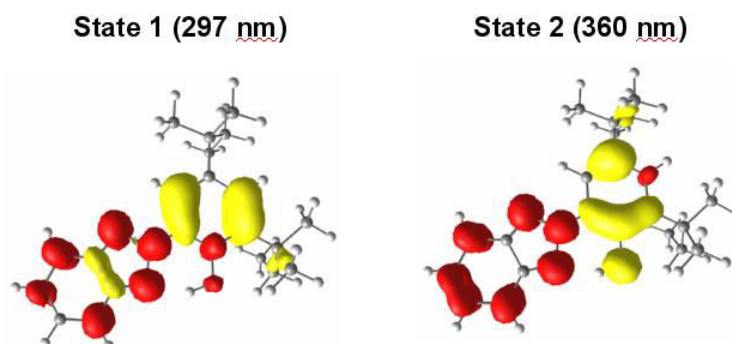


Figure 53. Electronic absorption spectra for $[\text{Cu}(\text{L}^2)_2]$ in DMF, DCM, MeCN/toluene 5:3 at the concentration $2.96 \times 10^{-5} \text{M}$.

For a better understanding of the optical properties of (HL^2) and $[\text{Cu}(\text{L}^2)_2]$, TDDFT calculations were carried out on their optimized structures. By employing this computational method, we can provide the assignment of their salient features by calculating the main transition energies and their relative intensities (Figure 51, inset). The calculations adequately reproduce the key features of both spectra in terms of energy and intensity, namely, the two bands at 305 and 340 nm (calc: $\lambda(f) = 297(0.495)$ and 360(0.317) nm) for (HL^2) and the two bands at 305 and 410 nm as well as the shoulder at 340 nm (calc: $\lambda(f) = 303(0.575)$, 360(0.239) and 428(0.168) nm) for $[\text{Cu}(\text{L}^2)_2]$ (Figure 51, inset and Table 17). Regarding the nature of these absorptions, they all present a $\pi\text{-}\pi^*$ character in (HL^2) (Figure 54) while for $[\text{Cu}(\text{L}^2)_2]$ the low-energy absorption can be assigned to a metal-metal transition and the two other absorptions are consistent with ligand-to-ligand charge transfer transitions (Figure 55).

Table 17. TDDFT-calculated electronic transitions for HL^2 , $[\text{Cu}(\text{L}^2)_2]$ and $[\text{Cu}(\text{L}^2)_2]^+$.

Complex	λ^{calc} (nm)	f^{calc}	TDDFT assignment
HL^2	297	0.495	Ligand \rightarrow Ligand
	360	0.317	Ligand \rightarrow Ligand
$[\text{Cu}(\text{L}^2)_2]$	303	0.575	Ligand \rightarrow Ligand
	360	0.239	Ligand \rightarrow Ligand
	428	0.168	Metal \rightarrow Metal
$[\text{Cu}(\text{L}^2)_2]^+$	306	0.264	Ligand \rightarrow Ligand
	370	0.254	Ligand \rightarrow Metal
	424	0.123	Ligand \rightarrow Ligand

**Figure 54.** Difference electron density sketch for relevant transitions of HL^2 (yellow = negative, red = positive density).

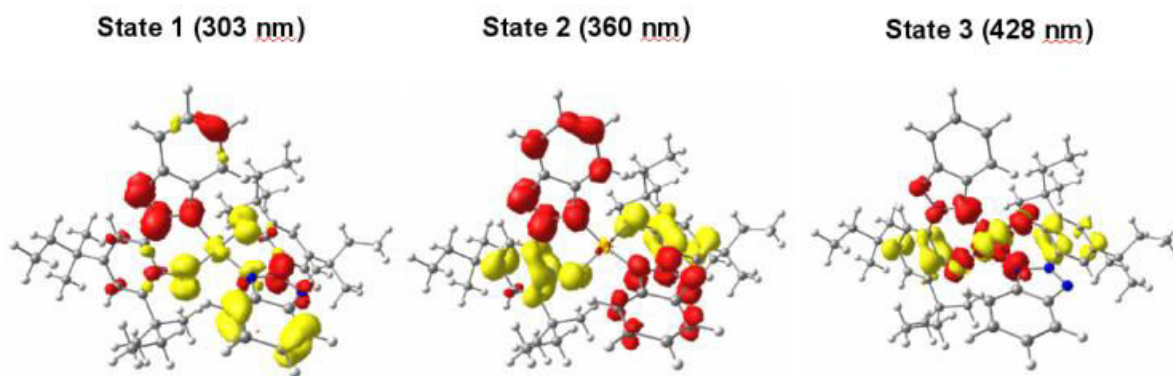


Figure 55. Difference electron density sketch for relevant transitions in complex $[\text{Cu}(\text{L}^2)_2]$ (yellow = negative, red = positive density).

From the DFT predicted UV-visible spectra (Figure 51) we can see that the theoretical data are in a good accordance with the experimental spectra. As we can see in Figure 55 and Table 17, first transition is correlated to a ligand charge transfer, the second to the ligand to metal charge transfer process and the third to a intra ligand through the metal charge transfer.

The X-band EPR spectrum of $[\text{Cu}(\text{L}^2)_2]$ was recorded on a frozen CH_2Cl_2 sample at 120 K. EPR parameters were simulated using Easyspin program package and the corresponding simulated spectrum is shown in Figure 56 together with experimental data. The spectrum exhibits the four expected lines at low field, due to the hyperfine interaction between the unpaired electron of the complex and the copper nucleus. Simulation of the spectrum using a single paramagnetic species lead to three different principal g values with $g_1 = 2.053$, $g_2 = 2.063$, $g_3 = 2.280$ and $g_3 > g_1 \sim g_2$. The g values are characteristic for a mononuclear Cu(II) complex having an unpaired electron occupying the $3d_{x^2-y^2}$ orbital,⁶²⁻⁶⁴ which is consistent with the DFT findings regarding the electronic ground state of $[\text{Cu}(\text{L}^2)_2]$ (Figure 50) and the computed EPR parameters (Table 18).

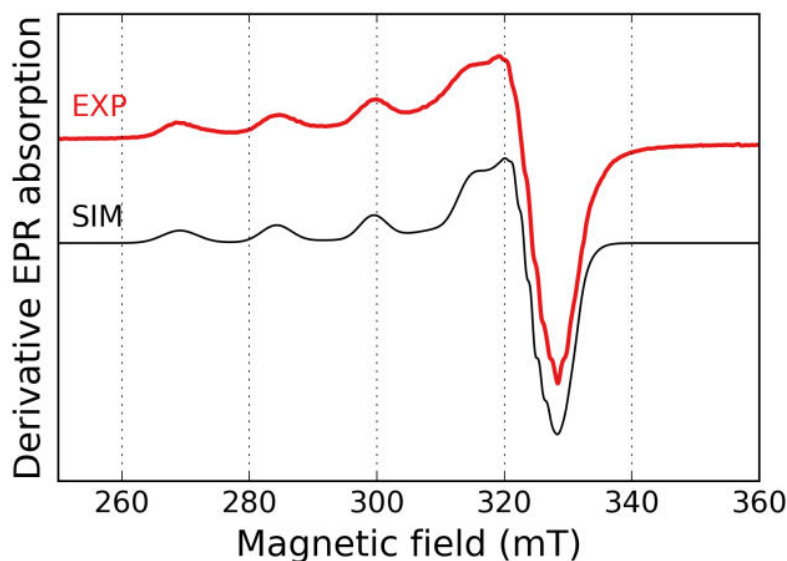


Figure 56. Simulated (black line) and experimental (red line) *cw* X-band EPR spectrum of 1mM solution of $[\text{Cu}(\text{L}^2)_2]$ in CH_2Cl_2 at $T= 120\text{K}$.

Table 18. Comparison of the EPR parameters for $[\text{Cu}(\text{L}^2)_2]$ obtained from simulation of the experimental spectrum and derived from DFT calculations.

	g-tensor			^{63}Cu hfc (MHz)			^{14}N hfc (MHz)		
	g_1	g_2	g_3	A_1	A_2	A_3	A'_1	A'_2	A'_3
Exp.	2.053	2.030	2.280	10	10	475	37	37	37
Calc.	2.033	2.067	2.178	35	35	455	35	36	44

The hyperfine coupling constants (hfc) of $[\text{Cu}(\text{L}^2)_2]$ were also simulated: $A_1 = A_2 = 10$, $A_3 = 475$ MHz for ^{63}Cu hfc and $A'_1 = A'_2 = A'_3 = 37$ MHz for ^{14}N hfc. The g_3 and A_3 values lie in the range of values reported for a copper center coordinated by a mixture of N and O ligands in the equatorial plan.^{65,66} Consistently with the simulated spectra, the calculations also predict an axial sets of hyperfine parameters for the ^{14}N center and a large A_3 component for ^{63}Cu nucleus. The fair agreement between the computed EPR parameters and the experimental data thus support the DFT-calculated structure for complex $[\text{Cu}(\text{L}^2)_2]$.

2.6. Electrochemical characterization

The redox behavior of (**HL**²) ligand (Figure 9) and [**Cu(L**²)₂] were studied by cyclic voltammetry (CV) in DMF with 0.1 M TBAPF₆. All potentials are referenced versus the Fc⁺/Fc redox couple. The complex is electro-active in the potential range from -1.5 to +1.2 V (Figure 57, Table 19). The CV curves of [**Cu(L**²)₂] display one quasi reversible one-electron redox wave at $E_{1/2}^0 = -1.03$ V in the cathodic region of potentials attributed to the Cu(II)/Cu(I) redox couple. In the anodic region of potentials, complex [**Cu(L**²)₂] exhibits three irreversible oxidation waves at $E_p^{a,1} = 0.52$ V, $E_p^{a,2} = 0.69$ V and $E_p^{a,3} = 0.96$ V. The last two oxidation peaks are associated to two reduction peaks at $E_p^{c,1} = -0.20$ V and $E_p^{c,2} = -0.50$ V.

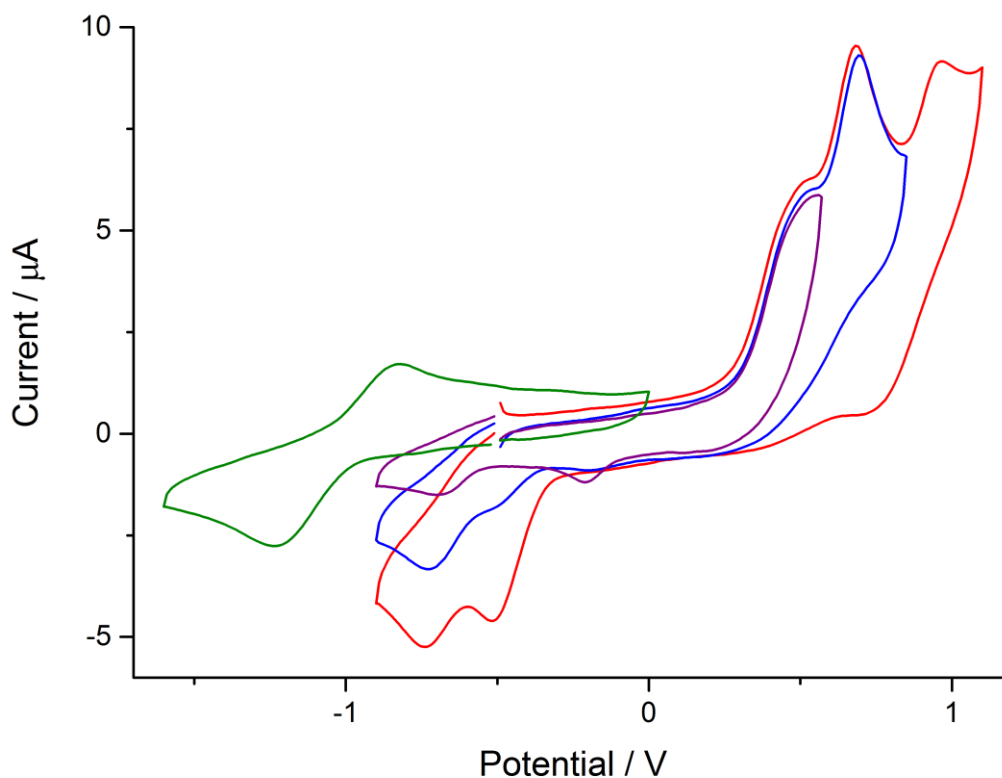


Figure 57. Cyclic voltammogram of 1 mM solution of (1) in DMF containing 0.1 M TBA.PF₆. The potentials are referenced versus Fc⁺/Fc redox couple. CV were recorded in both oxidation mode (red, blue and purple lines) and reduction mode (green line).

Table 19. CV data for $[\text{Cu}(\text{L}^2)_2]$ recorded in DMF.

complex	$E_p^{a,0}$	$E_p^{c,0}$	$E_{1/2}^0$	$E_p^{a,1}$	$E_p^{c,1}$	$E_p^{a,2}$	$E_p^{c,2}$	$E_p^{a,3}$	$E_p^{c,3}$
$[\text{Cu}(\text{L}^2)_2]$	-1,23	-0,83	-1,03	0,52	-0,20	0,69	-0,50	0,96	0,70

2.7. One-electron oxidized species generation and characterization

Chemical oxidation of complex $[\text{Cu}(\text{L}^2)_2]$ was performed by adding a one-electron oxidant, NOSbF_6 , to the medium (1 eq. in dichloromethane at -40°C). The resulting species, supposedly mono-oxidized, was then characterized by spectroscopic methods including EPR and UV-vis techniques. Upon chemical oxidation we observe that the intensity of the EPR signal corresponding to the initial complex $[\text{Cu}(\text{L}^2)_2]$ clearly decreases (Figure 58).

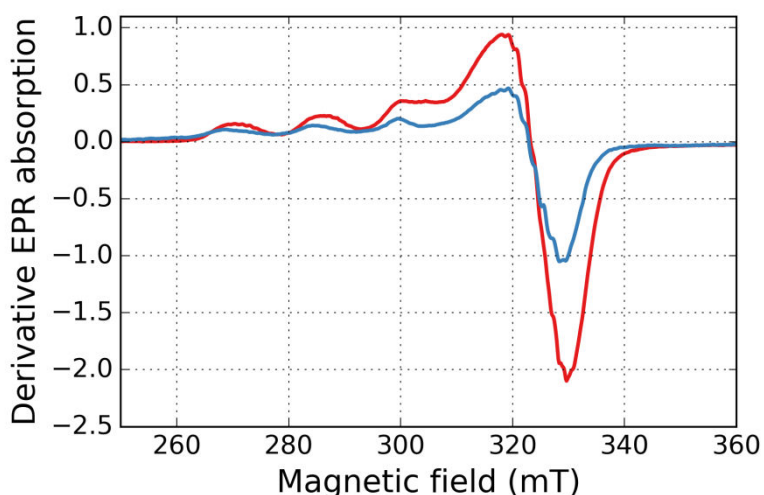


Figure 58. Experimental *cw* X-band EPR spectra of 1 mM solution of $[\text{Cu}(\text{L}^2)_2]$ (red line) and its chemically mono-oxidized species $[\text{Cu}(\text{L}^2)_2]^+$ (blue line) in CH_2Cl_2 at $T=120\text{ K}$.

The intensity ratio of the two signals is directly proportional to the quantity of spins in the sample, $\text{Cu}(\text{II})$, $S=1/2$ in this case. By double integration of the recorded signals one obtains: $I([\text{Cu}(\text{L}^2)_2]^+)/I([\text{Cu}(\text{L}^2)_2])=N(\text{Cu}(\text{II}), \text{blue line})/N(\text{Cu}(\text{II}), \text{red line}) = 0.55$. This is indicative of the clear disappearance of $[\text{Cu}(\text{L}^2)_2]$ consistently with the formation of an EPR-silent species $[\text{Cu}(\text{L}^2)_2]^+$ like a metal-radical complex.

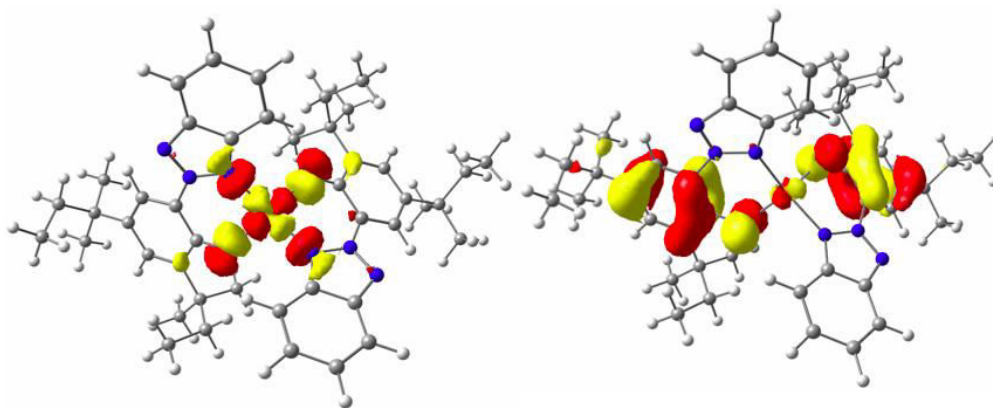


Figure 59. DFT-calculated redox active orbitals for the one-electron oxidized complex $[\text{Cu}(\text{L}^2)_2]^+$.

Such an assignment is supported by DFT calculations conducted on the mono-oxidized species $[\text{Cu}(\text{L}^2)_2]^+$. Geometry optimization (Figure 60) and electronic structure calculations (Figures 59 and 61) confirm that the oxidation of $[\text{Cu}(\text{L}^2)_2]$ is a ligand-based process leading to the formation of a radical ligand coupled to a Cu(II) center as the first SOMO of $[\text{Cu}(\text{L}^2)_2]^+$ presents a dominant metal character while the second SOMO is a delocalized π orbital essentially distributed over the ligand framework. Due to the orthogonality of the two SOMOs and an energy gap of $6.5 \text{ kcal mol}^{-1}$ with respect to the singlet state, the ground spin state of this species can be assigned as a triplet $S=1$. Such a spin state is also consistent with the EPR measurements (Figure 58).

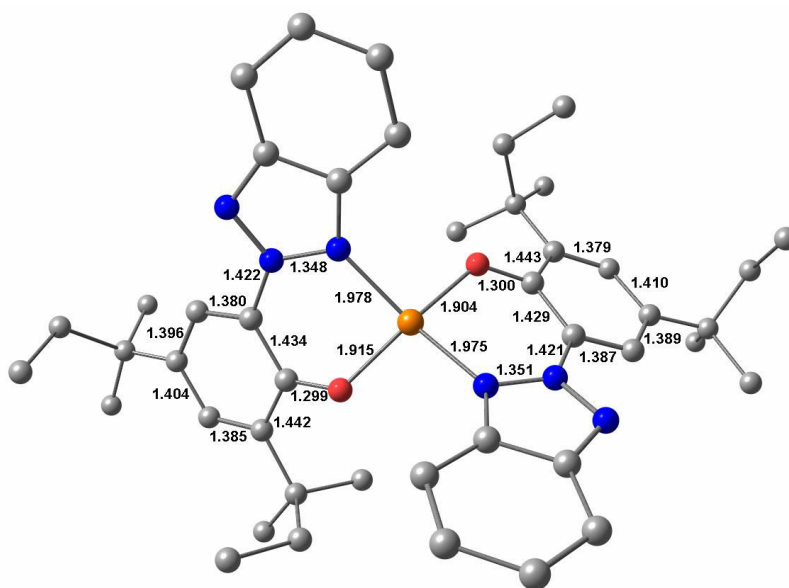


Figure 60. DFT-optimized structure of $[\text{Cu}(\text{L}^2)_2]^+$ (hydrogen atoms were omitted for clarity).

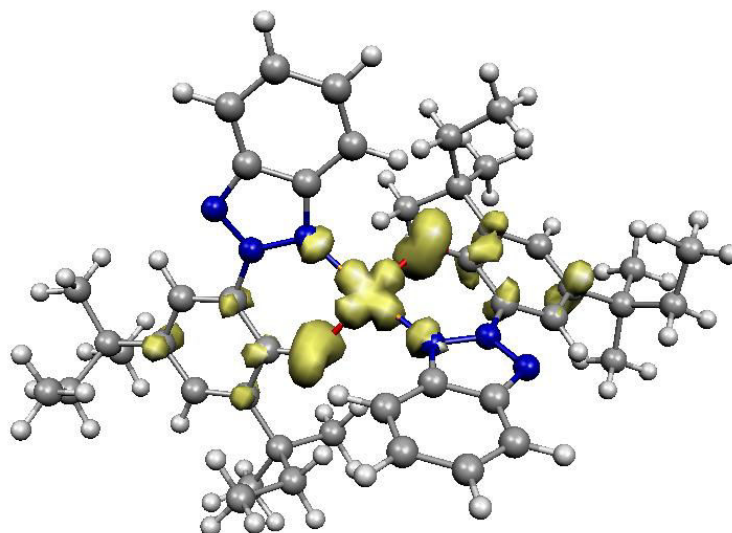


Figure 61. Spin density plot of $[\text{Cu}(\text{L}^2)_2]^+$.

The chemical oxidation of $[\text{Cu}(\text{L}^2)_2]$ also causes a net decrease of the intensity of the 305 and 410 nm bands while the intensity of the transition at 340 nm increases (Figure 62).

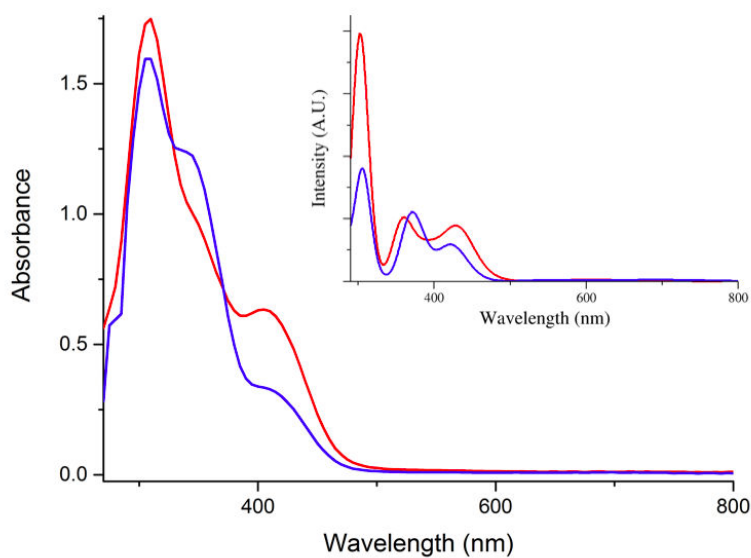


Figure 62. UV-visible spectra of 4.76×10^{-5} M solutions of $[\text{Cu}(\text{L}^2)_2]$ (red line) and its chemically mono-oxidized species $[\text{Cu}(\text{L}^2)_2]^+$ (blue line) in CH_2Cl_2 at $T = 298$ K. Inset: TDDFT-predicted UV-vis spectra of $[\text{Cu}(\text{L}^2)_2]$ (red line) and $[\text{Cu}(\text{L}^2)_2]^+$ (blue line).

TDDFT calculations performed on the geometry-optimized structure of $[\text{Cu}(\text{L}^2)_2]^+$ fairly reproduce the UV-vis spectral evolution in terms of energy and intensity

(Figure 62, inset). The two bands at 305 and 410 nm are predicted at 306 and 424 nm ($f = 0.264$ and 0.123 , respectively) while the one at 340 nm is predicted at 370 nm ($f = 0.254$) (Table 17). Regarding the nature of these absorptions, the low-energy absorption can be assigned to an intra-ligand charge transfer as expected for a metal-radical species while the two other absorptions are consistent with metal-to-ligand and ligand-to-ligand transitions (Figure 63).

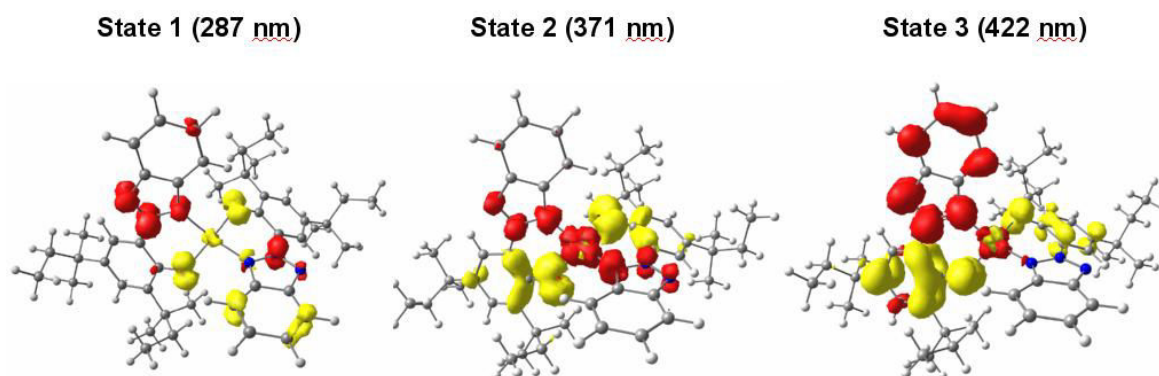


Figure 63. Difference electron density sketch for relevant transitions of $[\text{Cu}(\text{L}^2)]^+$ (yellow = negative, red = positive density).

The stability of the phenoxyl radical was investigated using the UV-vis spectroscopic technique (Figure 64). Our results show that the spectrum obtained for $[\text{Cu}(\text{L}^2)]^+$ evolves rapidly in time since the main feature found at 410 nm and characteristic for the metal-radical species totally disappears after 15 min. Indeed, the resulting spectrum looks very similar to the one obtained the ligand alone which indicates a poor stability for the species formed upon one-electron oxidation of $[\text{Cu}(\text{L}^2)]$.

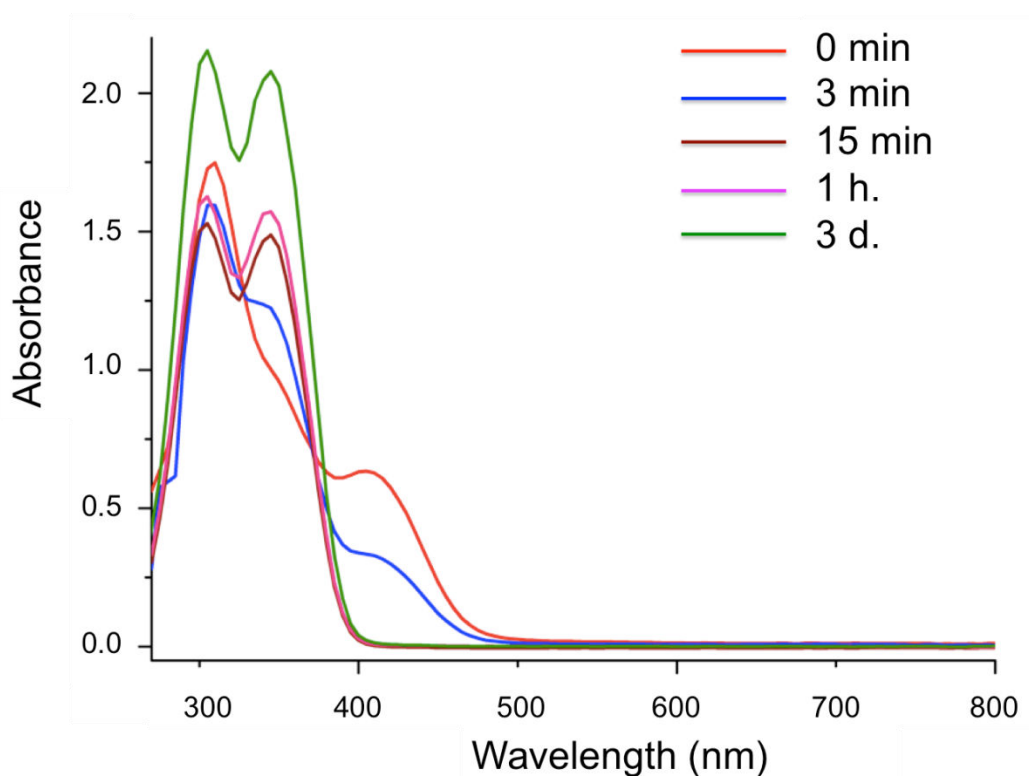


Figure 64. Time evolution of the UV-visible spectra of 4.76×10^{-5} M solutions of $[\text{Cu}(\text{L}^2)_2]$ (red line) and its chemically mono-oxidized species $[\text{Cu}(\text{L}^2)_2]^+$ (blue line) in CH_2Cl_2 at $T = 298$ K.

2.8. Veratryl alcohol oxidation

Under aerobic conditions, copper(I)/(II) complexes derived from triazole-phenolate ligands have been described as catalyst for the oxidation of benzyl alcohol into benzaldehyde.⁵⁸ In order to study the reactivity of our copper(II) complex $[\text{Cu}(\text{L}^2)_2]$, we checked its capability for veratryl alcohol oxidation (Figure 65). In DMF and under aerobic condition, complex $[\text{Cu}(\text{L}^2)_2]$ does not exhibit any reactivity towards veratryl alcohol. However, in the presence of H_2O_2 in DMF, complex $[\text{Cu}(\text{L}^2)_2]$ leads to the formation of veratryl aldehyde in 2.5% conversion (based on the alcohol concentration) and a turnover number (TON) of 5 mol of product per mol of catalyst upon 30 minutes of reaction. Control reactions carried out either in the absence of the metal complex, hydrogen peroxide or alcohol alone indicate that no appreciable alcohol oxidation reaction occurs (conversion $< 0.05\%$) (Figure 67). Similarly alcohol oxidation assays carried out in the same conditions using a copper(II) sulfate salt in the presence or absence of hydrogen peroxide did not lead to any noticeable reaction conversion (0.12% and 0.07%, respectively).

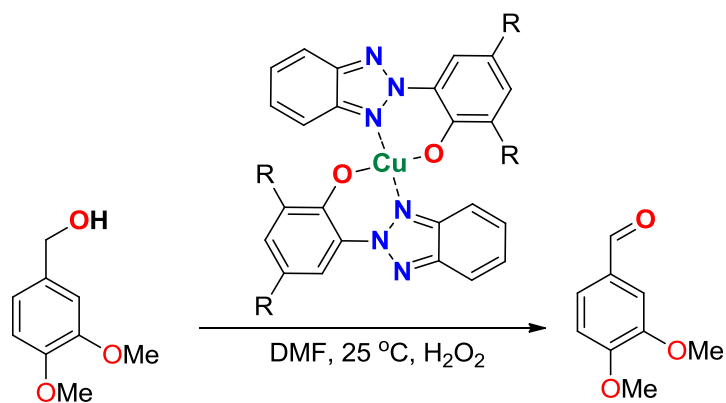


Figure 65. Oxidation of veratryl alcohol by $[\text{Cu}(\text{L}^2)_2]$ in DMF. R= *tert*-pentyl.

To get insight into the copper species responsible for the oxidation of veratryl alcohol, UV-vis. spectroscopy was employed to follow the reactivity of copper complex $[\text{Cu}(\text{L}^2)_2]$ with increased amounts of hydrogen peroxide. As observed with NOSbF_6 , addition of H_2O_2 causes the decrease of the intensity of the bands at 410 nm and 305 nm while the intensity of the one at 340 nm increases (Figure 66). This clearly indicates that H_2O_2 -mediated oxidation produces the same species than the one obtained by a mono-oxidation with NOSbF_6 which was attributed to the one-electron oxidized copper complex $[\text{Cu}(\text{L}^2)_2]^+$.

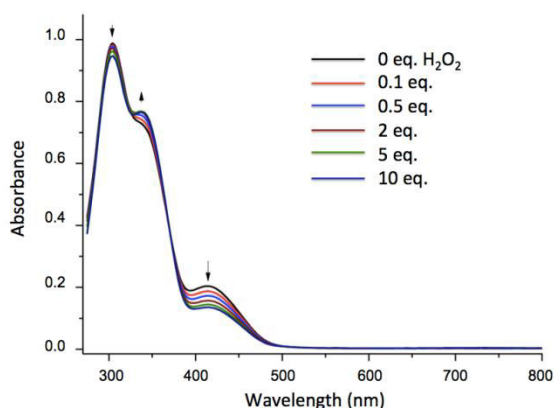


Figure 66. Electronic absorption spectra of 3.21×10^{-5} M solution of complex $[\text{Cu}(\text{L}^2)_2]$ in DMF with increasing amounts of hydrogen peroxide. T= 298 K.

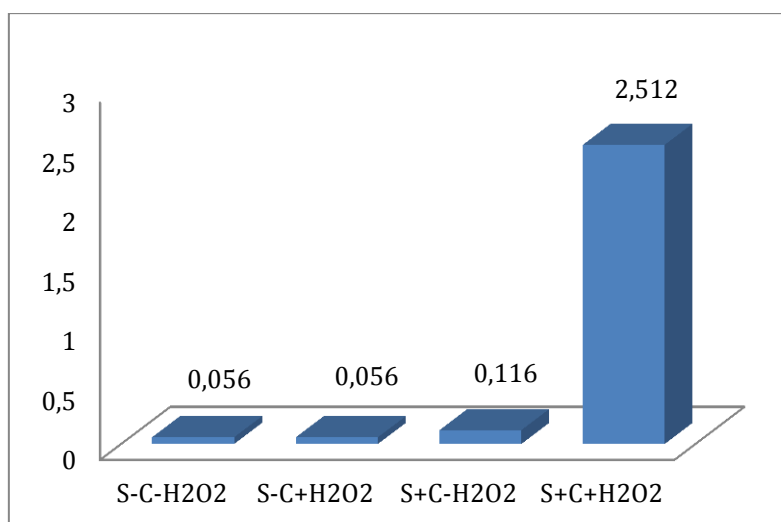


Figure 67. Aerobic oxidation of veratryl alcohol (S) at 25 °C in DMF in presence (+) and without (-) hydrogen peroxide (H₂O₂), in presence/absence (+/-) of complex [Cu(L²)₂] (C). The data represent the conversion at 30 minutes.

2.9. DNA cleavage

Copper(II) complexes are known to cleave efficiently DNA in oxidative conditions.⁵⁷ Therefore we checked the capability of copper complex [Cu(L²)₂] in the oxidative digestion of DNA. The nuclease activity of the copper(II) complex [Cu(L²)₂] was studied on supercoiled pUC19 DNA at 37°C for 1 hour with hydrogen peroxide (H₂O₂, 100 μM). The corresponding gel electrophoresis is presented in Figure 68 and relevant numerical data are reported in Table 20.

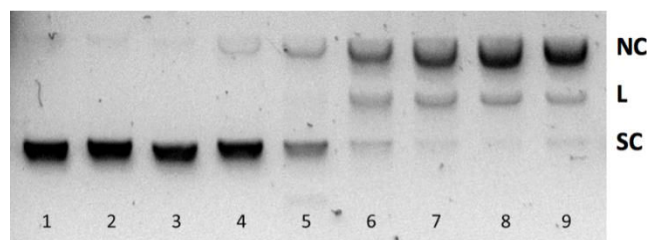


Figure 68. Agarose gel electrophoresis diagram showing the cleavage of SC pUC19 DNA (0.1 μg) by various concentrations of complex [Cu(L²)₂] in DMSO (5% from total volume) treated with H₂O₂ in TE buffer (10 mM Tris-HCl, pH = 8.0; 0.1 mM EDTA) in dark. Incubation time: 1 h (37 °C). Lane 1: DNA control; lane 2: DNA +DMSO (5%); lane 3: DNA + H₂O₂ (100 μM); lane 4: DNA + [Cu(L²)₂] (500 μM in 1 μL DMSO); lane 5: DNA + H₂O₂ (100 μM) + [Cu(L²)₂] (100 μM in 1 μL DMSO); lane 6: DNA + H₂O₂ (100 μM) + [Cu(L²)₂] (200 μM in 1 μL DMSO); lane 7: DNA + H₂O₂ (100 μM) + [Cu(L²)₂] (300 μM in 1 μL DMSO); lane 8: DNA + H₂O₂ (100 μM) + [Cu(L²)₂] (400 μM in 1 μL DMSO); lane 9: DNA + H₂O₂ (100 μM) + [Cu(L²)₂] (500 μM in 1 μL DMSO).

As shown in Figure 68, complex $[\text{Cu}(\text{L}^2)_2]$ exhibits significant DNA cleavage reactivity in the 100-500 μM concentration range. The amount of DNA breaks (NC) increases as a function of the concentration of complex $[\text{Cu}(\text{L}^2)_2]$ as evidenced by the progressive transformation of supercoiled plasmid (SC) to the nicked circular form (NC) and then to the linear form (L). Blank experiments with DNA alone (lanes 1), DNA containing 5% DMSO (lane 2) and DNA with 100 μM H_2O_2 (lane 3) showed no nuclease activity (Figure 68).

Table 20. Copper complex $[\text{Cu}(\text{L}^2)_2]$ mediated DNA cleavage.

Entries	$[\text{Cu}(\text{L}^2)_2]$ μM	H_2O_2 (100 μM)			Ascorbate (100 μM)			DTT (100 μM)		
		SC	NC	L	SC	NC	L	SC	NC	L
		1	0	100	-	-	100	-	-	100
2	100	48	52	-	-	72	18	71	29	-
3	200	-	59	41	-	48	52	3	72	25
4	300	-	72	28	-	80	20	1	68	33
5	400	-	80	20	-	68	32	-	75	25
6	500	-	84	16	-	89	11	-	80	20

We also checked the reactivity of complex $[\text{Cu}(\text{L}^2)_2]$ in the presence of a reducing agent (ascorbate or dithiothreitol, DTT) under aerobic conditions. As shown in Figures 69 and 70, both nuclease activities are comparable to the one with H_2O_2 . In both cases, the amount of NC also increases as a function of the concentration of complex $[\text{Cu}(\text{L}^2)_2]$ (Tables 21 and 22).

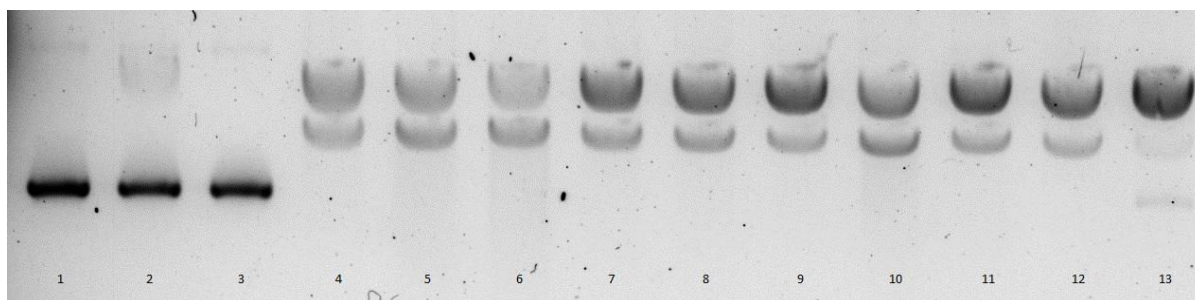


Figure 69. Copper complex $[\text{Cu}(\text{L}^2)_2]$ mediated DNA cleavage in the presence of ascorbate. Agarose gel electrophoresis diagram showing the cleavage of SC pUC19 DNA (0.1 μg) by various concentrations of complex $[\text{Cu}(\text{L}^2)_2]$ in DMF (5% from total volume) treated with ascorbate in TE buffer (10 mM Tris-HCl, pH = 8.0; 0.1 mM EDTA) in dark. Incubation time: 1 h (37 $^\circ\text{C}$). Lane 1: DNA + ascorbate + DMF (5%); lane 2: DNA + $[\text{Cu}(\text{L}^2)_2]$ (500 μM in 1 μL DMF); lane 3: DNA + ascorbate (100 μM) + $[\text{Cu}(\text{L}^2)_2]$ (50 μM in 1 μL DMF); lane 4: DNA + ascorbate (100 μM) + $[\text{Cu}(\text{L}^2)_2]$ (100 μM in 1 μL DMF); lane 5: DNA + ascorbate (100 μM) + $[\text{Cu}(\text{L}^2)_2]$ (150 μM in 1 μL DMF); lane 6: DNA + ascorbate (100 μM) + $[\text{Cu}(\text{L}^2)_2]$ (200 μM in 1 μL DMF); lane 7: DNA + ascorbate (100 μM) + $[\text{Cu}(\text{L}^2)_2]$ (250 μM in 1 μL DMF); lane 8: DNA + ascorbate (100 μM) + $[\text{Cu}(\text{L}^2)_2]$ (300 μM in 1 μL DMF); lane 9: DNA + ascorbate (100 μM) + $[\text{Cu}(\text{L}^2)_2]$ (350 μM in 1 μL DMF); lane 10: DNA + ascorbate (100 μM) + $[\text{Cu}(\text{L}^2)_2]$ (400 μM in 1 μL DMF); lane 11: DNA + ascorbate (100 μM) + $[\text{Cu}(\text{L}^2)_2]$ (450 μM in 1 μL DMF); lane 12: DNA + ascorbate (100 μM) + $[\text{Cu}(\text{L}^2)_2]$ (500 μM in 1 μL DMF).

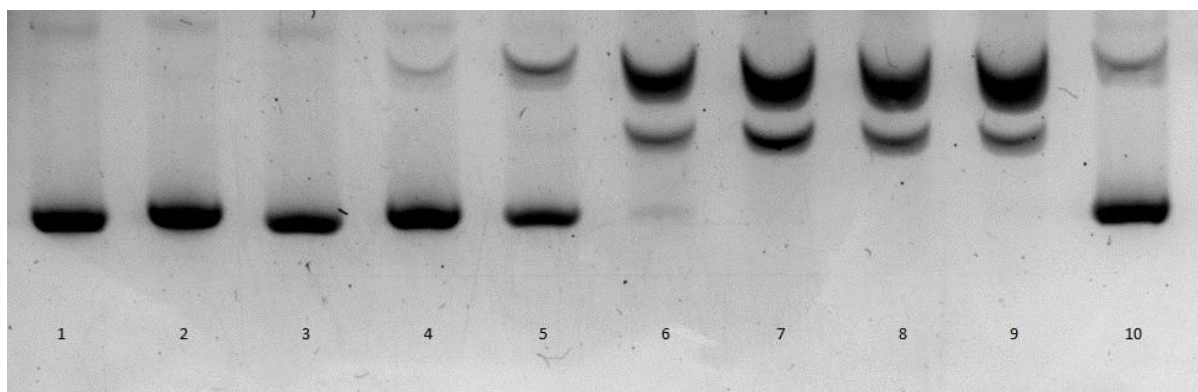


Figure 70. Copper complex $[\text{Cu}(\text{L}^2)_2]$ mediated DNA cleavage in the presence of DTT. Agarose gel electrophoresis diagram showing the cleavage of SC pUC19 DNA (0.1 μg) by various concentrations of complex $[\text{Cu}(\text{L}^2)_2]$ in DMSO (5% from total volume) treated with DTT in TE buffer (10 mM Tris-HCl, pH = 8.0; 0.1 mM EDTA) in dark. Incubation time: 1 h (37 $^\circ\text{C}$). Lane 1: DNA control; lane 2: DNA +DMSO (5%); lane 3: DNA + DTT (100 μM); lane 4: DNA + $[\text{Cu}(\text{L}^2)_2]$ (500 μM in 1 μL DMSO); lane 5: DNA + DTT (100 μM) + $[\text{Cu}(\text{L}^2)_2]$ (100 μM in 1 μL DMSO); lane 6: DNA + DTT (100 μM) + $[\text{Cu}(\text{L}^2)_2]$ (200 μM in 1 μL DMSO); lane 7: DNA + DTT (100 μM) + $[\text{Cu}(\text{L}^2)_2]$ (300 μM in 1 μL DMSO); lane 8: DNA + DTT (100 μM) + $[\text{Cu}(\text{L}^2)_2]$ (400 μM in 1 μL DMSO); lane 9: DNA + DTT (100 μM) + $[\text{Cu}(\text{L}^2)_2]$ (500 μM in 1 μL DMSO); lane 10: DNA + DTT (100 μM) + CuCl_2 (30 μM).

Table 21. DNA cleavage data of SC pUC19 (0.1 μg) DNA by $[\text{Cu}(\text{L}^2)_2]$ in DMF (5% from total volume) on chemical oxidation by ascorbate (100 μM). Incubation time 1 h in dark.

Lanes	Reaction conditions	$[\text{Cu}(\text{L}^2)_2]$ (μM)	% SC	% NC	% L
1	DNA + ascorbate + DMF	-	100	-	-
2	DNA + $[\text{Cu}(\text{L}^2)_2]$	500	98	2	-
4	DNA + ascorbate + $[\text{Cu}(\text{L}^2)_2]$	100	1	72	17
5	DNA + ascorbate + $[\text{Cu}(\text{L}^2)_2]$	150	-	61	39

6	DNA + ascorbate + $[\text{Cu}(\text{L}^2)_2]$	200	-	48	52
8	DNA + ascorbate + $[\text{Cu}(\text{L}^2)_2]$	300	-	80	20
10	DNA + ascorbate + $[\text{Cu}(\text{L}^2)_2]$	400	-	68	32
12	DNA + ascorbate + $[\text{Cu}(\text{L}^2)_2]$	500	-	89	11
13	DNA + ascorbate + CuCl_2	-/100	96	4	-

Table 22. DNA cleavage data of SC pUC19 (0.1 μg) DNA by $[\text{Cu}(\text{L}^2)_2]$ in DMSO (5% from total volume) on chemical oxidation by DTT (100 μM). Incubation time 1 h in dark.

Lanes	Reaction conditions	$[\text{Cu}(\text{L}^2)_2]$ (μM)	% SC	% NC	% L
2	DNA + DMSO	-	96	4	-
3	DNA + DTT	-	95	5	-
4	DNA + $[\text{Cu}(\text{L}^2)_2]$	500	90	10	-
5	DNA + DTT + $[\text{Cu}(\text{L}^2)_2]$	100	71	29	-
6	DNA + DTT + $[\text{Cu}(\text{L}^2)_2]$	200	3	72	25
7	DNA + DTT + $[\text{Cu}(\text{L}^2)_2]$	300	-	67	33
8	DNA + DTT + $[\text{Cu}(\text{L}^2)_2]$	400	-	75	25
9	DNA + DTT + $[\text{Cu}(\text{L}^2)_2]$	500	-	80	20
10	DNA + DTT + CuCl_2	-/30	79	21	-

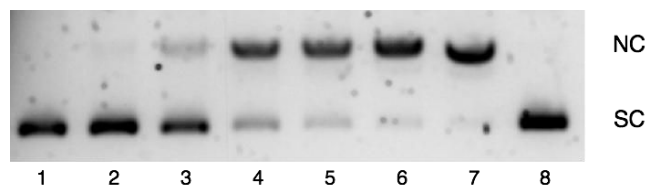


Figure 71. Agarose gel electrophoresis diagram showing the cleavage of SC pUC19 DNA (0.1 μg) by various concentrations (0-150 μM) of complex $[\text{Cu}(\text{L}^2)_2]$ in DMSO (5% from total volume) treated with H_2O_2 in TE buffer (10 mM Tris-HCl, pH = 8.0; 0.1 mM EDTA) in dark. Incubation time: 1 h (37 $^\circ\text{C}$). Lane 1: DNA + DMSO (5%) + H_2O_2 (100 μM); lane 2: DNA + H_2O_2 (100 μM) + $[\text{Cu}(\text{L}^2)_2]$ (25 μM in 1 μL DMSO); lane 3: DNA + H_2O_2 (100 μM) + $[\text{Cu}(\text{L}^2)_2]$ (50 μM in 1 μL DMSO); lane 4: DNA + H_2O_2 (100 μM) + $[\text{Cu}(\text{L}^2)_2]$ (75 μM in 1 μL DMSO); lane 5: DNA + H_2O_2 (100 μM) + $[\text{Cu}(\text{L}^2)_2]$ (100 μM in 1 μL DMSO); lane 6: DNA + H_2O_2 (100 μM) + $[\text{Cu}(\text{L}^2)_2]$ (125 μM in 1 μL DMSO); lane 7: DNA + H_2O_2 (100 μM) + $[\text{Cu}(\text{L}^2)_2]$ (150 μM in 1 μL DMSO); lane 8: DNA + H_2O_2 (100 μM) + CuCl_2 (50 μM).

It is difficult to characterize and compare the efficiency of metal complexes for DNA cleavage. Palandiavar *et al.* used a pseudo-Michaelis-Menten kinetic treatment to determine apparent V_{max} , K_{M} and k_{cat} .⁶⁷ We preferred to use a simpler treatment which consists in determining the complex concentration (AC_{50}) leading to 50% of the SC \rightarrow NC cleavage. In the set of experiments above described, we have used complex $[\text{Cu}(\text{L}^2)_2]$ in the concentration

range of 100-500 μM . These high concentration conditions lead to DNA degradation into small oligomers, which are difficult or even impossible to quantify by gel electrophoresis. In this context the activity of complex $[\text{Cu}(\text{L}^2)_2]$ was characterized by checking the conditions in which only the first cleavage occurs ($\text{SC} \rightarrow \text{NC}$). For that purpose, we have diminished the concentration of complex $[\text{Cu}(\text{L}^2)_2]$. We worked in the concentration range of 0-150 μM (Table 23 and Figure 71). In these conditions, we were able to determine an AC_{50} of 62 μM (Figure 72).

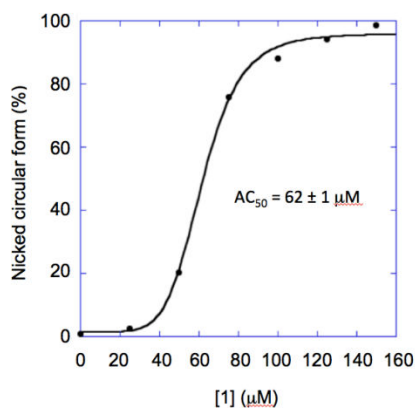


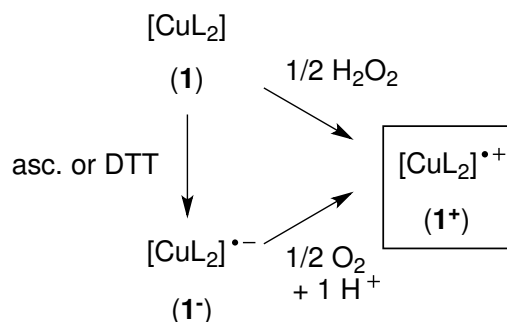
Figure 72. Mediated DNA cleavage by complex $[\text{Cu}(\text{L}^2)_2]$ min in the presence of H_2O_2 as oxidant.

Copper(II) complexes are known to cleave DNA through a hydrolytic process.⁶⁷ When DNA was incubated under anaerobic conditions with complex $[\text{Cu}(\text{L}^2)_2]$ alone (Table 23), less than 20% of the NC form were observed, while in the presence of 100 μM H_2O_2 and with the same concentration of complex $[\text{Cu}(\text{L}^2)_2]$ (150 μM) 98.5 % of NC forms are observed (Table 23, lane 7). These results confirm that the DNA cleavage occurs mainly through an oxidative process rather than a hydrolytic one.

Table 23. Copper complex $[\text{Cu}(\text{L}^2)_2]$ mediated DNA cleavage in the concentration range 0-150 μM .

Lanes	$[\text{Cu}(\text{L}^2)_2]$ μM	% NC with H_2O_2	% NC without H_2O_2
1	0	0.9	0.8
2	25	2.6	5.3
3	50 (CuCl_2)	20.2 (1.6)	7.8 (1.9)
4	75	75.9	9.7
5	100	88.0	26.5
6	125	94.3	16.3
7	150	98.5	18.0

It is widely accepted that copper salts can exhibit nuclease activities. In our conditions, copper chloride displayed a poor activity compared to complex $[\text{Cu}(\text{L}^2)_2]$. When DNA was incubated under anaerobic conditions with copper chloride alone (Table 23, lane 3), only 1.6 % of NC form was observed *versus* 20.2 % with complex $[\text{Cu}(\text{L}^2)_2]$.

**Figure 73.** Possible mechanism for oxidations promoted by complex $[\text{Cu}(\text{L}^2)_2]$ in the presence of H_2O_2 or reducing agents (ascorbate or DTT).

On the other hand, because complex $[\text{Cu}(\text{L}^2)_2]$ is insoluble in water, all the experiments were done in the presence of 5 % of DMSO to solubilize the copper complex $[\text{Cu}(\text{L}^2)_2]$. Since DMSO is known to be a HO^\bullet scavenger,⁶⁸ we can rule out its occurrence during the process. Consequently, we can assume that the oxidative species responsible for the DNA cleavage is

the one-electron oxidized species $[\text{Cu}(\text{L}^2)_2]^+$ as we have shown that this species can be obtained by reaction of complex $[\text{Cu}(\text{L}^2)_2]$ with H_2O_2 . In the presence of ascorbate or DTT, complex $[\text{Cu}(\text{L}^2)_2]$ can thus be reduced into complex $[\text{Cu}(\text{L}^2)_2]$ which is able to react with dioxygen to form the one-electron oxidized species $[\text{Cu}(\text{L}^2)_2]^+$ (Figure 73).

2.10. Conclusions to Chapter 2

In this chapter was presented the synthesis and comprehensive characterization for copper complexes containing 2-(2H-benzotriazol-2-yl)-4,6-ditert-pentylphenol ligand with general formula $[\text{Cu}(\text{L}^2)_2\text{X}]$ where X =none; DMF; DMA; DMSO respectively.

The complexes were isolated in different geometry: distorted tetrahedral and pentacoordinated complex. All complexes were synthesized via two distinct methods and isolated as monocrystalline products.

Complexes $[\text{Cu}(\text{L}^2)_2]$, $[\text{Cu}(\text{L}^2)_2\text{DMF}]$, $[\text{Cu}(\text{L}^2)_2\text{DMA}]$ were characterized by X-ray diffraction analysis and all the complexes $[\text{Cu}(\text{L}^2)_2]$, $[\text{Cu}(\text{L}^2)_2\text{DMF}]$, $[\text{Cu}(\text{L}^2)_2\text{DMA}]$ and $[\text{Cu}(\text{L}^2)_2\text{DMSO}]$ were characterized by different methods, such as IR, Elemental analysis, mass spectroscopy UV-vis, Electrochemistry, EPR and Theoretical calculations.

It was shown that the neutral copper(II) complex $[\text{Cu}(\text{L}^2)_2]$ exhibits an oxidative cleavage of DNA in the presence of different agents (H_2O_2 , Ascorbate, DTT) with an efficiency evaluated through its AC_{50} of 62 μM . Its oxidative activity towards DNA and veratryl alcohol was attributed to the mono-oxidized form $[\text{Cu}(\text{L}^2)_2]^+$, which has been generated by chemical oxidants such as NOSbF_6 and H_2O_2 and fully characterized by UV-vis., EPR and theoretical calculations. This study points out that copper complexes derived from benzotriazole-phenolate type ligand could be good candidates as anti-cancer agents if we solve the problem of their solubility in water. Further investigations will be needed to increase their solubility in water in order to envisage to check their effect on cancer cells.

CHAPTER 3

Palladium and copper phosphonates.

3.1. Introduction

In this chapter, we will describe the characterization of bisphosphonate and bisphosphonic acid metal complexes, followed by their use as catalysts in some specific reactions.

Phosphonates and phosphonic metals complexes have been described for several years, and their syntheses, structures and their potential applications have been reviewed.⁶⁹⁻⁷²

These complexes may find application in biomedical studies,^{73,74} and this can be related to the fact that some bisphosphonates may also act as ligands for metals, thus leading them to be employed in metal intoxication therapy.⁷⁵

Furthermore, the phosphonic acid moiety interacts easily with metallic surfaces such as titanium dioxide or iron oxide,⁷⁶ thus providing an efficient grafting of organic molecules on these surfaces, and the corresponding structures may lead to useful heterogeneous catalysts.⁷⁷

It was shown that aminophosphonate ligands easily lead to metal complexes which either possess biomedical potential⁷⁴ or show thermoluminescent properties.⁷⁸ On the other hand, the use of bisphosphonic esters as ligands for metals has been much less described.⁷⁹⁻⁸² However another interest raised by this kind of ligands is that the presence of the bisphosphonate function may influence the solubility of the corresponding complexes in water, thus allowing the possibility to use such compounds as catalysts in water mediated reactions.

Furthermore, the bisphosphonate can lead to bisphosphonic acid after hydrolysis, whose acids usually favors the grafting on metallic surfaces, as already pointed out.⁷⁶

Since these ligands modify the electronic density around the metal and therefore its reactivity, we turned out towards the synthesis of aminobisphosphonate ligands, namely pyridylbisphosphonates, with the aim of preparing palladium and copper complexes for catalytic studies, and/or for biochemical experiments.

3.2. *N*-(methylene-2-pyridine)-*N,N*-bis(diethoxyphosphorylmethyl)amine (**L**⁴)

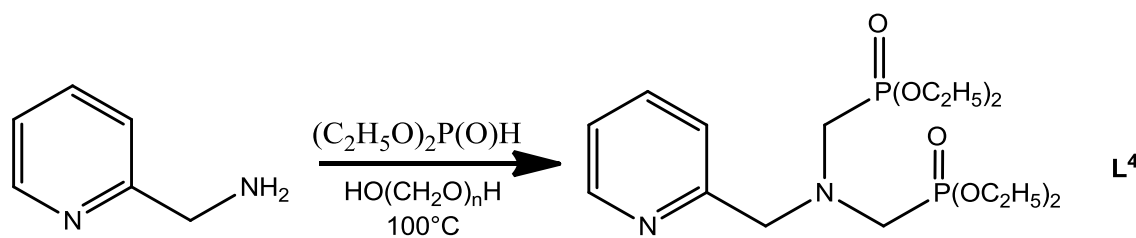


Figure 74. Illustration of *N*-(methylene-2-pyridine)-*N,N*-bis(diethoxyphosphorylmethyl)amine (**L**⁴) ligand.

This new compound was obtained through a double Kabachnik-Fields reaction, by adaptation of a known procedure,⁸³ starting from 2-aminomethyl pyridine (2-picolylamine) (Figure 74). This gave the compound as an orange oil in 89% yield after purification, which was fully characterized using the usual spectroscopic techniques.

³¹P NMR displays a single peak at 24.4 ppm, whereas ¹³C and ¹H spectra are in accordance with the structure.

High resolution mass spectroscopy shows a molecular peak at 408.1579 Da, which matches with the required mass.

UV visible spectra were recorded at different concentrations, to show invariably a characteristic band at 260nm (Figure 75).

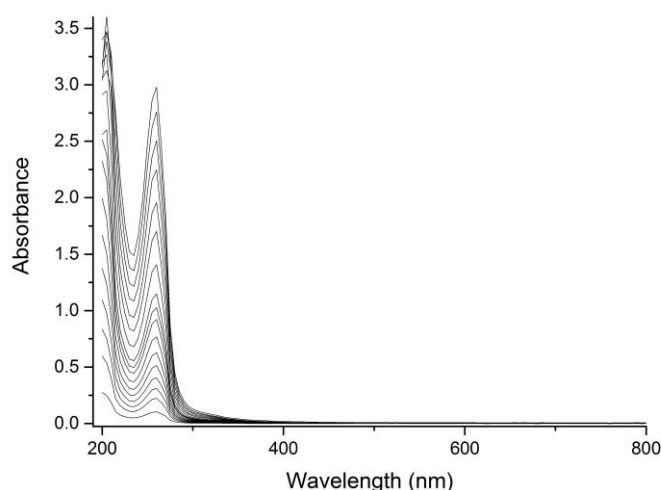


Figure 75. Electronic absorption spectra for **L**⁴ in CH₃CN at different concentrations (15 – 476 μM). Band at 260 nm.

3.3. Palladium (II) complex

3.3.1. Preparation of palladium(II) coordination compound

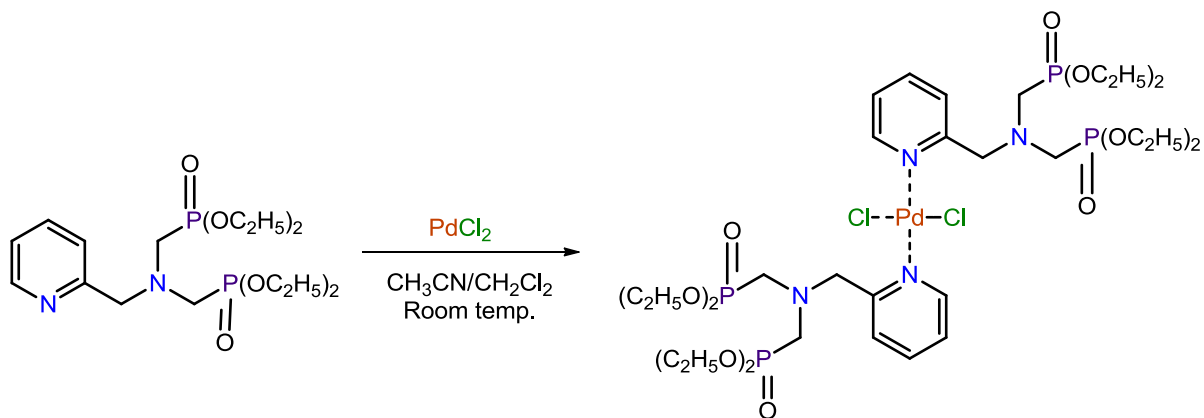


Figure 76. Scheme of the synthesis of the complex $[\text{Pd}(\text{L}^4)_2]$.

This complex (Figure 76) is easily formed by mixing and stirring a solution of palladium chloride in acetonitrile with a solution of ligand in dichloromethane, at room temperature. Crystals suitable for single X-ray diffraction analysis were grown from a DMSO solution (after one year, however).

3.3.2. Structural characterization of palladium(II) coordination compound

Compound $\text{Pd}(\text{L})_2\text{Cl}_2$ has a molecular structure in the crystal consisting of one neutral palladium(II) trans-dichloride containing unit, two ligand molecules, and two water molecules (Figure 77).

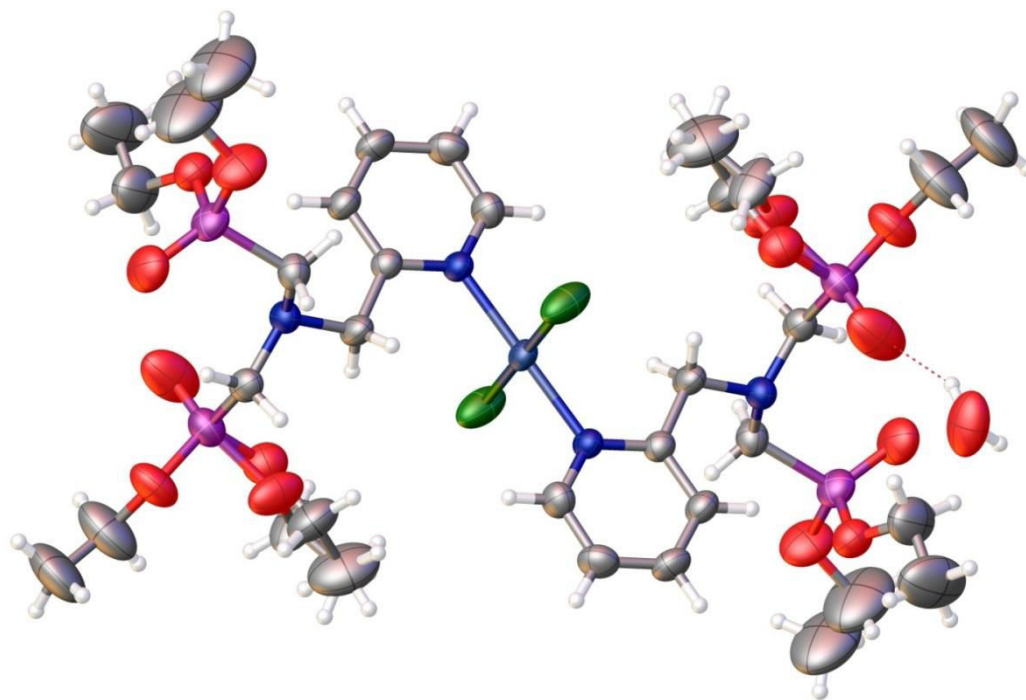


Figure 77. View of the molecule $[\text{Pd}(\text{L}^4)_2]$.

The compound crystallizes in the triclinic centrosymmetric space group P-1. The palladium has a square planar coordination sphere provided by two nitrogen and two chlorine atoms in a trans arrangement. The pyridinic rings are situated perpendicular to the plane formed by the central metal and its coordination sphere. The crystallographic data are shown below in Table 24.

Table 24. Crystallographic data for phosphonate-Pd complex $[\text{Pd}(\text{L}^4)_2]$.

Compound	$[\text{Pd}(\text{L}^4)_2]$
Empirical formula	$\text{C}_{32}\text{H}_{64}\text{Cl}_2\text{N}_4\text{O}_{14}\text{P}_4\text{Pd}$
Formula weight (g/mol)	1030.05
Crystal system	triclinic
Space group	P-1
<i>Unit cell dimensions</i>	
a (Å)	9.09726(18)
b (Å)	11.7041(3)
c (Å)	13.2219(3)
α (°)	109.521(2)
β (°)	104.3024(19)

γ ($^{\circ}$)	104.788(2)
Volume (\AA^3)	1194.60(5)
Z	1
λ (\AA)	0.71073
$\rho_{\text{calc.}}$ (g/cm^3)	1.432
Crystal size (mm^3), colour	$0.24 \times 0.12 \times 0.04$ brown needles
Temperature (K)	293
μ (mm^{-1})	0.695
Unique data, parameters, restraints	5792, 277, 2
R_1 ^(a)	0.0489
wR_2 ^(b)	0.1616
GOF ^(c)	1.263

Data collection method SuperNova, Dual, Cu at zero, AtlasS2

$$^a R_1 = \frac{\sum ||F_o| - |F_c||}{\sum |F_o|};$$

$$^b wR_2 = \left\{ \frac{\sum [w(F_o^2 - F_c^2)^2]}{\sum [w(F_o^2)^2]} \right\}^{1/2};$$

$$^c \text{GOF} = \left\{ \frac{\sum [w(F_o^2 - F_c^2)^2]}{(n - p)} \right\}^{1/2}, \text{ where } n \text{ is the number of reflections and } p \text{ the total number of parameters refined.}$$

These data reveal that palladium is coordinated only to the two nitrogen atoms from the two pyridine rings, and is not bound to the phosphonate moiety, it would be sterically impossible. This structure is in contrast with the complex described by Jordan⁸⁴ in which palladium is bound to the phosphine and to the oxygen atom of the phosphoryl bond (Figure 78).

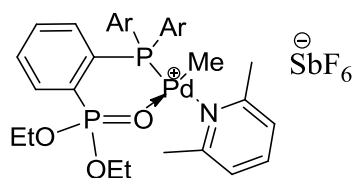


Figure 78. Palladium-phosphonate complex described by Jordan *et al.*⁸⁴

3.3.3. NMR study of L^4

The NMR spectra for this complex are quite similar to those of the free ligand. ^{31}P NMR displays a peak at 24.3 ppm.

In addition, the mass spectrum of this complex leads to the conclusion that a compound with a formula to $\text{C}_{32}\text{H}_{60}\text{O}_{12}\text{P}_4\text{PdCl}_2$ is present, corresponding to an exact mass of 994.1567 Da.

3.3.4. UV-vis

The UV-vis spectrum of $[\text{Pd}(L^4)_2]$ complex was recorded in acetonitrile and showed in Figure 79. The spectrum consists of 3 signals, two bands at 230 and 400 nm and a shoulder at 260 nm. This complex displays an additional band at 400 nm by comparison with L^4 , indicating a coordination of palladium to the ligand.

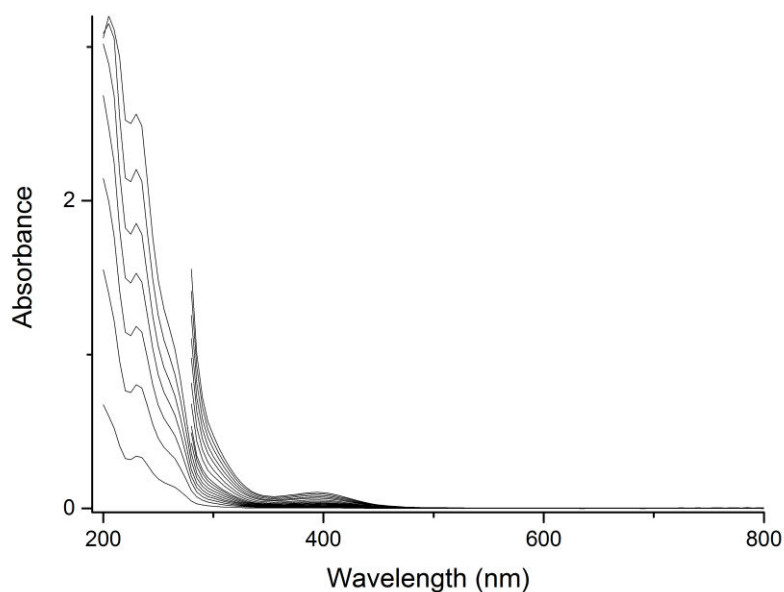


Figure 79. Electronic adsorption spectra for $[\text{Pd}(L^4)_2]$ in CH_3CN at different concentrations (15 – 476 μM). Band at 230 nm, shoulder at 260 nm. The band at 400 nm indicates that the palladium atom coordinates to the L^4 ligand.

3.4. Copper (II) compound

3.4.1. Preparation of copper(II) coordination compound

The synthesis of copper(II) coordination compounds with phosphonate groups containing pyridine-based ligands is still not described to be an easy and simple reaction. As a matter of fact the major difficulty is the high solubility of the complexes due to the presence of the phosphonate ester groups which is an impediment to the compounds isolation and crystallization.

We realized the synthesis of copper (II) complex $[\text{Cu}(\text{L}^4)]$ (Figure 80) via the direct reaction between copper(II) nitrate and bisphosphonate ligand (1:1) in methanol at room temperature. At the addition of the ligand the color of the solution changes to deep green. After removal of solvent, a green oily product is obtained. The coordination of the metal to the ligand was confirmed by EPR analysis.

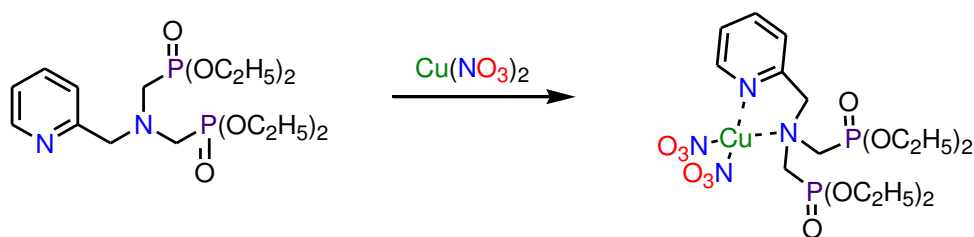


Figure 80. Synthesis of the copper bisphosphonate complex $[\text{Cu}(\text{L}^4)]$.

3.4.2. EPR characterization

The EPR spectra were measured at 120K for both $\text{Cu}(\text{NO}_3)_2$ in MeOH and 1 mM solution copper(II) complex $[\text{Cu}(\text{L}^4)]$ formed by instantaneous mixing of L^4 ligand and copper nitrate salt in methanol (Figure 81).

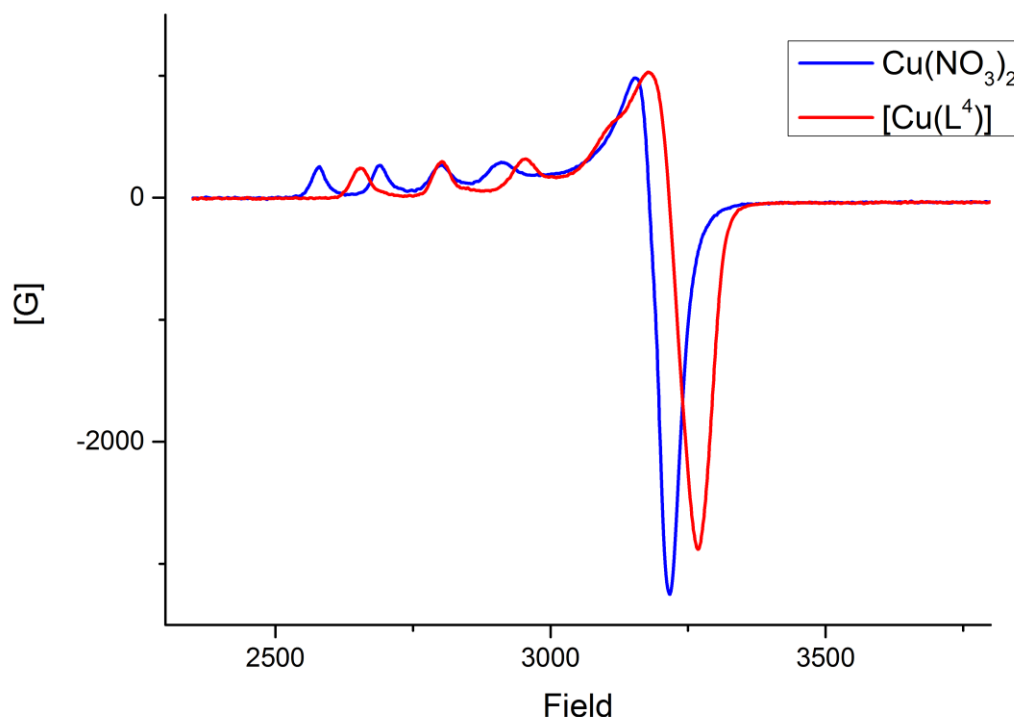


Figure 81. EPR spectra for $\text{Cu}(\text{NO}_3)_2$ (blue) and $[\text{Cu}(\text{L}^4)]$ (red) 1 mM methanolic solution at 120K. Main parameters: $g_{\parallel} = 2.31$ and $A_{\parallel} = 150$ G; $g_{\text{perp}} = 2.06$.

As can be seen from Figure 81, in the spectrum for $[\text{Cu}(\text{L}^4)]$ we see no signals characteristic for free copper(II) salt, this is suggesting the quantitative and immediate coordination of the ligand to the metal with the formation of a new coordination compound namely $[\text{Cu}(\text{L}^4)]$.

3.4.3. Catalytic activity for the oxidation of *p*-nitrophenyl- β -D-glucopyranoside

This reaction is one of the standard for assessment of the oxidative ability for copper complexes. It relies on the oxidation in the position α to oxygen, catalyzed by copper complex. The reactions were either realized in the presence and in absence of hydrogen peroxide (Figure 82).

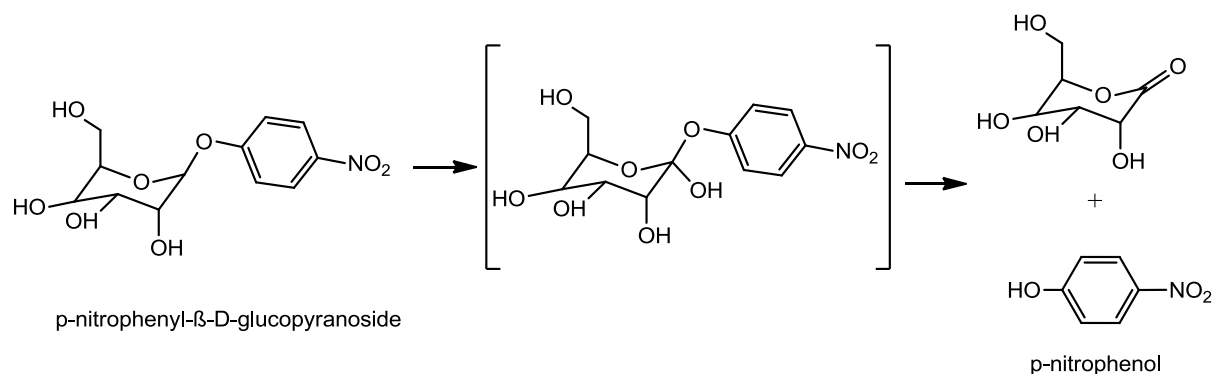


Figure 82. Oxidation scheme of p-nitrophenyl-β-D-glucopyranoside.

The progress of this reaction is monitored by the appearance of p-nitrophenol, which is titrated by UV absorbance at 400nm.

The results shown first that the reaction does not work in absence of hydrogen peroxide (Figure 83 left), the amount of oxidation being almost null.

However, addition of hydrogen peroxide led to varying conversions for oxidation, depending on the amount of catalyst used with a maximum of *ca.* 70% (Figure 83 right). Thus, increasing the amount of catalysis results in increasing the conversion and rate for the reaction, but with a maximum concentration of 0.8 mM after which the rate increase is no longer effective (Figure 84).

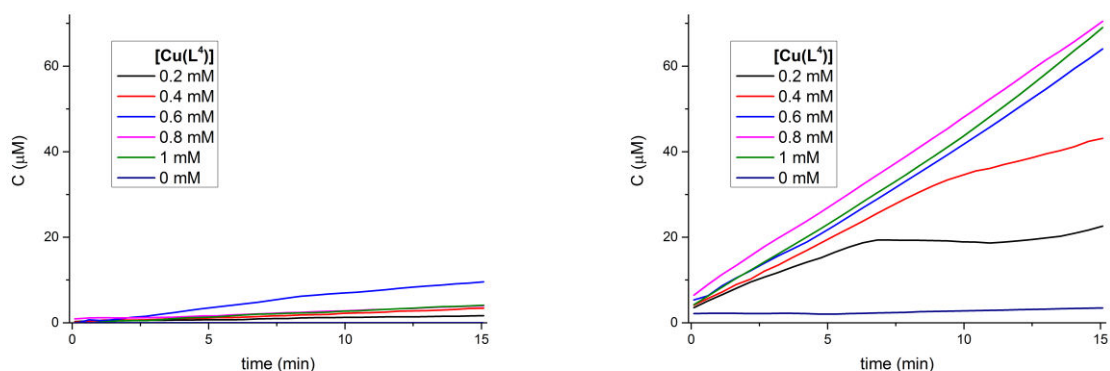


Figure 83. Oxidation of p-nitrophenyl-β-D-glucopyranoside in presence of $[Cu(L^4)]$ catalyst alone (left) and in presence of hydrogen peroxide (right).

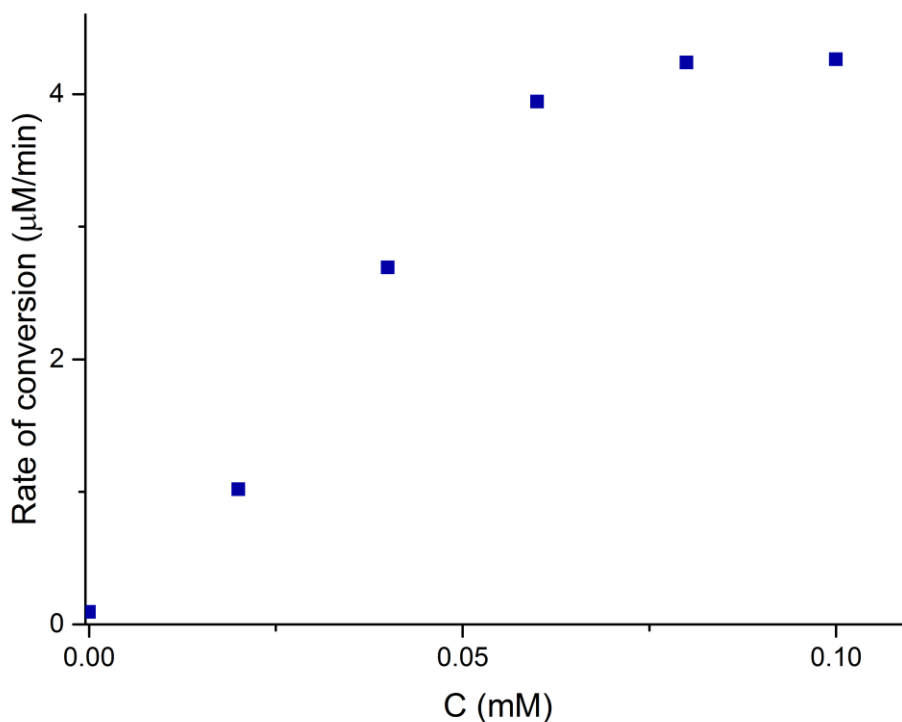


Figure 84. Rate of conversion of *p*-nitrophenyl- β -D-glucopyranoside into *p*-nitrophenol in presence of $[\text{Cu}(\text{L}^4)]$ catalyst and hydrogen peroxide.

As shown in Figure 84, the maximal rate of conversion is 4.26 mol of substrate in presence of 1 mol of catalyst and 1 mol H_2O_2 .

3.5. *N,N* bis(phosphonic acid methyl) 2-methylamino pyridine (L^6)

The synthesis of this acid was already reported⁸⁵ using a similar Kabachnik-Fields reaction (Figure 85), but using phosphonic acid instead of diethyl phosphite.

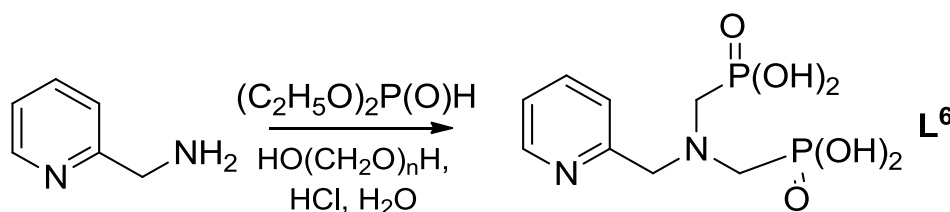


Figure 85. Illustration of *N,N* bis(phosphonic acid methyl) 2-methylamino pyridine (L^6) ligand.

This reaction was reported to occur with 57% yield. However, we were unable to get a pure compound using this procedure, and only black polymeric product was obtained instead.

To circumvent this difficulty, we employed another methodology developed by McKenna,⁸⁶ starting from tetraester **L**⁴, which was submitted to bromotrimethylsilane to give the trimethylsilyl ester, followed by reaction with methanol to yield the acid.

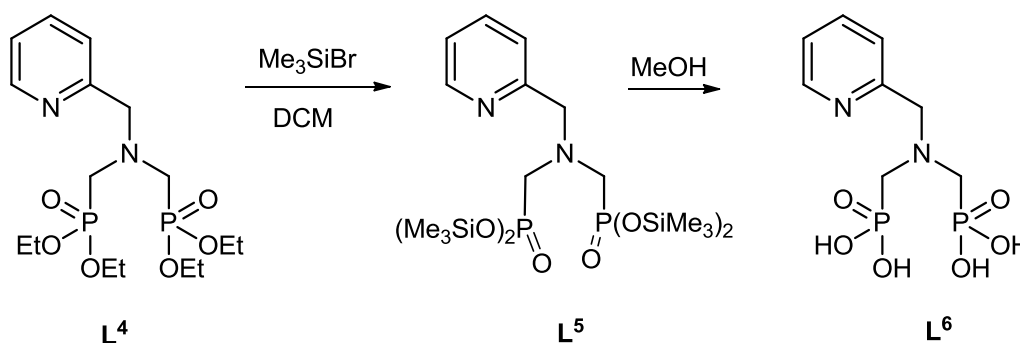


Figure 86. Synthesis of *N,N* bis(phosphonic acid methyl) 2-methylamino pyridine (**L**⁶) ligand, using a new approach and formation of **L**⁵.

This method allows an easy synthesis of the required acid, with good purity.

As already pointed out, the interest for phosphonic acids is that they can be easily grafted onto metallic surfaces. Bisphosphonic acids usually give more resistant adducts than phosphonic acids. The following part illustrates our first results related to the grafting of *N,N* bis(phosphonic acid methyl) 2-methylamino pyridine obtained above onto titanium oxide, and further reaction of the resulting adduct with copper salts. The resulting material was assessed for oxygen consumption.

3.6. TiO_2 nanoparticles and O_2 consumption

The phosphonic acid deposition on TiO_2 was realized at 25 °C under stirring for 20 minutes in aqueous solution. To 8 samples of 10 μg of TiO_2 were added 2 mL aqueous solution of ligand of 8 different concentrations (from 10 μM to 2000 μM). The quantity of adsorbed ligand was quantified spectrophotometrically, by difference between the initial amount and the measured amount of acid remaining in solution after filtration.

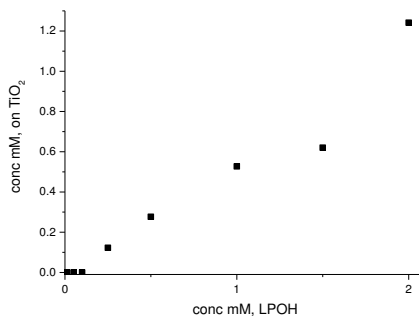


Figure 87. Concentration of adsorbed ligand on the TiO₂ surface in dependence of TiO₂.

Further we have decided to work with 1 mM solution of ligand on TiO₂. From Figure 87 we can see that for 1 mM solution of ligand on the surface of TiO₂ is adsorbed half, 0.5 mM ligand.

After washing and determining that the ligand is not removed from TiO₂ surface 1 equivalent Cu(NO₃)₂ aqueous solution was added and the suspension was stirred for another 20 minutes. From EPR experiment we can see that the coordination of the metal to the ligand occurs instantaneously even at low concentration, that's why we can presume that all copper coordinated to the pyridine moiety of the ligand. The complex bound on TiO₂ surface was washed with water and re-suspended in 2 mL H₂O.

This sample was used further for catalytic studies and co-adsorption of ruthenium bipyridine-phosphonate, and in the presence of potassium persulfate as additional oxidant. The use of an oxymeter allowed the determination of the amount of oxygen dissolved in the solution, which was shown to decrease with time (Figure 88).

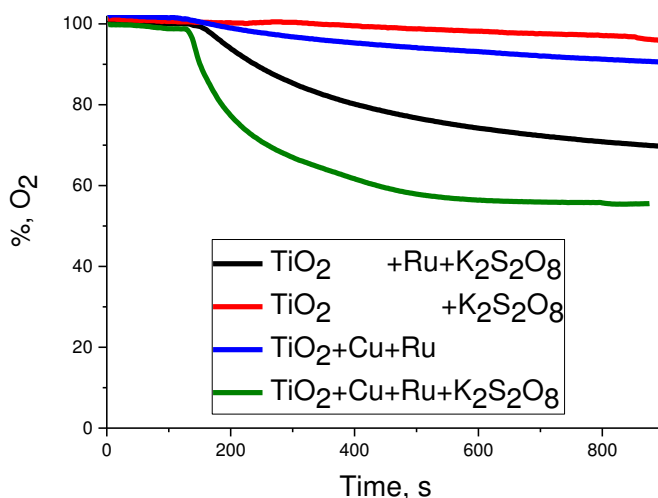


Figure 88. Oxygen consumption in presence of Cu complex adsorbed on TiO₂.

Oxygen consumption was dependent with the reaction conditions, and was effective only in the presence of ruthenium complex. Additional presence of potassium persulfate increased the uptake.

These results shown that the system is able to activate oxygen, but its fate remains unknown. At this moment, it is difficult to understand which oxidation is occurring in this system.

It was shown that photodecomposition of the bisphosphonate group $-\text{C}(\text{PO}_3\text{H}_2)_2(\text{OH})$ by singlet oxygen in the presence of ruthenium bipyridine complex may occur,⁸⁷ but we still have to determine if a similar mechanism may occur in our conditions.

3.7. Conclusions to Chapter 3

In this part, we described the synthesis of a palladium(II) and a copper (II) complex from an aminobisphosphonate ligand incorporating an aminopyridine moiety. This is the first time that such a bisphosphonate is used as a ligand. The complexes were fully characterized by the usual spectroscopic techniques. In the palladium complex, the metal is bound to the pyridine nitrogen atom only, whereas the copper complex did not yield any crystalline product, so its X rays diffraction analysis could not be performed. The catalytic activity of the copper complex was assayed for the oxidation of p-nitrophenyl- β -glucopyraniside, thus showing a satisfactory conversion in the presence of hydrogen peroxide as co-oxidant. Finally, the corresponding bisphosphonic acid was used for grafting of a copper complex onto titanium oxide. The resulting structure was shown to be able to activate oxygen. All these preliminary results should need more time to be developed.

CHAPTER 4

EXPERIMENTAL SECTION

4.1. Physical methods of investigation

Elemental analyses were performed using a Thermo Finnigan EA 1112 instrument. The results were validated by at least two measurements.

UV-Vis spectra were recorded on a Varian Cary 50 spectrophotometer from 200-800 nm with samples in 1.0 path length quartz cuvette.

^1H - and ^{13}C -NMR spectra were recorded on Bruker—Avance III nanobay - 400MHz. Chemical shifts for ^1H - and ^{13}C -NMR spectra are referred to TMS or the residual protonated solvent.

FT-IR spectra were recorded in FT-IR in attenuated total reflection (ATR) mode on a Bruker TENSOR 27 spectrometer equipped with a single-reflection DuraSamplIR diamond ATR accessory. Intensities are mentioned in the parenthesis as vs = very strong, s = strong, m = medium, w = weak, vw = very weak and sh = shoulder.

All electrochemical measurements were carried out under argon atmosphere at room temperature using a Biologic SP-150 instrument. All solutions contained the supporting electrolyte NBu_4PF_6 (0.1 M). For cyclic voltammetry, a standard three-electrode configuration was used consisting of a glassy carbon ($d = 2 \text{ mm}^2$) working and counter electrodes and a Ag-wire placed in a AgNO_3 (0.01 M in MeCN)/ NBu_4PF_6 (0.2 M in MeCN)-solution as a pseudo-reference electrode. The system was systematically calibrated against ferrocene after each experiment and all the potentials are therefore given versus the Fc/Fc^+ redox potential.

X-Band EPR measurements were carried out using a BRUKER EMX9/2.7 spectrometer equipped with a B-VT2000 digital temperature controller (100-400 K). The EPR spectra simulations have been performed using Matlab program package Easyspin.⁸⁸ The optimum hamiltonien parameters have been obtained using the 2nd order perturbation then an exact diagonalization has been used for the final simulations. The homogenous linewidth was set to 0.5 mT, no strain of the hyperfine field and a reasonable strain of the g-tensor were used to simulate the width of the recorded lines. A_N was considered isotropic and used in the final simulation of the first-derivative spectra. The Hamiltonian used for the simulations is the following: $H = \mu_b S[g]B + S[A_{Cu}]I_{Cu} + S[A_{N1}]I_{N1} + S[A_{N2}]I_{N2} + \text{nuclear zeeman}$

Single crystal X-ray diffraction data were collected on a Rigaku Oxford Diffraction SuperNova diffractometer. Data collection, cell refinement and data reduction were performed with CrysAlisPro (Rigaku Oxford Diffraction), the structure were solved with SIR92⁸⁹ or SHELXS⁹⁰ and SHELXL-2013⁹⁰ was used for full matrix least squares refinement.

4.2. DFT calculations

All theoretical calculations were performed with the ORCA program package.⁹¹ Full geometry optimizations were undertaken for all complexes using the GGA functional BP86⁹²⁻⁹⁴ and by taking advantage of the resolution of the identity (RI) approximation in the Split-RI-J variant⁹⁵ with the appropriate Coulomb fitting sets⁹⁶ Scalar relativistic effects were included with ZORA paired using the SARC def2-TZVP(-f) basis sets^{97,98} and the decontracted def2-TZVP/J Coulomb fitting basis sets for all atoms. Increased integration grids (Grid4 and GridX4 in ORCA convention) and tight SCF convergence criteria were used. Electronic structures and Molecular Orbital diagrams were obtained from single-point calculations using the hybrid functional B3LYP.^{99,100} Increased integration grids (Grid4 and GridX4 in ORCA convention) and tight SCF convergence criteria were used in the calculations. For according to the experimental conditions solvent effects were accounted and we used the DMF solvent ($\epsilon = 37$) within the framework of the conductor-like screening (COSMO) dielectric continuum approach.¹⁰¹ EPR parameters were evaluated from additional single point calculations using the B3LYP functional. Picture change effects were applied and the integration grids were increased to an integration accuracy of 11 (ORCA convention) for the metal center. Optical properties were also predicted from additional single-point calculations using the hybrid functional B3LYP. Electronic transition energies and dipole moments for all models were calculated using time-dependent DFT (TDDFT)¹⁰²⁻¹⁰⁴ within the Tamm–Dancoff approximation.^{105,106} To increase computational efficiency, the RI approximation¹⁰⁷ was used in calculating the Coulomb term, and at least 30 excited states were calculated in each case. For each transition, difference density plots were generated using the orca plot utility program and were visualized with the Chemcraft program.¹⁰⁸

4.3. Electrocatalysis cell and GC analysis

Electrochemical investigations were carried out on both Pd incorporated complexes in DMF/*n*-NBu₄PF₆ (0.1 M) solution at ambient temperature using a three-electrode configuration (glassy carbon working electrode, Pt counter electrode, Ag/AgNO₃ reference). All potentials are presented vs Fc⁺/Fc redox couple.

H₂ detection was performed using the method described by Summers et al.³⁹ 1 mM solutions of catalyst in DMF containing TFA (90 mM) and TBAPF₆ (0.1 M), were prepared from thoroughly degassed stock solutions and stored under Ar. Ar was continually flowed through the solution and into a 6 port 2 position switch (VICI) at a constant flow (10 cm³ min⁻¹), maintained using a mass flow controller (Bronkhorst, E-Flow series). A 200 μL sample was analyzed automatically every 3.2 min using a gas chromatograph (Shimadzu GC2014) with a thermal conductivity detector operating at 50 °C. The sample was initially passed through a dry ice trap to remove any condensable solvents. Ar was used as the carrier gas and H₂ was detected on an activated molecular sieve column (Shincarbon ST, Restek). Integration of a plot of the production rate versus time yields the total amount of H₂ produced. A voltage was applied using an IVIUMSTAT potentiostat, a boron doped diamond working electrode, platinum mesh counter electrode, Ag/AgNO₃ (0.01 M) in CH₃CN reference electrode were employed and the potentials were converted to the NHE scale by adding 0.54 V.¹⁰⁹

4.4. Oxydation experiments

In a typical experiment, oxidation of veratryl alcohol was performed in a 15 mL tube at 25 °C with a gentle constant shaking. Freshly prepared complex solution of 500 μM was incubated with 100 mM of veratryl alcohol in a 500 μL DMF solution for 30 minutes in presence of 100 mM H₂O₂. Samples were then immediately applied onto a C18 nucleosil column (300 A, 250*4.6 mm) and analyzed by High Performance Liquid Chromatography (Waters 2695 equipped with a photodiode array detector). The aldehyde concentration was determined spectrophotometrically at 310 nm from a standard curve performed with commercial aldehyde solution. Control experiments were conducted using the same conditions as described above with a copper(II) sulfate pentahydrate solution of 500 μM in the presence and absence of H₂O₂.

4.5. DNA cleavage

The nuclease activity of the copper(II) complex $[\text{Cu}(\text{L}^2)_2]$ was studied using a reductant (ascorbate or DTT) or in the presence of hydrogen peroxide. DNA cleavages were carried out under aerobic conditions with a reaction mixture (20 μL total volume) containing 100 ng of supercoiled pUC19 DNA in TE buffer (10 mM Tris-HCl, pH = 8.0; 0.1 mM EDTA; invitrogen, Germany), an appropriate amount of the copper(II) complex $[\text{Cu}(\text{L}^2)_2]$ (50-500 μM) in DMSO or DMF (5% from total volume) and reducing agents (ascorbate, 100 μM or DTT, 100 μM) or hydrogen peroxide (100 μM). The reaction mixtures were incubated at 37°C for 1 h. At the end of the reaction, 3 μL of 6x loading buffer (0.25% bromo-phenol blue, 30% glycerol) were added and the samples were immediately deposited and run on a 1% agarose gel (50 mL) containing 2.5 μL of SYBR Safe DNA gel stain, invitrogen, USA. The gels were run at room temperature at a constant current (50V) for 90 minutes in TAE buffer. Bands of DNA were visualized by UV light and photographed. The proportion of DNA in the SC, NC and LC forms after electrophoresis was estimated quantitatively from the intensities of the bands by using Lane Analysis Tools in Fluo Chem Q software. Control experiments were done using different reagents such as DMSO (1 μL , 5%), DMF (1 μL , 5%), H_2O_2 (100 μM), ascorbate (100 μM), DTT (100 μM) added to SC DNA prior to the addition of complex $[\text{Cu}(\text{L}^2)_2]$.

4.6. Activity towards catalytic p-nitrophenyl- β -D-glucopyranoside oxidation

Activity assays were performed in total volume of 300 μL placed in 96-well plates. Copper complex was placed at concentration ranging from 0 to 0.1 mM in aqueous solutions (carbonate buffer 100 mM at pH 10). The substrate p-nitrophenyl- β -D-glucopyranoside was used at concentration of 20 mM and hydrogen peroxide at concentrations of 20 mM. Controls were performed using the same conditions but in the absence of complexes or hydrogen peroxide or placing the substrate alone in similar reaction conditions. Controls were also performed in the presence of $\text{CuSO}_4 \cdot 5\text{H}_2\text{O}$ instead of the complexes. Reaction mixtures were incubated at 30°C and were monitored by following the absorbance at 400 nm using a BioTek Synergy MX microplate reader. Initial velocities were extracted from the slopes during the

first 15 minutes of reaction in carbonate buffer at pH 10. Quantification was performed by measuring the absorbance at 400 nm ($\epsilon = 18500 \text{ L}\cdot\text{mol}^{-1}\cdot\text{cm}^{-1}$) and using calibration curves obtained with commercial p-nitrophenol placed at different pHs. When performed in water, the amount of p-nitrophenolate was determined at the end of the reaction after basification of the medium by addition of carbonate buffer at pH 10 to reach a final concentration of 100 mM.

4.7. Synthetic procedures for compounds discussed in Chapters 1, 2 and 3

All chemicals were purchased from commercial sources and used as received unless otherwise stated. Basic solvents for synthesis were dried using literature methods. Solvents for spectroscopic investigations were of the highest purity available.

Synthesis of bis[2-(2H-benzotriazol-2-yl)-6-dodecyl-4-methylphenolato]palladium(II) $[\text{Pd}(\text{L}^1)_2]$

To a solution of 2-(2H-benzotriazol-2-yl)-6-dodecyl-4-methylphenol (HL^1) (0.25 g, 0.6 mmol) in THF (3 ml) at ambient temperature was added dropwise a solution of $\text{Pd}(\text{OAc})_2$ (0.07 g, 0.3 mmol) in THF (4 ml). The obtained orange mixture with the total volume of 7 ml was stirred at 20 °C. The reaction was monitored by TLC. After 48 h volatile materials were removed under vacuum. The obtained oilish product was purified by flash chromatography on silicagel using as eluents petroleum ether/methylene chloride (99:1). Compound $[\text{Pd}(\text{L}^1)_2]$ was isolated as an orange oilish product. Yield: 83.7%.

For $[\text{Pd}(\text{C}_{25}\text{H}_{34}\text{N}_3\text{O})_2]$: Yield: 0.2325 g (83.7 %).

IR, ν (cm^{-1}) = 2954.9 (m), 2922.1 (s), 2852.7 (m), 1608.6 (w), 1572.0 (w), 1556.5 (w), 1490.9 (m), 1465.9 (s), 1411.9 (w), 1377.1 (w), 1352.1 (m), 1342.4 (m), 1307.7 (m), 1288.4 (m), 1244.1 (s), 1203.6 (m), 1149.6 (m), 1134.1 (w), 1114.8 (w), 1078.2 (w), 1037.7 (w), 987.5 (w), 976.0 (w), 947.0 (w), 906.5 (m), 856.4 (m), 819.7 (m), 763.8 (m), 734.9 (vs), 680.9 (w), 648.1 (w), 636.5 (w), 557.4 (m), 511.1 (w), 443.6 (w).

¹H-NMR (400 MHz, CDCl₃, ppm): δ 8.48 (broad singlet, 1H, CH), 8.00 (d, 1H, CH, 9.04Hz), 7.66 (s, 1H, CH), 7.55 (t, 2H, CH, 5.72Hz, 6.51Hz), 6.81 (s, 1H, CH), 3.50 (dd, xH,), 2.26 (s, 3H, CH, CH₃-methyl, 1.26 (m, xH,).

ESI-MS (DCM): m/z 891.45 [M+H]⁺.

UV-Vis (DMF): λ_{max}, nm (ε, 10³ L mol⁻¹ cm⁻¹): 310 (22.0), 390 (8.6).

Synthesis of bis[2-(2H-Benzotriazol-2-yl)-4,6-di-tert-pentylphenolato]palladium(II)

[Pd(L²)₂]

To a solution of 2-(2H-Benzotriazol-2-yl)-4,6-di-tert-pentylphenol (**HL²**) (0.70 g, 2.0 mmol) in THF (10 ml) at ambient temperature was added dropwise a solution of Pd(OAc)₂ (0.22 g, 1.0 mmol) in THF (15 ml). The obtained dark red mixture with the total volume of 25 ml was stirred at 20 °C. The reaction was monitored by TLC. After 48 h volatile materials were removed under vacuum. The obtained product was purified by flash chromatography on silicagel using as eluents petroleum ether/methylene chloride (99:1). Compound [Pd(L²)₂] was isolated as an orange solid. Yield: 92.4 %. Suitable crystals for X-ray diffraction study of [Pd(L²)₂]H₂O were grown by recrystallization from chloroform.

For [Pd(C₂₂H₂₈N₃O)₂]: Yield: 0.7309 g (92.4 %).

Elemental Anal.: Calcd.: C, 65.46; H, 6.99; N, 10.41; (C₄₄H₅₆N₆O₂Pd); Found: C, 65.66; H, 6.95; N, 10.15 %.

IR, ν (cm⁻¹) = 2960.7 (m), 2910.5 (w), 2873.9 (w), 1573.9 (w), 1460.1 (m), 1440.8 (m), 1404.1 (m), 1381.0 (w), 1352.1 (w), 1328.9 (w), 1309.6 (m), 1282.6 (m), 1244.1 (m), 1228.6 (m), 1199.7 (w), 1166.9 (w), 1149.6 (w), 1137.97 (w), 1111.0 (w), 1057.0 (w), 1006.8 (w), 987.5 (w), 974.0 (vw), 939.3 (w), 896.9 (vw), 871.8 (w), 840.9 (vw), 825.5 (w), 808.2 (w), 781.2 (w), 763.8 (w), 740.7 (vs), 723.3 (m), 690.5 (w), 663.5 (w), 638.4 (w), 592.1 (w), 563.2 (m), 538.1 (w), 516.9 (m), 505.3 (w), 474.5 (w), 441.7 (m), 395.4 (w), 356.8 (w), 314.4 (m).

ESI-MS (DCM): m/z 807.36 [M+H]⁺.

UV-Vis (DMF): λ_{max}, nm (ε, 10³ L mol⁻¹ cm⁻¹): 310 (34.2), 390 (13.9).

Synthesis of bis[2-(2H-Benzotriazol-2-yl)-4,6-bis(1-methyl-1-phenylethyl)phenolato] palladium(II) [Pd(L³)₂]

To a solution of 2-(2H-Benzotriazol-2-yl)-4,6-bis(1-methyl-1-phenylethyl)phenol (**HL³**) (0.90 g, 2.0 mmol) in THF (10 mL) at ambient temperature was added dropwise a solution of Pd(OAc)₂ (0.22 g, 1.0 mmol) in THF (15 mL). The obtained deep red mixture with the total volume of 25 mL was stirred at 20 °C. The reaction was monitored by TLC. After 48 h volatile materials were removed under vacuum. The obtained product was purified by flash chromatography on silicagel using as eluents petroleum ether/methylene chloride (99:1). Compound [Pd(L³)₂] was isolated as an orange solid. Yield: 93.95 %. Suitable crystals for X-ray diffraction study of [Pd(L³)₂] were grown by recrystallization from DMF (orange hexagons).

For [Pd(C₃₀H₂₈N₃O)₂]: Yield: 0.9165 g (93.95 %).

Elemental Anal.: Calcd.: C, 72.10; H, 5.65; N, 8.41; (C₆₀H₅₆N₆O₂Pd); Found: C, 72.17; H, 5.57; N, 8.28 %.

IR, ν (cm⁻¹) = 2964.5 (w), 2933.7 (w), 2868.1 (w), 1597.0 (w), 1492.9 (w), 1462.0 (m), 1440.8 (m), 1408.0 (m), 1384.9 (w), 1354.0 (w), 1311.6 (m), 1288.4 (m), 1251.8 (m), 1230.6 (m), 1220.9 (m), 1188.1 (w), 1145.7 (w), 1128.3 (w), 1107.1 (w), 1072.4 (w), 1030.0 (w), 987.5 (w), 933.5 (w), 896.9 (w), 873.7 (w), 856.4 (w), 815.9 (m), 761.9 (s), 748.4 (s), 715.6 (w), 696.3 (vs), 667.4 (w), 650.0 (m), 636.5 (w), 615.3 (w), 605.6 (m), 578.6 (w), 561.3 (m), 551.6 (m), 528.48 (w), 509.2 (w), 497.6 (m), 472.6 (w), 455.2 (m), 443.6 (m), 410.8 (m), 403.1 (m), 383.8 (w), 366.5 (w), 326.0 (m).

¹H-NMR (400 MHz, CDCl₃, ppm): δ 7.82 (d, 1H, CH, 8.70Hz), 7.69 (d, 1H, 8.70Hz), 7.64 (s, 1H, CH), 7.39 (d, 2H, CH, 7.37Hz), 7.36 (t, 1H, CH, 7.60Hz,7.60Hz) 7.29 (s, 1H, CH), 7.27 (d, 3H, CH, 8.20Hz), 7.12 (t, 1H, CH, 7.60Hz,7.60Hz) 6.65 (d, 2H, CH, 7.70Hz), 6.24 (t, 2H, CH, 7.40Hz,7.40Hz), 6.03 (t, 2H, CH, 7.30Hz,7.40Hz), 1.79 (s, 3H, CH₃), 1.76 (s, 3H, CH₃), 1.51 (s, 3H, CH₃), 1.18 (s, 3H, CH₃).

ESI-MS (DCM): m/z 999.36 [M+H]⁺.

UV-Vis (DMF): λ_{\max} , nm (ϵ , 10³ L mol⁻¹ cm⁻¹): 310 (35.8), 390 (14.8).

Recrystallization of [Pd(L³)₂] from acetone gave the compound [Pd(L³)₂](CH₃)₂CO. Orange needles.

For [Pd(C₃₀H₂₈N₃O)₂·0.5(CH₃)₂CO]: Elemental Anal.: Calcd.: C, 71.81; H, 5.78; N, 8.17; (C_{61.5}H₅₉N₆O_{2.5}Pd); Found: C, 71.90; H, 5.61; N, 8.10 %.

Synthesis of bis[2-(2H-Benzotriazol-2-yl)-4,6-di-tert-pentylphenolato]copper(II) [Cu(L²)₂]

Bis[2-(2H-benzotriazol-2-yl)-4,6-di-tert-pentylphenolato]copper(II) complex [Cu(L²)₂] was obtained by two different methods.

Method a: A mixture of 2-(2H-Benzotriazol-2-yl)-4,6-di-tert-pentylphenol (HL², 1.406 g, 4 mmol) and Cu(OAc)₂·H₂O (0.399 g, 2.0 mmol) solubilized in ethanol (50 mL) were heated under reflux for 1 hour. After cooling at room temperature, the resulting precipitate was collected by filtration, washed with EtOH (2x5 mL) and dried overnight at room temperature in order to obtain the complex ([Cu(L²)₂], 1.270 g, 83 % yield) as a dark green solid.

Method b: 2-(2H-Benzotriazol-2-yl)-4,6-di-tert-pentylphenol (HL², 0.088 g, 0.25 mmol) dissolved in 10 mL of CH₃CN/toluene (5:3) mixture and triethylamine (0.035 mL, 0.25 mmol) were stirred at room temperature for 10 minutes. Then, Cu(OTf)₂ (0.047 g, 0.13 mmol) dissolved in 1 mL of CH₃CN was added dropwise under stirring. The resulting brown solution was allowed to evaporate slowly at room temperature for a couple of days. The resulting precipitate was filtered, washed with CH₃CN/toluene (5:3) solution (2x5 mL) and dried overnight at room temperature in order to obtain the complex ([Cu(L²)₂], 0.023 g, 23% yield) as a dark green crystalline solid.

Anal. calc. for C₄₄H₅₆N₆O₂Cu (M_r = 764.50 g/mol): C, 69.13 %; H, 7.38 %; N, 10.99 %. Found: C, 69.32 %; H, 7.41 %; N, 10.85 %.

IR, ν (cm⁻¹) (intensity) = 2955.8 (m), 2910.2 (w), 2872.0 (w), 1606.3 (vw), 1576.7 (vw), 1556.0 (vw), 1466.9 (s), 1445.5 (m), 1404.8 (m), 1382.9 (w), 1310.6 (s), 1293.6 (m), 1254.1 (s), 1223.2 (m), 1200.8 (w), 1167.5 (w), 1115.0 (m), 1058.5 (vw), 988.1 (vw), 944.7 (vw), 899.9 (vw), 875.9 (w), 830.9 (m), 808.8 (w), 766.9 (m), 742.9 (vs), 727.5 (m), 692.8 (vw).

UV-vis (DMF): λ_{\max} , nm (ϵ , 10³ L mol⁻¹ cm⁻¹) = 305 (35), 340 (sh) and 410 (13).

ESI-MS in acetone (positive): m/z 764.3835 [M + H]⁺.

Suitable crystals for X-ray diffraction study were grown by slow evaporation of the mother CH₃CN/toluene (5:3) solution.

Synthesis of bis[2-(2H-Benzotriazol-2-yl)-4,6-di-tert-pentylphenolato]copper(II)·DMF [Cu(L²)₂DMF]

Complex [Cu(L²)₂DMF] was obtained by two different methods. Method c: Complex [Cu(L²)₂], 0.2 g, 0.26 mmol) was dissolved in 50 ml of DMF. The resulting brown solution was heated at 50°C for 10 minutes and allowed to cool slowly. After several days, a black crystalline product was collected by filtration, washed with DMF (2x2 mL) and dried at RT to give the complex [Cu(L)₂·(DMF)_{0.5}] ([Cu(L²)₂DMF], 0.171 g, 81% yield). Method d: A mixture of 2-(2H-Benzotriazol-2-yl)-4,6-di-tert-pentylphenol (HL², 0.176 g, 0.5 mmol) and Cu(OAc)₂·H₂O (0.050 g, 0.25 mmol) in DMF (50 ml) were heated at 70 °C for 1 hour. The brown solution was filtered and left to evaporate slowly at RT. The complex [Cu(L)₂·(DMF)_{0.5}] ([Cu(L²)₂DMF], 0.150 g, 75% yield) was collected by filtration and washed with small amounts of DMF to give black needle-like crystalline solid suitable for X-ray diffraction study.

Elemental Analysis: calc. for C_{45.5}H_{59.5}N_{6.5}O_{2.5}Cu (M = 801.05 g/mol): C, 68.22 %; H, 7.49 %; N, 11.37 %; O, 4.99 %; Cu, 7.93 %. Found: C, 68.16 %; H, 7.53 %; N, 11.22 %.

IR (neat): ν (cm⁻¹) (intensity) = 2960.6 (s), 2902.2 (s), 1665.0 (s), 1605.9 (vw), 1571.5 (vw), 1556.0 (vw), 1466.9 (s), 1404.3 (m), 1375.3 (m), 1333.7 (w), 1305.7 (m), 1255.0 (s), 1224.1 (m), 1201.3 (sh), 1137.4 (w), 1113.9 (m), 1057.8 (s), 982.0 (vw), 960.9 (vw), 894.4 (vw), 877.5 (w), 864.6 (w), 805.9 (w), 768.8 (w), 744.9 (vs), 725.7 (m), 671.9 (vw).

UV-vis (DMF): λ_{\max} , nm (ϵ , 10³ L mol⁻¹ cm⁻¹) = 305 (37), 340 (sh) and 410 (13).

Synthesis of bis[2-(2H-Benzotriazol-2-yl)-4,6-di-tert-pentylphenolato]copper(II)·DMA [Cu(L²)₂DMA]

Complex [Cu(L²)₂DMA] was obtained by two different methods. Method c: Complex [Cu(L²)₂], 0.2 g, 0.26 mmol) was dissolved in 50 ml DMA. The resulting brown solution was heated at 50°C for 10 minutes and allowed to cool slowly. After several days brown monocryalline product was collected by filtration and dried at ambient conditions to yield [Cu(L)₂·(DMA)_{0.5}] ([Cu(L²)₂DMA], 0.103 g, 49%). Method d: A mixture of 2-(2H-Benzotriazol-2-yl)-4,6-di-tert-pentylphenol (HL², 0.176 g, 0.5 mmol), Cu(OAc)₂·H₂O (0.050 g, 0.25 mmol) and DMA (50 ml) were heated at 70 °C for 1 hour. No precipitate was formed. The brown solution was filtered and left to evaporate at room temperature. Brown needle-like

crystalline complex $[\text{Cu}(\text{L})_2 \cdot (\text{DMA})_{0.5}]$ ($[\text{Cu}(\text{L}^2)_2\text{DMA}]$, 0.071 g, 35%) suitable for X-ray diffraction analysis was isolated by filtration and washed with small amounts of DMA.

Elemental Analysis: calc. for $\text{C}_{46}\text{H}_{60.5}\text{N}_{6.5}\text{O}_{2.5}\text{Cu}$ ($M = 808.06$ g/mol): C, 68.37 %; H, 7.55 %; N, 11.27 %. Found: C, 68.17 %; H, 7.54 %; N, 11.08 %.

IR (neat): ν (cm^{-1}) (intensity) = 2960.1 (m), 2911.1 (w), 2874.6 (w), 1634.6 (m), 1571.0 (vw), 1555.8 (vw), 1467.8 (s), 1403.4 (m), 1374.6 (w), 1305.7 (m), 1288.0 (m), 1254.6 (s), 1223.6 (m), 1200.4 (w), 1144.9 (w), 1114.1 (w), 1058.3 (w), 1045.3 (w), 1003.3 (w), 981.5 (vw), 934.1 (vw), 876.4 (w), 864.1 (w), 828.8 (w), 805.9 (w), 768.8 (w), 745.1 (vs), 725.9 (m), 688.3 (vw).

UV-vis (DMF): λ_{max} , nm (ϵ , 10^3 L mol $^{-1}$ cm $^{-1}$) = 305 (29), 340 (sh) and 410 (12).

Synthesis of bis[2-(2H-Benzotriazol-2-yl)-4,6-di-tert-pentylphenolato]copper(II)·DMSO $[\text{Cu}(\text{L}^2)_2\text{DMSO}]$

Complex $[\text{Cu}(\text{L}^2)_2\text{DMSO}]$ was obtained by two different methods. Method c: Complex $[\text{Cu}(\text{L}^2)_2]$, 0.2 g, 0.26 mmol) was dissolved in 50 ml of DMSO. The resulting brown solution was heated at 50 °C for 10 minutes and allowed to cool slowly. After several days, a dark green crystalline product was collected by filtration, washed with DMSO (2x2 mL) and dried at RT to give the complex $[\text{Cu}(\text{L})_2 \cdot (\text{DMSO})_{0.33}]$ $[\text{Cu}(\text{L}^2)_2\text{DMSO}]$ (0.038 g, 18% yield). Method d: A mixture of 2-(2H-Benzotriazol-2-yl)-4,6-di-tert-pentylphenol (HL^2 , 0.176 g, 0.5 mmol) and $\text{Cu}(\text{OAc})_2 \cdot \text{H}_2\text{O}$ (0.050 g, 0.25 mmol) in DMSO (50 ml) were heated at 70 °C for 1 hour. The brown solution was filtered and left to evaporate slowly at RT. The complex $[\text{Cu}(\text{L})_2 \cdot (\text{DMSO})_{0.33}]$ $[\text{Cu}(\text{L}^2)_2\text{DMSO}]$ (0.089 g, 45% yield) was collected by filtration to give black needle-like crystalline solid suitable for X-ray diffraction study.

Anal. calc. for $\text{C}_{44.66}\text{H}_{58}\text{N}_6\text{O}_{2.33}\text{S}_{0.33}\text{Cu}$ ($M_r = 790.54$ g/mol): C, 67.86 %; H, 7.39 %; N, 10.63 %; S, 1.35 %. Found: C, 67.73 %; H, 7.50 %; N, 10.46 %; S, 1.38 %.

IR, ν (cm^{-1}) = 2960.1 (m), 2910.7 (m), 2873.0 (m), 1603.7 (vw), 1574.7 (vw), 1553.9 (vw), 1470.4 (s), 1444.9 (m), 1403.9 (m), 1335.0 (w), 1309.4 (s), 1256.5 (s), 1223.4 (m), 1199.8 (w), 1135.2 (w), 1113.6 (m), 1064.1 (m), 1007.1 (w), 989.1 (w), 927.6 (vw), 875.6 (m), 829.7 (m), 807.8 (w), 767.8 (m), 750.8 (vs), 726.1 (m), 692.0 (w).

UV-vis (DMF): λ_{max} , nm (ϵ , 10^3 L mol $^{-1}$ cm $^{-1}$) = 305 (32), 340 (sh) and 410 (13).

Monooxidation of [Cu(L²)₂]

Under an inert atmosphere, to a solution of **1** (0.015 g, 0.0196 mol) in CH₂Cl₂ (20 mL) at RT or in DMF (20 mL) at -40 °C were added NOSbF₆ (0.0052 g, 0.0196 mmol) as one-electron oxidant to the medium. This solution of [**1**]⁺·SbF₆⁻ was stirred for a couple of minutes and used further for other studies.

Synthesis of *N*-(methylene-2-pyridine)-*N,N*-bis(diethoxyphosphorylmethyl)amine (L⁴)

A mixture of diethyl phosphite (3g, 22 mmol), 2-(amino methyl) pyridine (0.94 g, 9 mmol) and paraformaldehyde (0.62 g, 21 mmol) was stirred under reflux at 100 °C for 3h. After cooling, 20 ml diethyl ether and K₂CO₃ (2g, 15 mmol) were added and stirred another 2h at rt. The organic reddish solution was separated from the brown solid by decantation and the solvent was removed at 700 mBar at 40 °C. Purification by flash chromatography using ethylacetate/methanol (4:1) afforded the desired compound **L⁴** (3 g, 85% yield) as an orange oil.

Anal. calc. for C₁₆H₃₀N₂O₆P₂ (Mr = 408.16 g/mol): C, 47.06 %; H, 7.40 %; N, 6.86 %. Found: C, 45.52 %, H, 7.52 %, N, 6.87 %.

UV-vis (MeCN): λ_{max}, nm (ε, 10³ L mol⁻¹ cm⁻¹) = 260 (7.7).

¹H-NMR (400 MHz, CDCl₃, ppm): δ 8.45 (d, 1H, CH, 4.28Hz), 7.65 (t, 1H, 7.59Hz,7.66Hz), 7.56 (d, 1H, CH, 7.79Hz), 7.14 (t, 1H, CH, 5.36Hz,6.04Hz), 4.07 (d, 8H, CH₂, 6.87Hz) 4.03 (s, 2H, CH₂), 3.18 (d, 4H, CH₂, 9.70Hz), 1.25 (t, 12H, CH₃, 7.07Hz,7.07Hz).

³¹P-NMR (162 MHz, CDCl₃, ppm): δ 24.36 (s).

ESI-MS (DCM): m/z 408.16 [M+H]⁺.

Synthesis of *N*-(methylene-2-pyridine)-*N,N*-bis(diethoxyphosphoryltrimethylsilyl)amine (L**⁵) and *N,N* bis(phosphonic acid methyl) 2-methylamino pyridine (**L**⁶)**

To a solution of *N*-(methylene-2-pyridine)-*N,N*-bis(diethoxyphosphorylmethyl)amine (**L**⁴) (0.52 g, 1.27 mmol) in freshly distilled DCM was added dropwise bromotrimethylsilane (2.32 g, 15.20 mmol). The mixture was stirred at room temperature for 24 hours to give a light yellow solution. The volatile components were evaporated under vacuum up to the formation of **L**⁵ compound as a deep yellow oil. This product was dissolved in 30 mL methanol and stirred over night for another 24 hours. The volatile components were evaporated under vacuum up to the formation of **L**⁶ compound as an orange oil.

***For L*⁵:**

¹H-NMR (400 MHz, CDCl₃, ppm): δ 8.61 (s, 1H, CH), 8.37 (s, 1H), 7.95 (s, 1H, CH), 7.79 (s, 1H, CH), 4.41 (s, 2H, CH₂) 3.19 (d, 4H, CH₂, 10.50Hz), 0.00 (s, 30H, CH₃).

³¹P-NMR (162 MHz, CDCl₃, ppm): δ 22.16 (s).

***For L*⁶:**

¹H-NMR (400 MHz, CDCl₃, ppm): δ 8.82 (d, 1H, CH, 5.45Hz), 8.61 (t, 1H, 7.88Hz,7.87Hz), 8.14 (t, 1H, CH, 8.22Hz,7.93Hz), 8.03 (t, 1H, CH, 6.54Hz,6.93Hz), 4.54 (s, 2H, CH₂), 3.34 (m, 4H, CH₂, 6.87Hz).

³¹P-NMR (162 MHz, CDCl₃, ppm): δ 22.14 (s).

Synthesis of Palladium complex [Pd(L⁴)₂]

To a solution of PdCl₂ (0.1985 g, 1.119 mmol) in CH₃CN was added dropwise a solution of L⁴ in CH₂Cl₂ (0.8756 g, 2.144 mmol), and the mixture was stirred at rt. The pale yellow precipitate was recrystallised from DMSO and in 1 year to give yellow monocrystalline compound [Pd(L⁴)₂] (0.2536 g, 11.5% yield).

UV-vis (MeCN): λ_{max}, nm (ε, 10³ L mol⁻¹ cm⁻¹) = 230 (25.3), 260 (sh), 400 (0.2).

ESI-MS (DCM): m/z 1017.18 [M+Na]⁺.

¹H-NMR (400 MHz, CDCl₃, ppm): δ 9.05 (d, 2H, CH, 5.44Hz), 8.06 (t, 2H, 9.27Hz,8.34Hz), 7.81 (t, 2H, CH, 7.63Hz,7.82Hz), 7.33 (t, 2H, CH, 6.08Hz,7.30Hz), 5.40 (s, 4H, CH₂), 4.19 (m, 16H, CH₂), 3.46 (d, 8H, CH₂, 9.21Hz), 1.36 (t, 24H, CH₃, 7.02Hz,6.93Hz).

³¹P-NMR (162 MHz, CDCl₃, ppm): δ 24.32 (s).

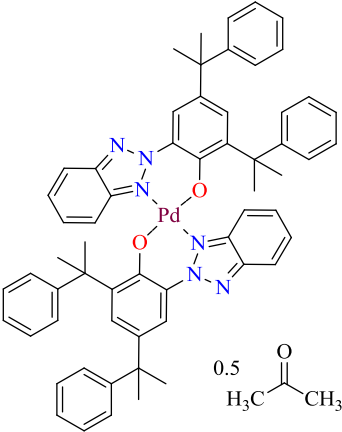
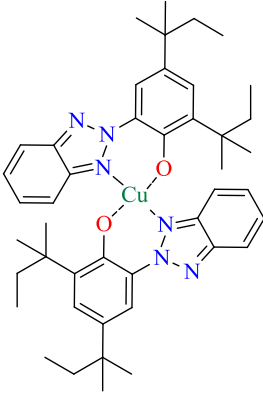
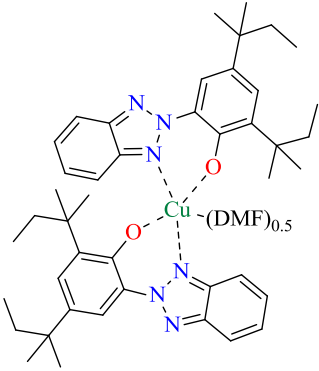
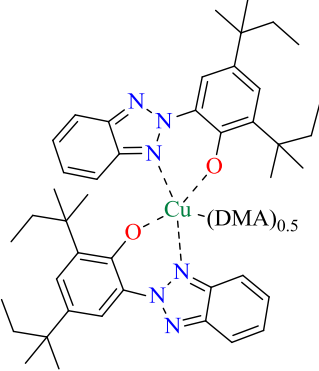
Synthesis of Copper complex [Cu(L⁴)]

To a blue solution of Cu(ClO₄)₂·6H₂O in 40 mL solvent mixture: DCM:THF (3:1) was added dropwise a brown(dark yellow) solution of L⁴ in DCM 20 mL.

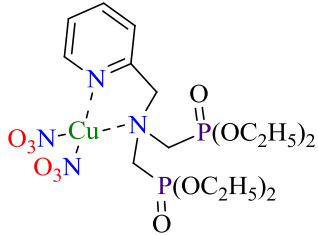
The resulting deep green solution was stirred at rt for 1h. The volatile components were evaporated under vacuum up to the formation of [Cu(L⁴)] compound as a green oil.

Table 25. The list of compounds obtained within this work, including the shortcuts and their structure.

Shortcut	Full name	Structure
$[\text{Pd}(\text{L}^1)_2]$	<i>bis[2-(2H-benzotriazol-2-yl)-6-dodecyl-4-methylphenolato]palladium(II)</i>	
$[\text{Pd}(\text{L}^2)_2]$	<i>bis[2-(2H-Benzotriazol-2-yl)-4,6-di-tert-pentylphenolato]palladium(II)</i>	
$[\text{Pd}(\text{L}^2)_2]\text{H}_2\text{O}$	<i>bis[2-(2H-Benzotriazol-2-yl)-4,6-di-tert-pentylphenolato] palladium(II)•H2O</i>	
$[\text{Pd}(\text{L}^3)_2]$	<i>bis[2-(2H-Benzotriazol-2-yl)-4,6-bis(1-methyl-1-phenylethyl)phenolato] palladium(II)</i>	

Shortcut	Full name	Structure
$[\text{Pd}(\text{L}^3)_2](\text{CH}_3)_2\text{CO}$	<i>bis[2-(2H-Benzotriazol-2-yl)-4,6-bis(1-methyl-1-phenylethyl)phenolato]palladium(II)•acetone</i>	
$[\text{Cu}(\text{L}^2)_2]$	<i>bis[2-(2H-Benzotriazol-2-yl)-4,6-di-tert-pentylphenolato]copper(II)</i>	
$[\text{Cu}(\text{L}^2)_2\text{DMF}]$	<i>bis[2-(2H-Benzotriazol-2-yl)-4,6-di-tert-pentylphenolato]copper(II) •DMF</i>	
$[\text{Cu}(\text{L}^2)_2\text{DMA}]$	<i>bis[2-(2H-Benzotriazol-2-yl)-4,6-di-tert-pentylphenolato]copper(II) •DMA</i>	

Shortcut	Full name	Structure
[Cu(L ²) ₂ DMSO]	<i>bis</i> [2-(2 <i>H</i> -Benzotriazol-2-yl)-4,6-di- <i>tert</i> -pentylphenolato]copper(II) •DMSO	
(L ⁴)	<i>N</i> -(methylene-2-pyridine)- <i>N,N</i> -bis(diethoxyphosphorylmethyl)amine	
(L ⁵)	<i>N</i> -(methylene-2-pyridine)- <i>N,N</i> -bis(diethoxyphosphoryltrimethylsilyl)amine	
(L ⁶)	<i>N,N</i> bis(phosphonic acid methyl) 2-methylamino pyridine	
[Pd(L ⁴) ₂]	dichloro bis[<i>N</i> -(methylene-2-pyridine)- <i>N,N</i> -bis(diethoxyphosphorylmethyl)amino]palladium(II) •H ₂ O	

Shortcut	Full name	Structure
[Cu(L ⁴)]	<i>dinitro [N-(methylene-2-pyridine)-N,N-bis(diethoxyphosphorylmethyl)amino]copper(II)</i>	

4.8. Conclusions to Chapter 4

Using the synthesis procedures described in chapter 4, fourteen products were synthesized (Table 25), from which five are new palladium based benzotriazolyl phenol containing coordination compounds. Four products are new coordination compounds of benzotriazolyl phenol based ligands with Copper(II) atoms. Two products are new coordination compounds of phosphonate based ligands with Palladium(II) and Copper(II) atoms. The composition and structure of compounds was confirmed by IR, NMR, Mass Spectrometry, Elemental Analysis and X-ray crystallography. In order to study and explain the physico-chemical properties of products a number of modern methods were used, namely: UV-Vis absorption spectroscopies, cyclic voltammetry, and computer assisted DFT calculations. Application potential of the final products was studied in a number of systems including electrocatalytic proton reduction, veratryl alcohol oxydation and DNA cleavage experiments.

GENERAL CONCLUSIONS

1. Five new palladium (II) complexes starting from benzotriazolylphenolate ligands were synthesized, and physically characterised by different techniques such as X-ray, IR, Elemental analysis, Mass spectrometry, NMR, UV-vis, Cyclic voltammetry and employed as catalysts in the hydrogen evolution reaction. The detection of the evolved hydrogen was performed using the gas analysis in DMF in the presence of 90 mM TFA and applying a potential of -0.36 V *vs.* NHE (-1.08 V *vs.* Fc⁺/Fc couple) to the boron doped diamond working electrode which resulted in immediate formation of molecular hydrogen. Almost seven turnovers were reached after five hours of electrolysis and no sign of hydrogen production decrease was observed at the end of this time. In order to facilitate the determination of the mechanism, the one electron reduced species was generated both chemically and electrochemically and characterised using spectroscopic methods as UV-vis, EPR and theoretical calculations.

2. Four new copper (II) complexes with 2-(2H-Benzotriazol-2-yl)-4,6-di-tert-pentylphenol ligand were synthesized, and physically characterised by using different techniques such as X-ray, IR, Elemental analysis, Mass spectrometry, UV-vis, Cyclic voltammetry, EPR, theoretical calculations and employed as catalysts in veratryl alcohol oxidation reaction. Copper benzotriazolate compounds also showed effective biological activity in DNA cleavage experiments. To determine the nature of the active species, the one-electron oxidized species generated via chemical oxidation reaction and fully characterized by spectroscopic methods (EPR and UV-vis) and theoretical calculations which confirmed the formation of a copper (II) complex with an organic ligand radical in a ferromagnetic configuration. By trying to mimic galactose oxydase's activity, were performed the catalytic oxidation experiments of veratryl alcohol. The veratryl aldehyde formation occurred in presence of hydrogen peroxide with a TON value of 5 mol of product per mol of catalyst calculated at a 30 minutes reaction time in DMF solution at room temperature. The oxidative digestion of DNA in presence of the copper(II) complex was studied on supercoiled pUC19 DNA at 37°C with different agents such as hydrogen peroxide, ascorbate or dithiotreitol (100 μ M). The copper based complex exhibits significant DNA cleavage reactivity in the 100-500 μ M concentration range. These results confirm that the DNA cleavage occurs through an oxidative process rather than a hydrolytic one.

3. Three new organic phosphonate-based ligands containing the pyridinic ring as well as their Cu(II) and Pd(II) coordination compounds were synthesised and studied. As a major difference of benzotriazolyl-phenolate ligands, the phosphonate containing ligands as well as their complexes are hydrophilic, thus allowing the possibility to use such compounds as catalysts in water mediated reactions. The preliminary results consists of the synthesis of two new complexes of palladium (II) and copper (II) metals which were employed as catalyst in the oxidation reaction of p-nitrophenyl- β -D-glucopyranoside. The oxidation of the substrate occurs in presence of hydrogen peroxide. In future, in order to achieve oxygen production/consumption catalysis will be performed the deposition of phosphonate complexes on TiO₂ surface in aqueous media. The preliminary results showed that copper (II) complex deposited on TiO₂ nanoparticles exhibited oxygen consumption behavior.

PERSPECTIVES

1. In order to enhance the catalytic activity in proton reduction processes will be interesting to synthesize new benzotriazolyl phenolate based coordination compounds with different transitional metals like nickel(II) or cobalt(II) since they are earth abundant and therefore much cheaper.
2. To enhance the oxidative activity of copper complexes it would be interesting to substitute the aliphatic radicals on the phenolate part of the ligand in order to enhance the solubility in aqueous solutions.
3. The grafting of the phosphonate ligands on different surfaces like metal oxides or proteins opens a large field of investigation of the properties of transitional metal based complexes in different catalytic processes.

REFERENCES

- 1 Fujishima, A.; Honda, K. Electrochemical Photolysis of Water at a Semiconductor Electrode. *Nature* **1972**, *238* (5358), 37–38 DOI: 10.1038/238037a0.
- 2 Grätzel, M.; McEvoy, A. J. Hydrogen Production by Solar Photolysis of Water. In *American Physical Society Symposium Basic Research for the Hydrogen Economy*; APS, 2004.
- 3 Costentin, C.; Dridi, H.; Savéant, J.-M. Molecular Catalysis of H₂ Evolution: Diagnosing Heterolytic versus Homolytic Pathways. *Journal of the American Chemical Society* **2014**, *136* (39), 13727–13734 DOI: 10.1021/ja505845t.
- 4 Kochem, A.; Neese, F.; van Gastel, M. Spectroscopic and Quantum Chemical Study of the Ni($\text{P}^{\text{Ph}}_2\text{N}^{\text{C}_6\text{H}_4\text{CH}_2\text{P}(\text{O})(\text{OEt})_2}_2$)₂ Electrocatalyst for Hydrogen Production with Emphasis on the Ni^I Oxidation State. *The Journal of Physical Chemistry C* **2014**, *118* (5), 2350–2360 DOI: 10.1021/jp411710b.
- 5 Jones, A. K.; Sillery, E.; Albracht, S. P. J.; Armstrong, F. A. Direct Comparison of the Electrocatalytic Oxidation of Hydrogen by an Enzyme and a Platinum catalyst Electronic Supplementary Information (ESI) Available: Levich Plots at 1% and 10% Hydrogen, and a Comparison of the Effect of Carbon Monoxide on Oxidation Currents Obtained at Platinum and Enzyme-Modified Electrodes. See <http://www.rsc.org/suppdata/cc/b2/b201337a/>. *Chemical Communications* **2002**, No. 8, 866–867 DOI: 10.1039/b201337a.
- 6 Fontecilla-Camps, J. C.; Volbeda, A.; Cavazza, C.; Nicolet, Y. Structure/Function Relationships of [NiFe]- and [FeFe]-Hydrogenases. *Chemical Reviews* **2007**, *107* (10), 4273–4303 DOI: 10.1021/cr050195z.
- 7 Vignais, P. M.; Billoud, B. Occurrence, Classification, and Biological Function of Hydrogenases: An Overview. *Chemical Reviews* **2007**, *107* (10), 4206–4272 DOI: 10.1021/cr050196r.

- 8 Tard, C.; Pickett, C. J. Structural and Functional Analogues of the Active Sites of the [Fe]-, [NiFe]-, and [FeFe]-Hydrogenases [†]. *Chemical Reviews* **2009**, *109* (6), 2245–2274 DOI: 10.1021/cr800542q.
- 9 Gloaguen, F.; Lawrence, J. D.; Schmidt, M.; Wilson, S. R.; Rauchfuss, T. B. Synthetic and Structural Studies on $[\text{Fe}_2(\text{SR})_2(\text{CN})_x(\text{CO})_{6-x}]^x$ as Active Site Models for Fe-Only Hydrogenases. *Journal of the American Chemical Society* **2001**, *123* (50), 12518–12527 DOI: 10.1021/ja016071v.
- 10 *Bioinspired Catalysis: Metal-Sulfur Complexes*; Weigand, W., Schollhammer, P., Eds.; Wiley-VCH Verlag GmbH & Co. KGaA: Weinheim, Germany, 2014.
- 11 Fourmond, V.; Jacques, P.-A.; Fontecave, M.; Artero, V. H₂ Evolution and Molecular Electrocatalysts: Determination of Overpotentials and Effect of Homoconjugation. *Inorganic Chemistry* **2010**, *49* (22), 10338–10347 DOI: 10.1021/ic101187v.
- 12 Kilgore, U. J.; Roberts, J. A. S.; Pool, D. H.; Appel, A. M.; Stewart, M. P.; DuBois, M. R.; Dougherty, W. G.; Kassel, W. S.; Bullock, R. M.; DuBois, D. L. $[\text{Ni}(\text{P}^{\text{Ph}}_2\text{N}^{\text{C}_6\text{H}_4\text{X}})_2]^{2+}$ Complexes as Electrocatalysts for H₂ Production: Effect of Substituents, Acids, and Water on Catalytic Rates. *Journal of the American Chemical Society* **2011**, *133* (15), 5861–5872 DOI: 10.1021/ja109755f.
- 13 Rakowski DuBois, M.; DuBois, D. L. Development of Molecular Electrocatalysts for CO₂ Reduction and H₂ Production/Oxidation. *Accounts of Chemical Research* **2009**, *42* (12), 1974–1982 DOI: 10.1021/ar900110c.
- 14 Rakowski DuBois, M.; DuBois, D. L. The Roles of the First and Second Coordination Spheres in the Design of Molecular Catalysts for H₂ Production and Oxidation. *Chem. Soc. Rev.* **2009**, *38* (1), 62–72 DOI: 10.1039/B801197B.
- 15 Wang, M.; Chen, L.; Sun, L. Recent Progress in Electrochemical Hydrogen Production with Earth-Abundant Metal Complexes as Catalysts. *Energy & Environmental Science* **2012**, *5* (5), 6763 DOI: 10.1039/c2ee03309g.
- 16 Fisher, B. J.; Eisenberg, R. Electrocatalytic Reduction of Carbon Dioxide by Using Macrocycles of Nickel and Cobalt. *Journal of the American Chemical Society* **1980**, *102* (24), 7361–7363 DOI: 10.1021/ja00544a035.
- 17 Hu, X.; Brunschwig, B. S.; Peters, J. C. Electrocatalytic Hydrogen Evolution at Low Overpotentials by Cobalt Macrocyclic Glyoxime and Tetraimine Complexes. *Journal of the American Chemical Society* **2007**, *129* (29), 8988–8998 DOI: 10.1021/ja067876b.
- 18 Bernhardt, P. V.; Jones, L. A. Electrochemistry of Macrocyclic Cobalt(III/II) Hexaamines: Electrocatalytic Hydrogen Evolution in Aqueous Solution. *Inorganic Chemistry* **1999**, *38* (22), 5086–5090 DOI: 10.1021/ic981425d.
- 19 Kellett, R. M.; Spiro, T. G. Cobalt(I) Porphyrin Catalysts of Hydrogen Production from Water. *Inorganic Chemistry* **1985**, *24* (15), 2373–2377 DOI: 10.1021/ic00209a011.
- 20 Kellett, R. M.; Spiro, T. G. Cobalt Porphyrin Electrode Films as Hydrogen Catalysts. *Inorganic Chemistry* **1985**, *24* (15), 2378–2382 DOI: 10.1021/ic00209a012.
- 21 Zhao, F.; Zhang, J.; Abe, T.; Wöhrle, D.; Kaneko, M. Electrocatalytic Proton Reduction by Phthalocyanine Cobalt Derivatives Incorporated in poly(4-Vinylpyridine-Co-Styrene) Film. *Journal of Molecular Catalysis A: Chemical* **1999**, *145* (1-2), 245–256 DOI: 10.1016/S1381-1169(99)00013-8.

- 22 Houlding, V.; Geiger, T.; Kölle, U.; Grätzel, M. Electrochemical and Photochemical Investigations of Two Novel Electron Relays for Hydrogen Generation from Water. *J. Chem. Soc., Chem. Commun.* **1982**, No. 12, 681–683 DOI: 10.1039/C39820000681.
- 23 Koelle, U.; Paul, S. Electrochemical Reduction of Protonated Cyclopentadienylcobalt Phosphine Complexes. *Inorganic Chemistry* **1986**, 25 (16), 2689–2694 DOI: 10.1021/ic00236a007.
- 24 Losse, S.; Vos, J. G.; Rau, S. Catalytic Hydrogen Production at Cobalt Centres. *Coordination Chemistry Reviews* **2010**, 254 (21–22), 2492–2504 DOI: 10.1016/j.ccr.2010.06.004.
- 25 Artero, V.; Chavarot-Kerlidou, M.; Fontecave, M. Splitting Water with Cobalt. *Angewandte Chemie International Edition* **2011**, 50 (32), 7238–7266 DOI: 10.1002/anie.201007987.
- 26 Bigi, J. P.; Hanna, T. E.; Harman, W. H.; Chang, A.; Chang, C. J. Electrocatalytic Reduction of Protons to Hydrogen by a Water-Compatible Cobalt Polypyridyl Platform. *Chem. Commun.* **2010**, 46 (6), 958–960 DOI: 10.1039/B915846D.
- 27 Jacobsen, G. M.; Yang, J. Y.; Twamley, B.; Wilson, A. D.; Bullock, R. M.; Rakowski DuBois, M.; DuBois, D. L. Hydrogen Production Using Cobalt-Based Molecular Catalysts Containing a Proton Relay in the Second Coordination Sphere. *Energy & Environmental Science* **2008**, 1 (1), 167 DOI: 10.1039/b805309j.
- 28 Chu, J.; Xie, X.; Yang, S.; Zhan, S. Synthesis and Electro-Catalytic Properties of a Dinuclear palladium(I) 1,3-bis[(2-Chloro)benzene]triazenide Complex. *Inorganica Chimica Acta* **2014**, 410, 191–194 DOI: 10.1016/j.ica.2013.10.026.
- 29 Sirbu, D.; Turta, C.; Gibson, E. A.; Benniston, A. C. The Ferrocene Effect: Enhanced Electrocatalytic Hydrogen Production Using Meso-Tetraferrocenyl Porphyrin Palladium(II) and Copper(II) Complexes. *Dalton Trans.* **2015**, 44 (33), 14646–14655 DOI: 10.1039/C5DT02191J.
- 30 McDaniel, N. D.; Coughlin, F. J.; Tinker, L. L.; Bernhard, S. Cyclometalated Iridium(III) Aquo Complexes: Efficient and Tunable Catalysts for the Homogeneous Oxidation of Water. *Journal of the American Chemical Society* **2008**, 130 (1), 210–217 DOI: 10.1021/ja074478f.
- 31 Rosevear, J.; Wilshire, J. Preparation of Some 2-(2' H -Benzotriazol-2'-Yl)phenol Ultraviolet Absorbers: Application of the Transalkylation Reaction. *Australian Journal of Chemistry* **1985**, 38 (8), 1163 DOI: 10.1071/CH9851163.
- 32 Katritzky, A. R.; Rachwal, S.; Hitchings, G. J. Benzotriazole: A Novel Synthetic Auxiliary. *Tetrahedron* **1991**, 47 (16–17), 2683–2732 DOI: 10.1016/S0040-4020(01)87080-0.
- 33 Scapin, G.; Patel, S. B.; Becker, J. W.; Wang, Q.; Desponts, C.; Waddleton, D.; Skorey, K.; Cromlish, W.; Bayly, C.; Therien, M.; Gauthier, J. Y.; Li, C. S.; Lau, C. K.; Ramachandran, C.; Kennedy, B. P.; Asante-Appiah, E. The Structural Basis for the Selectivity of Benzotriazole Inhibitors of PTP1B[†]. *Biochemistry* **2003**, 42 (39), 11451–11459 DOI: 10.1021/bi035098j.
- 34 Rosevear, J.; Wilshire, J. The Reduction of Some O-Nitrophenylazo Dyes with Thiourea S,S-Dioxide (Formamidinesulfinic Acid): A General Synthesis of 2-Aryl-2H-Benzotriazoles and Their 1-Oxides. *Australian Journal of Chemistry* **1984**, 37 (12), 2489 DOI: 10.1071/CH9842489.
- 35 Novak, L.; Farkas, R.; Törinösi, M.; Kolonits, P.; Jimenez Alonso, O. One-Pot Synthesis of Benzotriazoles and Benzotriazole 1-Oxides by Reductive Cyclization of O-Nitrophenylazo Compounds with Benzyl Alcohol. *HETEROCYCLES* **2009**, 78 (10), 2579 DOI: 10.3987/COM-09-11759.

- 36 Kim, B. H.; Kim, S. K.; Lee, Y. S.; Jun, Y. M.; Baik, W.; Lee, B. M. Reductive Cyclization of O-Nitrophenylazobenzenes to 2-Aryl-2H-Benzotriazoles by SmI₂. *Tetrahedron Letters* **1997**, *38* (48), 8303–8306 DOI: 10.1016/S0040-4039(97)10207-6.
- 37 Franceschi, F.; Guardigli, M.; Solari, E.; Floriani, C.; Chiesi-Villa, A.; Rizzoli, C. Designing Copper(I) Photosensitizers for the Norbornadiene–Quadricyclane Transformation Using Visible Light: An Improved Solar Energy Storage System. *Inorganic Chemistry* **1997**, *36* (18), 4099–4107 DOI: 10.1021/ic9706156.
- 38 Tsai, C.-Y.; Lin, C.-H.; Ko, B.-T. Bis[2-(2-*H*-Benzotriazol-2-yl)-4-methylphenolato]palladium(II). *Acta Crystallographica Section E Structure Reports Online* **2009**, *65* (6), m619–m619 DOI: 10.1107/S1600536809016390.
- 39 Summers, P. A.; Dawson, J.; Ghiotto, F.; Hanson-Heine, M. W. D.; Vuong, K. Q.; Stephen Davies, E.; Sun, X.-Z.; Besley, N. A.; McMaster, J.; George, M. W.; Schröder, M. Photochemical Dihydrogen Production Using an Analogue of the Active Site of [NiFe] Hydrogenase. *Inorganic Chemistry* **2014**, *53* (9), 4430–4439 DOI: 10.1021/ic500089b.
- 40 Shimazaki, Y. Phenoxy Radical-Metal Complexes. In *PATAI'S Chemistry of Functional Groups*; Rappoport, Z., Ed.; John Wiley & Sons, Ltd: Chichester, UK, 2012.
- 41 Shimazaki, Y.; Yamauchi, O. Recent Advances in Metal-Phenoxy Radical Chemistry. *Indian Journal of Chemistry -Section A* **2011**, *50A*, 383–394.
- 42 Kersten, P.; Cullen, D. Copper Radical Oxidases and Related Extracellular Oxidoreductases of Wood-Decay Agaricomycetes. *Fungal Genetics and Biology* **2014**, *72*, 124–130 DOI: 10.1016/j.fgb.2014.05.011.
- 43 Kersten, P. J.; Cullen, D. Cloning and Characterization of cDNA Encoding Glyoxal Oxidase, a H₂O₂-Producing Enzyme from the Lignin-Degrading Basidiomycete *Phanerochaete Chrysosporium*. *Proceedings of the National Academy of Sciences of the United States of America* **1993**, *90* (15), 7411–7413.
- 44 Whittaker, M. M.; Kersten, P. J.; Nakamura, N.; Sanders-Loehr, J.; Schweizer, E. S.; Whittaker, J. W. Glyoxal Oxidase from *Phanerochaete Chrysosporium* Is a New Radical-Copper Oxidase. *Journal of Biological Chemistry* **1996**, *271* (2), 681–687 DOI: 10.1074/jbc.271.2.681.
- 45 Whittaker, J. W. Free Radical Catalysis by Galactose Oxidase. *Chemical Reviews* **2003**, *103* (6), 2347–2364 DOI: 10.1021/cr020425z.
- 46 Parikka, K.; Master, E.; Tenkanen, M. Oxidation with Galactose Oxidase: Multifunctional Enzymatic Catalysis. *Journal of Molecular Catalysis B: Enzymatic* **2015**, *120*, 47–59 DOI: 10.1016/j.molcatb.2015.06.006.
- 47 Yin, D. (Tyler); Urresti, S.; Lafond, M.; Johnston, E. M.; Derikvand, F.; Ciano, L.; Berrin, J.-G.; Henrissat, B.; Walton, P. H.; Davies, G. J.; Brumer, H. Structure–function Characterization Reveals New Catalytic Diversity in the Galactose Oxidase and Glyoxal Oxidase Family. *Nature Communications* **2015**, *6*, 10197 DOI: 10.1038/ncomms10197.
- 48 Pickl, M.; Fuchs, M.; Glueck, S. M.; Faber, K. The Substrate Tolerance of Alcohol Oxidases. *Applied Microbiology and Biotechnology* **2015**, *99* (16), 6617–6642 DOI: 10.1007/s00253-015-6699-6.
- 49 Hollmann, F.; Arends, I. W. C. E.; Buehler, K.; Schallmeyer, A.; Bühler, B. Enzyme-Mediated Oxidations for the Chemist. *Green Chem.* **2011**, *13* (2), 226–265 DOI: 10.1039/C0GC00595A.

- 50 Thomas, F. Ten Years of a Biomimetic Approach to the Copper(II) Radical Site of Galactose Oxidase. *European Journal of Inorganic Chemistry* **2007**, 2007 (17), 2379–2404 DOI: 10.1002/ejic.200601091.
- 51 Chaudhuri, P.; Wieghardt, K. Phenoxyl Radical Complexes. In *Progress in Inorganic Chemistry*; Karlin, K. D., Ed.; John Wiley & Sons, Inc.: New York, USA, 2002; pp 151–216.
- 52 de Bellefeuille, D.; Orio, M.; Barra, A.-L.; Aukauloo, A.; Journaux, Y.; Philouze, C.; Ottenwaelder, X.; Thomas, F. Redox Noninnocence of the Bridge in Copper(II) Salophen and Bis(oxamato) Complexes. *Inorganic Chemistry* **2015**, 54 (18), 9013–9026 DOI: 10.1021/acs.inorgchem.5b01285.
- 53 Asami, K.; Takashina, A.; Kobayashi, M.; Iwatsuki, S.; Yajima, T.; Kochem, A.; van Gestel, M.; Tani, F.; Kohzuma, T.; Thomas, F.; Shimazaki, Y. Characterization of One-Electron Oxidized Copper(>ii)-Salophen-Type Complexes; Effects of Electronic and Geometrical Structures on Reactivities. *Dalton Trans.* **2014**, 43 (5), 2283–2293 DOI: 10.1039/C3DT52338A.
- 54 Asami, K.; Tsukidate, K.; Iwatsuki, S.; Tani, F.; Karasawa, S.; Chiang, L.; Storr, T.; Thomas, F.; Shimazaki, Y. New Insights into the Electronic Structure and Reactivity of One-Electron Oxidized Copper(II)-(Disalicylidene)diamine Complexes. *Inorganic Chemistry* **2012**, 51 (22), 12450–12461 DOI: 10.1021/ic3018503.
- 55 Kochem, A.; Jarjays, O.; Baptiste, B.; Philouze, C.; Vezin, H.; Tsukidate, K.; Tani, F.; Orio, M.; Shimazaki, Y.; Thomas, F. One-Electron Oxidized Copper(II) Salophen Complexes: Phenoxyl versus Diiminobenzene Radical Species. *Chemistry - A European Journal* **2012**, 18 (4), 1068–1072 DOI: 10.1002/chem.201102882.
- 56 Chaudhuri, P.; Wieghardt, K.; Weyhermüller, T.; Paine, T. K.; Mukherjee, S.; Mukherjee, C. Biomimetic Metal-Radical Reactivity: Aerial Oxidation of Alcohols, Amines, Aminophenols and Catechols Catalyzed by Transition Metal Complexes. *Biological Chemistry* **2005**, 386 (10) DOI: 10.1515/BC.2005.118.
- 57 Jiang, Q.; Xiao, N.; Shi, P.; Zhu, Y.; Guo, Z. Design of Artificial Metallonucleases with Oxidative Mechanism. *Coordination Chemistry Reviews* **2007**, 251 (15-16), 1951–1972 DOI: 10.1016/j.ccr.2007.02.013.
- 58 Butsch, K.; Klein, A.; Nitsche, S.; Stirnat, K.; Hawkett, J. R.; McInnes, E. J. L.; Bauer, M. Generation and Characterisation of the Phenoxyl-Radical Containing Cu(ii) Complex [Cu(triaz)₂]⁺ (triaz⁻ = O₂N Chelating Triazole-Phenolate). *Dalton Transactions* **2012**, 41 (37), 11464 DOI: 10.1039/c2dt31369c.
- 59 Li, C.-Y.; Hsu, S.-J.; Lin, C.; Tsai, C.-Y.; Wang, J.-H.; Ko, B.-T.; Lin, C.-H.; Huang, H.-Y. Air-Stable Copper Derivatives as Efficient Catalysts for Controlled Lactide Polymerization: Facile Synthesis and Characterization of Well-Defined Benzotriazole Phenoxide Copper Complexes. *Journal of Polymer Science Part A: Polymer Chemistry* **2013**, 51 (18), 3840–3849 DOI: 10.1002/pola.26780.
- 60 Saydam, S.; Yilmaz, E.; Bağcı, F.; Yağlıoğlu, H. G.; Elmalı, A.; Salih, B.; Bekaroğlu, Ö. Synthesis, Characterization, Electrochemical, and Optic Limiting Properties of Novel CoII, CuII, and Double-Decker LuIII Phthalocyanines. *European Journal of Inorganic Chemistry* **2009**, 2009 (14), 2096–2103 DOI: 10.1002/ejic.200801174.
- 61 Addison, A. W.; Hendriks, H. M. J.; Reedijk, J.; Thompson, L. K. Copper Complexes of the “Tripod” Ligand tris(2-Benzimidazolylmethyl)amine: Five- and Six-Coordinate copper(II) Derivatives and Some copper(I) Derivatives. *Inorganic Chemistry* **1981**, 20 (1), 103–110 DOI: 10.1021/ic50215a024.

- 62 Goodman, B. A.; Raynor, J. B. Electron Spin Resonance of Transition Metal Complexes. In *Advances in Inorganic Chemistry and Radiochemistry*; Elsevier, 1970; Vol. 13, pp 135–362.
- 63 Hathaway, B. J.; Billing, D. E. The Electronic Properties and Stereochemistry of Mono-Nuclear Complexes of the copper(II) Ion. *Coordination Chemistry Reviews* **1970**, 5 (2), 143–207 DOI: 10.1016/S0010-8545(00)80135-6.
- 64 Hathaway, B. J. A New Look at the Stereochemistry and Electronic Properties of Complexes of the copper(II) Ion. In *Complex Chemistry*; Springer Berlin Heidelberg: Berlin, Heidelberg, 1984; Vol. 57, pp 55–118.
- 65 Peisach, J.; Blumberg, W. E. Structural Implications Derived from the Analysis of Electron Paramagnetic Resonance Spectra of Natural and Artificial Copper Proteins. *Archives of Biochemistry and Biophysics* **1974**, 165 (2), 691–708 DOI: 10.1016/0003-9861(74)90298-7.
- 66 Sakaguchi, U.; Addison, A. W. Spectroscopic and Redox Studies of Some copper(II) Complexes with Biomimetic Donor Atoms: Implications for Protein Copper Centres. *Journal of the Chemical Society, Dalton Transactions* **1979**, No. 4, 600 DOI: 10.1039/dt9790000600.
- 67 Jaividhya, P.; Dhivya, R.; Akbarsha, M. A.; Palaniandavar, M. Efficient DNA Cleavage Mediated by Mononuclear Mixed Ligand copper(II) Phenolate Complexes: The Role of Co-Ligand Planarity on DNA Binding and Cleavage and Anticancer Activity. *Journal of Inorganic Biochemistry* **2012**, 114, 94–105 DOI: 10.1016/j.jinorgbio.2012.04.018.
- 68 Liang, Q.; Ananias, D. C.; Long, E. C. Ni(II)·Xaa-Xaa-His Induced DNA Cleavage: Deoxyribose Modification by a Common “Activated” Intermediate Derived from KHSO_5 , MMPP, or H_2O_2 . *Journal of the American Chemical Society* **1998**, 120 (2), 248–257 DOI: 10.1021/ja9720218.
- 69 Clearfield, A. Metal Phosphonate Chemistry. In *Progress in Inorganic Chemistry*; Karlin, K. D., Ed.; John Wiley & Sons, Inc.: Hoboken, NJ, USA, 1997; Vol. 47, pp 371–510.
- 70 Goura, J.; Chandrasekhar, V. Molecular Metal Phosphonates. *Chemical Reviews* **2015**, 115 (14), 6854–6965 DOI: 10.1021/acs.chemrev.5b00107.
- 71 Chandrasekhar, V.; Senapati, T.; Dey, A.; Hossain, S. Molecular Transition-Metal Phosphonates. *Dalton Transactions* **2011**, 40 (20), 5394 DOI: 10.1039/c0dt01069c.
- 72 Nash, K. L. Actinide Phosphonate Complexes in Aqueous Solutions. *Journal of Alloys and Compounds* **1994**, 213-214, 300–304 DOI: 10.1016/0925-8388(94)90919-9.
- 73 Galezowska, J.; Gumienna-Kontecka, E. Phosphonates, Their Complexes and Bio-Applications: A Spectrum of Surprising Diversity. *Coordination Chemistry Reviews* **2012**, 256 (1-2), 105–124 DOI: 10.1016/j.ccr.2011.07.002.
- 74 Tusek-Bozic, L. Aminophosphonate Metal Complexes of Biomedical Potential. *Current Medicinal Chemistry* **2013**, 20 (16), 2096–2117 DOI: 10.2174/0929867311320160004.
- 75 Xu, G.; Yang, C.; Liu, B.; Wu, X.; Xie, Y. Synthesis of New Potential Chelating Agents: Catechol-Bisphosphonate Conjugates for Metal Intoxication Therapy. *Heteroatom Chemistry* **2004**, 15 (3), 251–257 DOI: 10.1002/hc.20013.
- 76 Queffelec, C.; Petit, M.; Janvier, P.; Knight, D. A.; Bujoli, B. Surface Modification Using Phosphonic Acids and Esters. *Chemical Reviews* **2012**, 112 (7), 3777–3807 DOI: 10.1021/cr2004212.
- 77 Dalpozzo, R. Magnetic Nanoparticle Supports for Asymmetric Catalysts. *Green Chem.* **2015**, 17 (7), 3671–3686 DOI: 10.1039/C5GC00386E.

- 78 Fu, R.; Hu, S.; Wu, X. Syntheses, Crystal Structures, Thermal Stabilities and Luminescence of Two Metal Phosphonates. *CrystEngComm* **2012**, *14* (10), 3478 DOI: 10.1039/c2ce25279a.
- 79 Kontturi, M.; Vuokila-Laine, E.; Peräniemi, S.; Pakkanen, T. T.; Vepsäläinen, J. J.; Ahlgrén, M. A Structural Study of Bisphosphonate Metal Complexes. Alkaline Earth Metal Complexes of (dichloromethylene)bisphosphonic Acid P,P'-Diethyl Ester. *Journal of the Chemical Society, Dalton Transactions* **2002**, No. 9, 1969–1973 DOI: 10.1039/b201124g.
- 80 Kontturi, M.; Laurila, E.; Mattsson, R.; Peräniemi, S.; Vepsäläinen, J. J.; Ahlgrén, M. Structures of Bisphosphonate Metal Complexes: Zinc and Cadmium Complexes of Clodronate and Its Partial Ester Derivatives. *Inorganic Chemistry* **2005**, *44* (7), 2400–2406 DOI: 10.1021/ic048329z.
- 81 Kontturi, M.; Peräniemi, S.; Vepsäläinen, J. J.; Ahlgrén, M. X-Ray Diffraction Study of Bisphosphonate Metal Complexes: Mg and Ca Complexes of (dichloromethylene)bisphosphonic Acid P,P'-Diisopropyl Ester. *Polyhedron* **2005**, *24* (2), 305–309 DOI: 10.1016/j.poly.2004.11.006.
- 82 Jokiniemi, J.; Vuokila-Laine, E.; Peräniemi, S.; Vepsäläinen, J. J.; Ahlgrén, M. Structural Study of Metal Complexes of Bisphosphonate Amide Ester: Copper, Magnesium, Zinc and Cadmium Complexes of (dichloromethylene)bisphosphonic Acid P-Piperidinium-P'-Methyl Ester. *CrystEngComm* **2007**, *9* (2), 158–164 DOI: 10.1039/B616077H.
- 83 Bálint, E.; Fazekas, E.; Kóti, J.; Keglevich, G. Synthesis of *N,N*-Bis(dialkoxyphosphinoylmethyl)- and *N,N*-Bis(diphenylphosphinoylmethyl)- β - and γ -Amino Acid Derivatives by the Microwave-Assisted Double Kabachnik-Fields Reaction: Synthesis of *N,N*-Bis(dialkoxyphosphinoylmethyl)- and *N,N*-Bis(diphenylphosphinoylmethyl)- β - and γ -Amino Acid. *Heteroatom Chemistry* **2015**, *26* (1), 106–115 DOI: 10.1002/hc.21221.
- 84 Contrella, N. D.; Sampson, J. R.; Jordan, R. F. Copolymerization of Ethylene and Methyl Acrylate by Cationic Palladium Catalysts That Contain Phosphine-Diethyl Phosphonate Ancillary Ligands. *Organometallics* **2014**, *33* (13), 3546–3555 DOI: 10.1021/om5004489.
- 85 Janicki, R. Synthesis, Crystal Structure and Spectral Properties of Diammonium Dihydrogen N-(methylene-2-Pyridine)-N,N,-Di-(methylenephosphonate). *Journal of Molecular Structure* **2013**, *1036*, 35–41 DOI: 10.1016/j.molstruc.2012.09.051.
- 86 McKenna, C. E.; Higa, M. T.; Cheung, N. H.; McKenna, M.-C. The Facile Dealkylation of Phosphonic Acid Dialkyl Esters by Bromotrimethylsilane. *Tetrahedron Letters* **1977**, *18* (2), 155–158 DOI: 10.1016/S0040-4039(01)92575-4.
- 87 Hanson, K.; Ashford, D. L.; Concepcion, J. J.; Binstead, R. A.; Habibi, S.; Luo, H.; Glasson, C. R. K.; Templeton, J. L.; Meyer, T. J. Sensitized Photodecomposition of Organic Bisphosphonates By Singlet Oxygen. *Journal of the American Chemical Society* **2012**, *134* (41), 16975–16978 DOI: 10.1021/ja307987g.
- 88 Stoll, S.; Schweiger, A. EasySpin, a Comprehensive Software Package for Spectral Simulation and Analysis in EPR. *Journal of Magnetic Resonance* **2006**, *178* (1), 42–55 DOI: 10.1016/j.jmr.2005.08.013.
- 89 Altomare, A.; Cascarano, G.; Giacovazzo, C.; Guagliardi, A.; Burla, M. C.; Polidori, G.; Camalli, M. SIR 92 – a Program for Automatic Solution of Crystal Structures by Direct Methods. *Journal of Applied Crystallography* **1994**, *27* (3), 435–435 DOI: 10.1107/S002188989400021X.
- 90 Sheldrick, G. M. A Short History of SHELX. *Acta Crystallographica Section A Foundations of Crystallography* **2008**, *64* (1), 112–122 DOI: 10.1107/S0108767307043930.

- 91 Neese, F. The ORCA Program System. *Wiley Interdisciplinary Reviews: Computational Molecular Science* **2012**, 2 (1), 73–78 DOI: 10.1002/wcms.81.
- 92 Perdew, J. P. Density-Functional Approximation for the Correlation Energy of the Inhomogeneous Electron Gas. *Physical Review B* **1986**, 33 (12), 8822–8824 DOI: 10.1103/PhysRevB.33.8822.
- 93 Perdew, J. P. Erratum: Density-Functional Approximation for the Correlation Energy of the Inhomogeneous Electron Gas. *Physical Review B* **1986**, 34 (10), 7406–7406 DOI: 10.1103/PhysRevB.34.7406.
- 94 Becke, A. D. Density-Functional Exchange-Energy Approximation with Correct Asymptotic Behavior. *Physical Review A* **1988**, 38 (6), 3098–3100 DOI: 10.1103/PhysRevA.38.3098.
- 95 Neese, F. An Improvement of the Resolution of the Identity Approximation for the Formation of the Coulomb Matrix. *Journal of Computational Chemistry* **2003**, 24 (14), 1740–1747 DOI: 10.1002/jcc.10318.
- 96 Weigend, F. Accurate Coulomb-Fitting Basis Sets for H to Rn. *Physical Chemistry Chemical Physics* **2006**, 8 (9), 1057 DOI: 10.1039/b515623h.
- 97 Pantazis, D. A.; Chen, X.-Y.; Landis, C. R.; Neese, F. All-Electron Scalar Relativistic Basis Sets for Third-Row Transition Metal Atoms. *Journal of Chemical Theory and Computation* **2008**, 4 (6), 908–919 DOI: 10.1021/ct800047t.
- 98 Pantazis, D. A.; Neese, F. All-Electron Scalar Relativistic Basis Sets for the Lanthanides. *Journal of Chemical Theory and Computation* **2009**, 5 (9), 2229–2238 DOI: 10.1021/ct900090f.
- 99 Becke, A. D. A New Mixing of Hartree–Fock and Local Density-Functional Theories. *The Journal of Chemical Physics* **1993**, 98 (2), 1372 DOI: 10.1063/1.464304.
- 100 Lee, C.; Yang, W.; Parr, R. G. Development of the Colle-Salvetti Correlation-Energy Formula into a Functional of the Electron Density. *Physical Review B* **1988**, 37 (2), 785–789 DOI: 10.1103/PhysRevB.37.785.
- 101 Klamt, A.; Schüürmann, G. COSMO: A New Approach to Dielectric Screening in Solvents with Explicit Expressions for the Screening Energy and Its Gradient. *J. Chem. Soc., Perkin Trans. 2* **1993**, No. 5, 799–805 DOI: 10.1039/P29930000799.
- 102 Casida, M. E. Time-Dependent Density Functional Response Theory for Molecules. In *Recent Advances in Density Functional Methods*; WORLD SCIENTIFIC, 1995; Vol. 1, pp 155–192.
- 103 Stratmann, R. E.; Scuseria, G. E.; Frisch, M. J. An Efficient Implementation of Time-Dependent Density-Functional Theory for the Calculation of Excitation Energies of Large Molecules. *The Journal of Chemical Physics* **1998**, 109 (19), 8218 DOI: 10.1063/1.477483.
- 104 Bauernschmitt, R.; Ahlrichs, R. Treatment of Electronic Excitations within the Adiabatic Approximation of Time Dependent Density Functional Theory. *Chemical Physics Letters* **1996**, 256 (4-5), 454–464 DOI: 10.1016/0009-2614(96)00440-X.
- 105 Hirata, S.; Head-Gordon, M. Time-Dependent Density Functional Theory within the Tamm–Dancoff Approximation. *Chemical Physics Letters* **1999**, 314 (3-4), 291–299 DOI: 10.1016/S0009-2614(99)01149-5.
- 106 Hirata, S.; Head-Gordon, M. Time-Dependent Density Functional Theory for Radicals. *Chemical Physics Letters* **1999**, 302 (5-6), 375–382 DOI: 10.1016/S0009-2614(99)00137-2.

- 107 Neese, F. Prediction of Electron Paramagnetic Resonance G Values Using Coupled Perturbed Hartree–Fock and Kohn–Sham Theory. *The Journal of Chemical Physics* **2001**, *115* (24), 11080
DOI: 10.1063/1.1419058.
- 108 *Chemcraft*, [Http://www.chemcraftprog.com](http://www.chemcraftprog.com).
- 109 *Applications of Physical Methods to Inorganic and Bioinorganic Chemistry*; Scott, R. A., Lukehart, C. M., Eds.; EIC books; Wiley: Hoboken, NJ, 2007.

RESUME

De nos jours, la capacité à synthétiser de nouveaux catalyseurs métallique bioinspirés pour améliorer et élargir le spectre d'activité catalytique est d'une importance capitale pour une chimie respectueuse de notre environnement.

Cette thèse se concentre sur la conception de nouveaux complexes de métaux de transition (cuivre et palladium) basés sur deux classes différentes de ligands organiques : les benzotriazolyle-phénolates et les phosphonates. La synthèse et la caractérisation de nouveaux composés a été réalisée par différentes méthodes physico-chimiques (électrochimie, EPR, UV-vis, IR, cristallographie aux rayons X) et la chimie théorique. La génération et la caractérisation des différentes espèces réduites et oxydées nous ont aidés dans la détermination des mécanismes possible. Les composés obtenus ont été utilisés avec succès comme catalyseurs dans divers procédés tels que: la production d'hydrogène, l'oxydation d'alcool et le clivage d'ADN.

Mots Clés: Chimie biomimétique, Chimie de coordination, Réaction d'oxydation, Réduction des protons, Electrochemistry, Calcul théorique DFT

ABSTRACT

Nowadays, the ability to synthesize new bioinspired metal catalysts to improve and broaden the spectrum of catalytic activity is of paramount importance for sustainable chemistry respectful for our environment. This thesis is focused on the design of transition metal complexes (copper and palladium) based on two different classes of organic ligands: benzotriazolyl-phenolates and phosphonates.

Different original complexes based on palladium and copper were synthesized from benzotriazolyl-phenolate and phosphonates ligands. The characterization of the new compounds was performed by different physical and physico-chemical methods (electrochemistry, EPR, UV-vis, IR, X-ray crystallography) and quantum chemistry. The generation and characterization of different reduced and oxidized species helped us in the possible mechanisms determination. The obtained compounds were successfully employed as catalysts in different processes as: hydrogen production, alcohol oxidation and DNA cleavage.

Keywords: Biomimetic Chemistry, Coordination chemistry, Oxidation reaction, Proton reduction, Electrochemistry, Quantum chemistry DFT